TECHNISCHE FAKULTÄT DER
CHRISTIAN-ALBRECHTS-UNIVERSITÄT
ZU KIEL

FeGa based tunneling magnetoresistance junctions and strain sensors

Dissertation

zur Erlangung des akademischen Grades
Doktor der Ingenieurwissenschaften (Dr.-Ing.)

der Technischen Fakultät
der Christian-Albrechts-Universität zu Kiel

Thajudin Ahmed Fazir

Kiel

August 2012

1. Gutachter : Prof. Dr. Eckhard Quandt

2. Gutachter : Prof. Dr. Bernhard Wagner

(ggf. 3. Gutachter).....

Datum der mündlichen Prüfung : 14 / 12 / 2012

Acknowledgements

I would like to thank sincerely Prof. Dr. Eckhard Quandt for giving me the opportunity to work in his group, teaching and guiding me constantly to improve my research abilities.

I am truly thankful to Dr. Dirk Meyners for his continuous support and guidance during the whole period of my thesis and also during my thesis writing.

Many thanks to Dr. Christiane zamponi for preparing the FIB samples and for performing EDX measurements, Dr. Christoph Bechtold for his overall support in the lab and cleanroom, Dr. Antonio Malave for his support in the clean room especially IBE, Dr. Thomas Von Hofe for the discussions, help with the CAD drawing for masks and for introducing me to TMR and strain measurements, Dr. Julian Teliban for many useful discussions and overall help in the lab, Dipl. Ing. Claas Thede for his help with VSM and friendly discussions, Dipl. Ing. Andre Piorra for introducing me to X-ray diffraction measurements, Gislinde Schroder, Ellen Riemer, Dipl. Ing. Thomas Metzing, Dipl. Ing. Kristina Schlüter, MSc Ali Tavassolizadeh, MSc Ahmed Zayed and all the members of the group for helping me both at work and also personally.

I would like to thank Prof. Dr. Lorentz Kienle and his group members especially Dr. rer.nat. Ulrich Schürmann and former group member Dr.Ing Venkata Sai Kiran Chakravadhanula for the TEM characterization of my samples, Christin Szillus for the TEM sample preparation.

Many thanks to Prof. Dr. Franz Faupel and his group members Dr. Vladimir Zaporojtchenko for the XPS measurements and Dr. Amit Kulkarni for annealing experiments.

Thank you so much Dr. Manfred Rührig of Siemens AG, Erlangen for the TMR stacks and timely help with literature and Dr. Jürgen Feydt of caesar institute for 3 dimensional XRD measurements.

I would like to acknowledge my Hiwi Jamaluddin Channa for performing magnetoresistance and annealing experiments.

The US NAVY for providing me financial support through ONR award number N000140810685.

Many thanks to Prof. Dr. Bernhard Wagner for readily accepting to evaluate this thesis work and Prof. Dr. Rainer Adelung for accepting to be a member of the exam board for thesis defense.

I would like to thank my beloved father D. Mohamed Thajudin and mother Z. Zamela Zainullabdeen for their sacrifice, love, affection and encouragement. Without them I could have never made it to Germany.

I would like to thank my dear wife Ella Noviana, for her love, encouragement and support during all those difficult times and helping me stay focused to finish this PhD.

Finally, I would like to express my gratitude to all the people and friends whom I cannot mention one by one in this acknowledgements part for their help and advice during my PhD.

Contents

1 Introduction

A tunneling magnetoresistance (TMR) junction consists of two ferromagnetic materials separated by a non-conducting barrier or insulating material. TMR effect was first observed by Jullière[1] in 1975. TMR junctions have a sensing layer or soft ferromagnetic layer and a stable ferromagnetic electrode which is hard magnetic. The stable ferromagnetic layer serves as the reference electrode. The sensing and reference electrodes are separated by a non conducting barrier layer. By applying an external magnetic field the soft ferromagnetic layer rotates in the direction of external magnetic field first, at higher external field the hard magnetic layer also rotates in the field direction. Fig. 1 shows the parallel and anti-parallel resistance states as a result of external magnetic field (H) and orientation of the soft magnetic layer (FE2) in the direction of H. TMR effect can be defined as:

$$TMR = \frac{\left(R_{ap} - R_p\right)}{R_p} \qquad (1),$$

where R_{ap} and R_p are anti-parallel and parallel resistances states, respectively. In order to use the TMR effect effectively it is important to achieve different switching fields for the rotation of the soft and hard ferromagnetic layers. Stable TMR effect at room temperature was demonstrated by Moodera et al[2]. Since then it has drawn much attention because of its use in magnetic field sensors[3], logic devices[4], read-write heads[5] and in magnetic random access memories (MRAM)[6]. To avoid mechanical interferences in the above mentioned applications low magnetostrictive thin films are preferred.

On the other hand the introduction of highly magnetostrictive thin films intentionally in magnetoresistive junctions can be used in sensing pressure and strain. Strain gauges based on TMR effect and inverse magnetostrictive effect was invented at caesar (center of advanced european studies and research)[7] and has gained much attention due to the high spatial resolution of ~200 nm and extremely high gauge factor from 600[8] to 800[9]. Gauge factor is defined as $(\Delta R/R)/\Delta\varepsilon$, where R is the electrical resistance and ε is the applied strain.

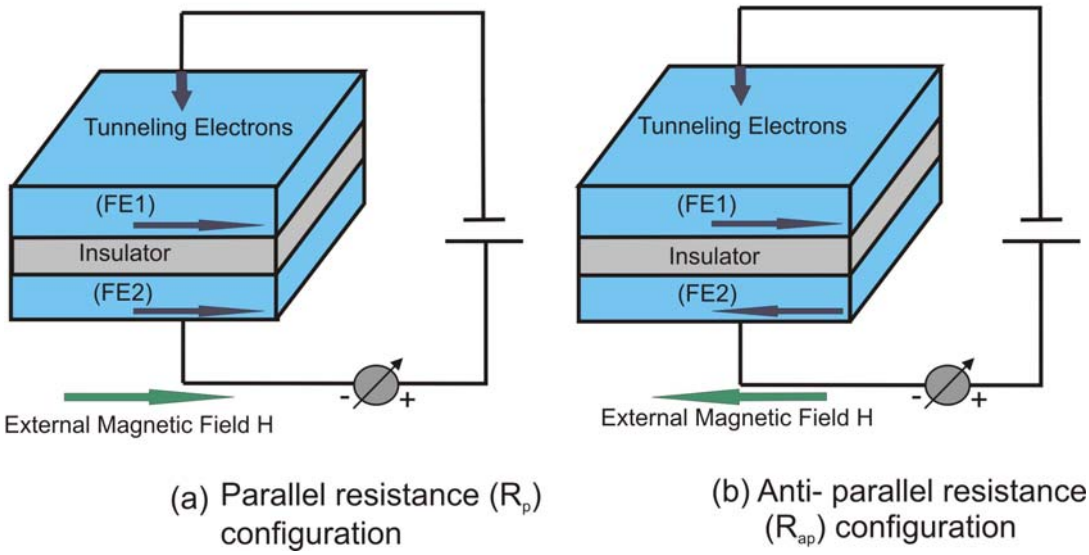

Fig. 1: Tunneling magnetoresistance at (a) parallel resistance (R_p) configuration and (b) anti-parallel resistance (R_{ap}) configuration of the ferromagnetic electrode 1 (FE1) and ferromagnetic electrode 2 (FE2).

$Fe_{50}Co_{50}$ [8] and Metglas[10] were some of the materials used for the fabrication of magnetostrictive free layers in TMR junction for pressure sensitivity[11]. The above mentioned TMR junctions were placed on membranes for the pressure sensitivity applications. The saturation magnetostriction of $Fe_{50}Co_{50}$ is $100*10^{-6}$ and Metglas is $30*10^{-6}$. Replacing these traditional magnetostrictive materials by highly magnetostrictive FeGa[12] shows magnetostriction exceeding $200*10^{-6}$ which will result in high strain sensitivity. Al_2O_3 barrier based TMR junctions show a maximum of 71% tunnel magnetoresistance ratio[13]. It was shown by Ikeda et al.[14] that TMR junctions based on MgO tunnel barrier show TMR ratio as high as 600% at room temperature. High TMR ratios were established in case of epitaxial growth conditions between the magnetic electrodes and the barrier layer[15,16,17]. Butera et al.[18] showed that when FeGa thin film was sputter deposited on MgO (100) oriented single crystal substrate the FeGa crystal cell rotated by 45° on MgO substrate which results in a (100) FeGa || (100) MgO, [110] FeGa || [100] MgO orientation. A lattice mismatch of only 0.7% results in good epitaxial growth of FeGa on MgO (100) substrate. Therefore epitaxially grown tunnel junctions with FeGa and MgO barrier layer could result in high strain sensitivity as well as high TMR ratio. This thesis work is concentrated on developing FeGa electrode and MgO tunnel barrier based TMR junction with high sensitivity to stress and strain, respectively.

2 Fundamentals

2.1 Magnetostriction

It is described most generally as the deformation of a body in response to a change in its magnetization[19]. A Change in the temperature or the magnetic field alters the magnetization of a ferromagnetic material. A linear deformation of a rectangular sample with increasing magnetic field is shown in the Fig. 2. All ferromagnetic materials exhibit magnetostriction and few ferromagnetic elements containing rare earth elements show giant magnetostriction. As shown in fig.2 increasing the magnetic field results in a small change in the length (ΔL). ΔL/L is the strain caused by the magnetic field, denoted by the magnetostriction factor λ. Change in magnetization occurs with respect to the applied external magnetic field until a magnetic saturation value is reached. The value of magnetostriction at the magnetic saturation is called saturation magnetostriction (λ_S).

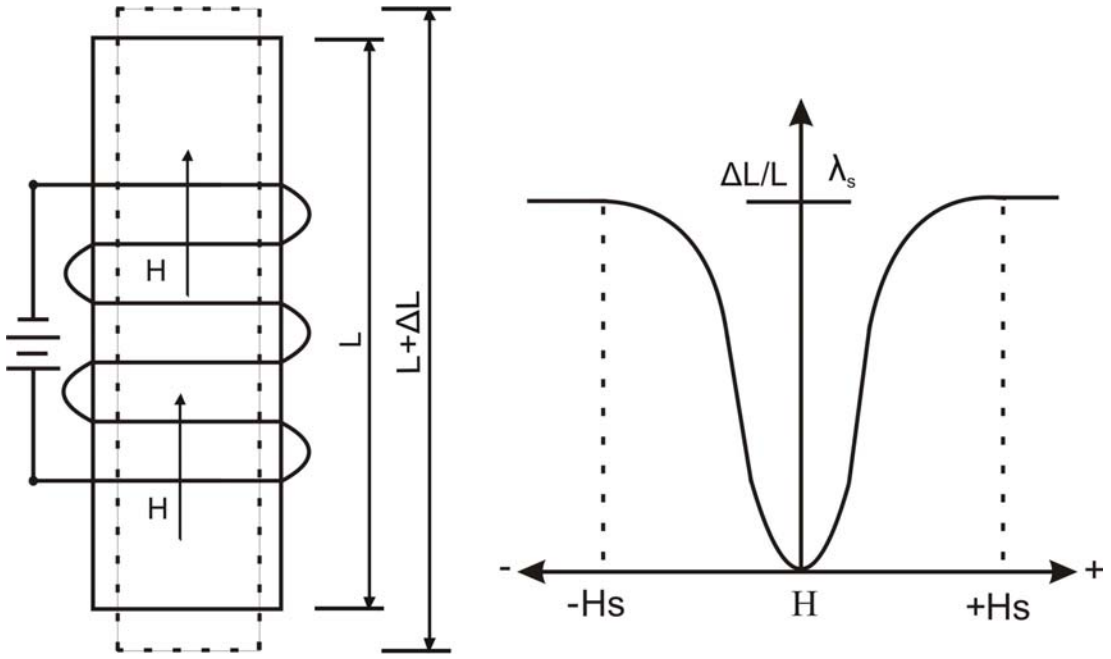

Fig. 2: Linear deformation of a sample by increasing the magnetic field. The direction of the applied field is parallel to the direction of the magnetostriction measurement. [According to Göran Engdahl] [20]

The two types of magnetostriction are Joule magnetostriction and volume magnetostriction. Joule magnetostriction is the change in the shape of the sample in the direction of the applied external magnetic field. In Joule magnetostriction the volume remains almost constant. The Joule magnetostriction factor λ is defined as:

$$\lambda(H) = \frac{\Delta L}{L}(H) \tag{2}$$

The magnetostriction is usually determined by the difference between the energy optimizations (when the direction of the applied field is parallel to the direction of the measurement and the direction of the applied field is perpendicular to the measurement direction). In case of Fig. 2 the direction of the applied field and the direction of the measurement are parallel to each other. Uniform change in the shape of a ferromagnetic material in all dimensions is volume magnetostriction. In most of the cases volume magnetostriction is smaller than Joule magnetostriction. But in case of Invar alloys[21] the volume magnetostriction is larger as compared to other magnetic materials. The volume magnetostriction factor can be defined as:

$$\omega = \frac{\Delta V}{V} \tag{3}$$

All magnetic materials and superconductors are magnetostrictive, but many important technical applications are focused on the soft ferromagnetic materials[22]. When a ferromagnetic material expands in the direction of the external field it is said to exhibit positive magnetostriction. When a magnetic material shrinks in the direction of the field it exhibits negative magnetostriction. The magnetostriction can also be almost zero for some alloys at certain temperatures. The magnetostriction in polycrystals depends on the magnetostrictive properties of the individual crystals and their domain orientation. Considering that the domains are oriented randomly and demagnetized, by applying an external field it is brought to the saturation state, the saturation magnetostriction for polycrystals is anisotropic along different crystallographic axis and can be defined as[23]:

$$\lambda_s = \left(\left(\frac{2}{5}\lambda_{100}\right) + \left(\frac{3}{5}\lambda_{111}\right)\right) \tag{4}$$

where λ_{100} and λ_{111} are saturation magnetostriction when the polycrystalline material is magnetized and the strain is measured along [100] and [111] crystallographic directions of a corresponding single crystal. The saturation magnetostriction λ_s in thin films are measured by two main techniques namely the direct method and the indirect method[24]. The direct method of measurement involves change in the strain state of the cantilever sample due to the change in the magnetization of the sample by applying external saturation magnetic field. In this method the deflection of the tip of the cantilever bimorph is measured by capacitance bridge [25] or with laser deflection technique[26]. In the indirect method of measurement a known strain is applied to the material and a change in the anisotropy is measured. In this method λ_s is measured by applying stress and measuring the change in the ferromagnetic resonance (FMR). During this work the saturation magnetostriction λ_s of the cantilever bimorph was measured by the laser deflection technique. The method of measurement is discussed in detail in section 3.3.3

2.2 Inverse magnetostriction

The inverse magnetostriction is the change in the magnetization of a material due to external compressive stress or tensile stress. The stress dependence of the magnetization on the iron wires was studied extensively by Villari.[27] Thus inverse magnetostriction is also known as the Villari effect.

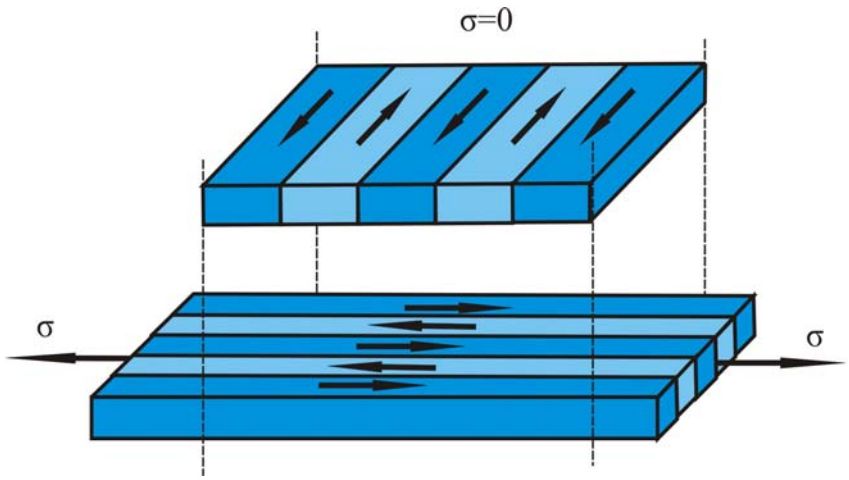

Fig. 3: Schematic representation of inverse magnetostriction effect for a positive magnetostrictive material

Fig. 3 shows a schematic representation of the effect of tensile stress on a positive magnetostrictive material. On applying a large tensile stress the magnetization of the material rotates in the direction of the applied stress. When no stress is applied the magnetization rotates back to its original position. If a compressive stress is applied to a positive magnetostrictive material the magnetization will rotate perpendicular to the direction of the stress. Force sensors[28] and pressure sensors[8] are some of the applications based on the inverse magnetostrictive effect.

2.3 Tunneling effect

According to quantum mechanics electrons can tunnel through a thin insulating dielectric material of few nanometers thickness (Fig. 4) known as the tunnel barrier even when the particle does not have sufficient energy to pass over it. In classical physics electrons cannot pass through the tunnel barrier, they are reflected. Tunneling probability depends on the thickness of the barrier and the wave vector. Tunneling effect can be explained by means of applying one dimensional Schrödinger equation to the areas (1), (2) and (3) in Fig. 4:

$$\frac{2m}{\hbar^2}(E-U)\Psi+\frac{\partial^2\psi}{\partial x^2}=0 \qquad (5)$$

Where E gives the energy of the particle, U the barrier potential, Ψ is the wave function, $\hbar$ is the Planck's constant and m the mass of the particle.

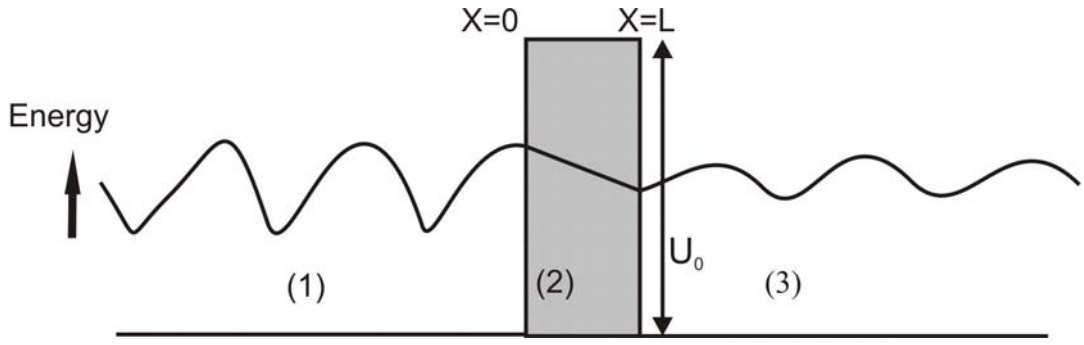

Fig. 4: Tunneling of electrons. An electron wave which has a certain amplitude and velocity is incident on the left side of the barrier of height U_0 and thickness L. In classical mechanics the particle would be reflected. But in quantum mechanics, if the barrier is not too thick the electron wave appears on the right side with lower amplitude as compared to its original amplitude.

Let us consider electrons of kinetic energy E, incident from the left of the potential barrier of height U_0 and width L. The wave function Ψ_1 represents the incident particles, Ψ_2 represents the wave function of particles inside the barrier some of which reach the area (3) while others are reflected back to area (1). Ψ_3 is the transmitted particles wave function moving to the right of the barrier. On both sides of the barrier (area (1) and (3)) no forces act on the particles, therefore U=0. Inside the barrier the particles experience a potential U. The potential is assumed to be step-like and by solving the Schrödinger equations we get the following solutions[29] for area (1) and (3) as:

$$\Psi_1 = A_1 e^{ik_1 x} + B_1 e^{-ik_1 x}, \quad k_1 = \sqrt{E * \frac{2m}{\hbar}} \tag{6}$$

$$\Psi_3 = E_1 e^{ik_1 x} + F_1 e^{-ik_1 x}, \quad k_1 = \sqrt{E * \frac{2m}{\hbar}} \tag{7}$$

Equation (6) can be rewritten as

$$\Psi_1 = \Psi_{1+} + \Psi_{1-} \tag{8}$$

Where $\Psi_{1+} = A_1 e^{ik_1 x}$ represents the incoming wave and $\Psi_{1-} = B_1 e^{-ik_1 x}$ denotes the reflected wave and k_1 is the wave vector of the de Broglie´s waves that represent the particle outside the barrier.

At x>L there can be only transmitted wave as there is nothing to reflect the wave in the region (3). Therefore Ψ_3 is rewritten as:

$$\Psi_3 = E_1 e^{ik_1 x} \tag{9}$$

From equations (6) and (7) the wave vector outside the barrier k_1 is always a real number independent of E and therefore represents a propagating wave outside the barrier. When 0<x<L, the Schrödinger equation for area (2) is:

$$\frac{2m}{\hbar^2}(E - U_0)\Psi_2 + \frac{\partial^2 \psi_2}{\partial x^2} = 0 \tag{10}$$

Since the energy of the barrier is greater than the energy of the particle the solution for equation (10) is

$$\Psi_2 = C_1 e^{-k_2 x} + D_1 e^{k_2 x},\ k_2 = \sqrt{(E - U_0) * \frac{2m}{\hbar}} \qquad (11)$$

Here, k_2 is the wave vector inside the barrier. The exponents of wave vector Ψ_2 are real and so it does not represent a moving particle. Since the probability density of Ψ_2 is not zero, there is a probability to find the particle inside the barrier. When E is less than U_0, k_2 becomes imaginary and the wave is decaying inside the barrier or reflected to area (1). Since E is not zero at x=L the particle is transmitted, which means the particle has a finite chance of tunneling the barrier.

2.4 Magnetoresistance effects

A change in the electrical resistance of a material when subjected to an external magnetic field is referred to as magnetoresistance effect[23]. Some of the important magnetoresistance effects to be mentioned are the anisotropy magnetoresistance (AMR), the giant magnetoresistance (GMR), and the tunneling magnetoresistance (TMR) effects, respectively.

2.4.1 Anisotropic magnetoresistance (AMR)

The physical origin of anisotropic magnetoresistance is the spin-orbit coupling. Applying an external magnetic field rotates the saturation magnetization in the direction of the field, resulting in the deformation of electron cloud around the nucleus. This deformation changes the amount of scattering of the conduction electrons in the lattice of the material. The resistivity of the material depends on the relative orientation of the electrical current and magnetization of the material. All materials show anisotropic magnetoresistance but the effect is large only in ferromagnetic metals and alloys such as NiFe and NiCo[30, 31]. Large AMR ratio is noticed for $Ni_{70}Co_{30}$ which equals 6-7% at room temperature and 27% at 4.2 K[31]. The AMR ratio of the NiCo alloys as a function of the composition at room temperature is shown in the Fig. 5.

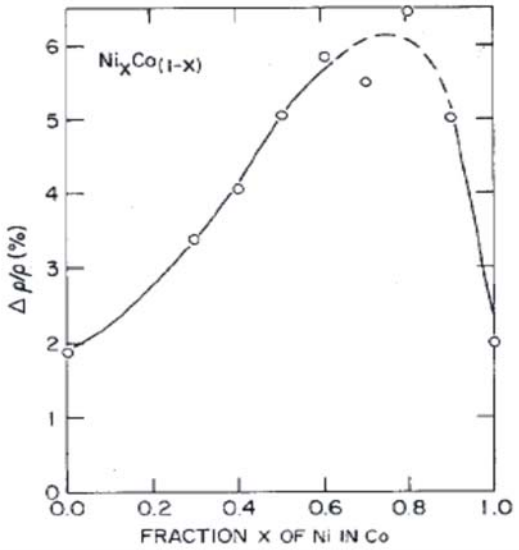

Fig. 5 : Anisotropic magnetoresistivity ratio of the $Ni_xCo_{(1-x)}$ alloys at room temperature[32,33] [Taken from Mc Guire et al[31]]

2.4.2 Giant magnetoresistance (GMR)

When an external magnetic field is applied to a multilayer film it changes the relative orientation of the magnetization in the adjacent magnetic layers resulting in a large change in film resistance, known as GMR effect.

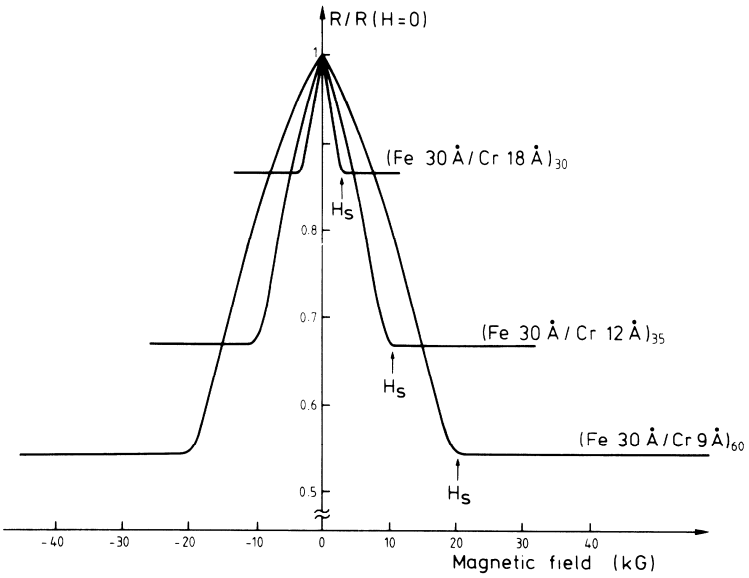

Fig.6: GMR effect of three Fe/Cr super lattices at 4.2 K (from Fert et al.[34])

This effect was discovered independently in 1988 by Fert et al [34] and Grünberg et al [35] in anti-ferromagnetically coupled Fe/Cr multilayered structures. Thin layers of magnetic Fe (3 nm) films were separated by non-magnetic Cr layers (0.9, 1.2 and 1.8 nm). Depending on the thickness of the non-magnetic Cr layers the moments of Fe layers were coupled to each other to be either anti-ferromagnetic or ferromagnetic. If the moments of Fe were anti-ferromagnetic or anti-parallel the resistance is high and by applying a sufficiently high magnetic field the moments can be forced to align in one direction. This results in a low resistance state. The high and low resistance states of Fe/Cr multilayer with varying thicknesses and varying saturation magnetization (H_s) can be seen in Fig.6. The spin dependent scattering of conduction electrons[36] is believed to be the origin of giant magnetoresistance. Fe/Cr based GMR experiments required low measurement temperature and fields as large as 20 kG to rotate the magnetization from anti-ferromagnetic configuration to the ferromagnetic configuration (from the anti-parallel to the parallel configuration).

Parkin et al[37] and Kano et al[38] studied Co/Cu multilayed GMR structures and succeeded in achieving room temperature GMR ratio of 65% and 80% (Fig. 7) respectively. The highest GMR ratio of 220% was measured by Schad et al.[39] at 1.5 K for Fe/Cr multilayered system.

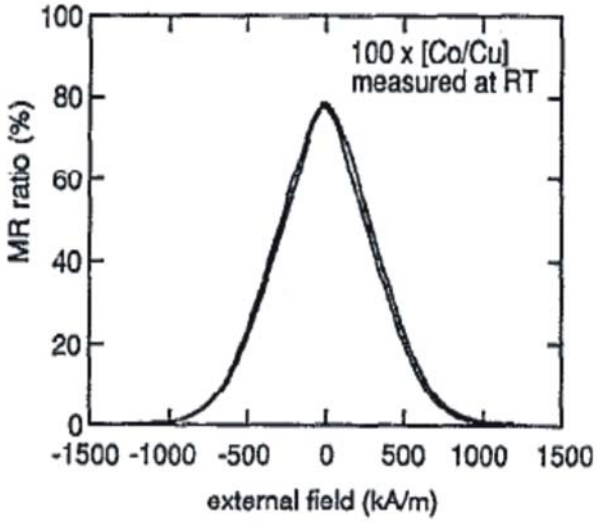

Fig. 7: GMR ratio versus external field for a Co/Cu multilayer at 20°C showing 80% GMR ratio [Taken from Kano et al[38]]

To overcome the draw backs of high saturation field and low experimental temperatures relatively simple setup that can be operated at room temperature called spin valve was developed. Spin valves consists of an anti-ferromagnetic layer which pins the ferromagnetic layer by exchange bias coupling in one orientation. This pinned ferromagnetic layer is separated by a non- magnetic layer and a ferromagnetic layer (free layer) which is free to switch its orientation in both directions by applying a magnetic field (see Fig.8). The magnetization of free layer can be changed by applying a relatively small external field. GMR spin valves are used in the magnetic read heads of hard disk drive[41] and in magnetic random access memory (MRAM)[40].

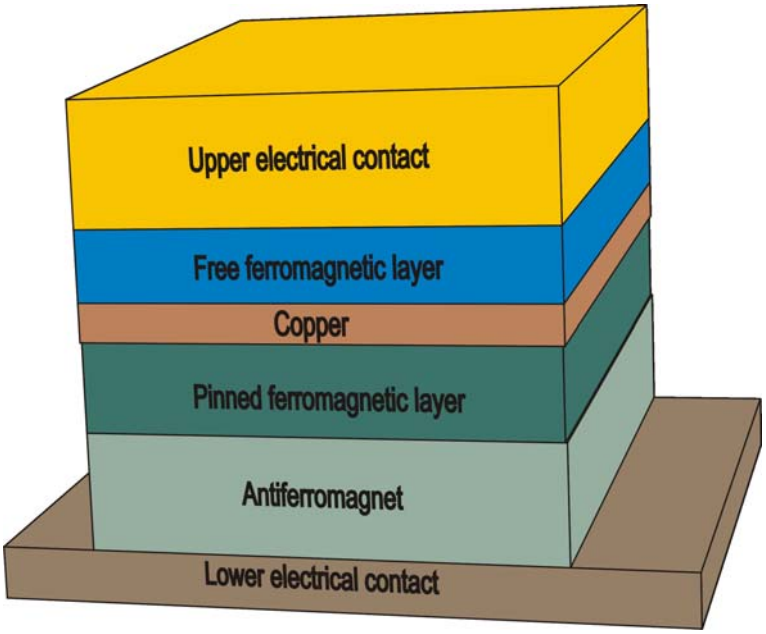

Fig.8: Basic structure of spin valve GMR junction [41]. One of the ferromagnetic layer is pinned by an anti-ferromagnetic layer and the other ferromagnetic layer is free to rotate under external fields.

The use GMR junctions for applications such as stress, strain and pressure sensors [42, 43] were investigated by only a few groups. Löhndorf et al[44] investigated the use of magnetostrictive materials as sensing layer in GMR junctions. They measured magnetoresistance ratio at room temperature of the order of 3 to 4 %. The gauge factor of these junctions were expected to be between 15 to 40.

2.4.3 Tunneling magnetoresistance (TMR)

A tunneling magnetoresistance junction consists of two ferromagnetic electrodes separated by a thin insulating barrier layer. The insulating layer is just a few nanometers thick. If a bias voltage is applied between the two metal electrodes the electrons tunnel through the barrier.

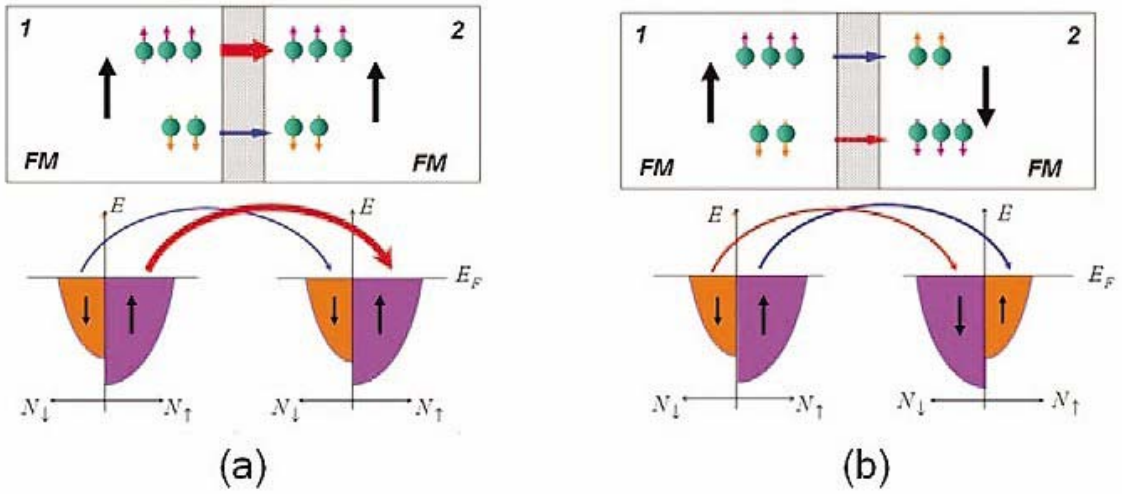

Fig. 9: The schematic of TMR effect showing electrons tunneling towards the positive electrode (from the FM1 to FM2) when a bias voltage is applied (not shown in the figure above). Upper row: Parallel and anti-parallel configuration of a TMR element. Lower row: The density of states (DOS) of the electrons depends on the orientation of their spin relative to the magnetization of the layer[45]

The electric current passing through a ferromagnetic material consists of spin-up and spin-down electrons (Fig. 9). During the tunneling process it is assumed that the spins of the electrons are conserved. So the spin-up electrons can tunnel only into the spin-up sub-band and vice-versa. Depending on the parallel or anti-parallel magnetization of the electrodes the conductance in TMR junction increases or decreases. When the spin of electrons are parallel to the magnetization, the density of states (DOS) of electrons parallel to magnetization are shifted down resulting in a large DOS at Fermi level E_F. Fig. 9a shows the magnetization orientation of both ferromagnetic electrodes parallel to each other. In this case many spin-up electrons can pass through the barrier, known as low resistance state. The contribution of the spin-down electrons is low, because “they are few” and there are only few available states in the counter electrode. To sum up the

overall resistance is low. Fig. 9b shows the magnetization of ferromagnetic electrodes anti-parallel to each other. The density of states of spin down electrons is shifted up on the left side and on the right side it's shifted down. This results in small current and the same holds also for the spin up electrons. The overall resistance is high. The relative change in the resistance defines the TMR ratio as shown in equation (1).

In order to achieve full TMR ratio a well separated parallel (P) and anti-parallel (AP) configuration of the electrodes is important in magnetic tunnel junctions. The above mentioned configuration can be achieved in a TMR junction in two ways as shown in Fig. 10. Fig. 10a. shows the TMR versus applied cyclic magnetic field for junctions consisting of two ferromagnetic (FM) thin films with different coercive field (hard and soft magnetic thin film) which can bring about well separated rotation of the electrodes resulting in P and AP configuration of magnetization.

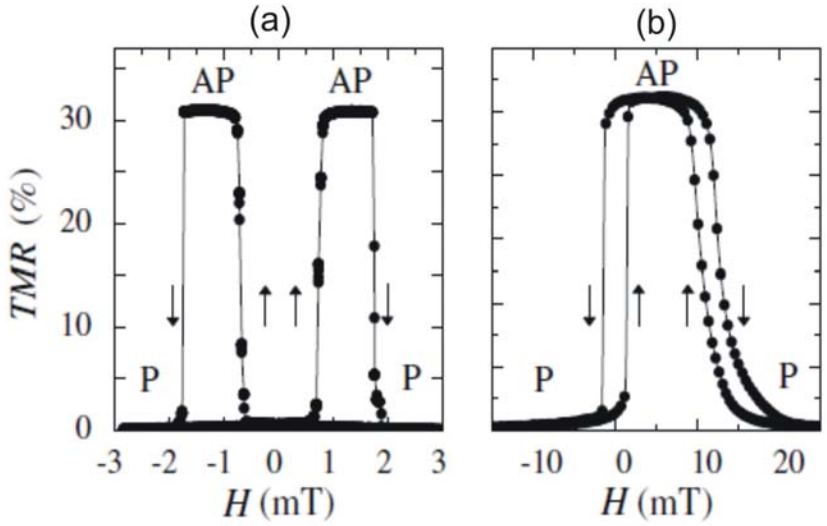

Fig. 10: Magnetoresistance versus magnetic field for (a) hard-soft magnetic tunnel junction, (b) exchange-biased magnetic tunnel junction. P represents parallel and AP the anti-parallel configuration of magnetization of electrodes[46]

Another way to realize the P and AP configuration is by means of exchange bias based TMR junctions. To achieve exchange bias one of the electrodes is deposited directly on top of an anti-ferromagnetic (AFM) thin film (NiO, PtMn). The exchange biased (FM/AFM) interface acts as a hard magnet and shifts the magnetization of the TMR loops away from zero field. The mechanism of exchange bias is discussed further in section 2.5. Exchange biased TMR junctions are preferred over the hard-soft magnetic junctions as

the change from P to AP configuration takes place near the zero field and these junctions have a better magnetic stability. The TMR ratio as a function of applied field for exchange biased TMR junction can be seen in Fig. 10b. Exchange biased TMR junctions are used in MRAM[47] and in many other technologically important applications.

The relative orientation magnetizations of the two magnetic layers determine the tunneling probability and the tunneling resistance. In non-magnetic metallic materials the spin-up and spin-down electrons have the same density of states (DOS) at the Fermi level, which results in the equal tunneling probability for electrons. Because of exchange splitting of the electronic bands in ferromagnetic metals the spin-up and spin down electrons have different DOS at the Fermi level resulting in different tunneling probability (Fig. 11).

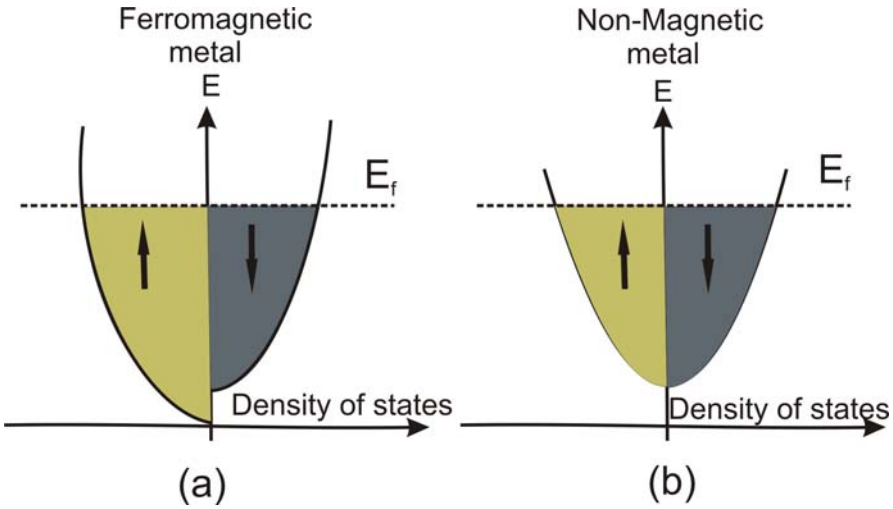

Fig. 11: Density of states of the spin-up (up arrow) and spin down (down arrow) electrons at the Fermi energy (E_f) for (a) Ferromagnetic metal and (b) non-magnetic metal

Spin dependent tunneling was discovered by Tedrow and Meservey[48,49,50]. They used superconductor/insulator/ferromagnetic films based tunnel junctions to measure the spin polarized tunnel current.

Later Jullière[1] came up with a simple model to explain TMR with respect to the spin up and the spin down polarizations P_1 and P_2 respectively. His theory was based on two assumptions. First the spin of the electrons is conserved during tunneling. Secondly the tunneling probability was assumed to be same for both spin up and spin down electrons. A demonstration of the

TMR effect by Jullière can be seen in Fig. 12. Based on these assumptions TMR ratio was expressed as:

$$\text{TMR ratio} = \frac{2 * P_1 P_2}{1 - P_1 P_2} \tag{12}$$

The spin polarization was expressed in terms of spin resolved density of states $N_\uparrow$ the majority spins and $N_\downarrow$ the minority spins in ferromagnetic electrodes as:

$$P \equiv \frac{N_\uparrow - N_\downarrow}{N_\uparrow + N_\downarrow} \tag{13}$$

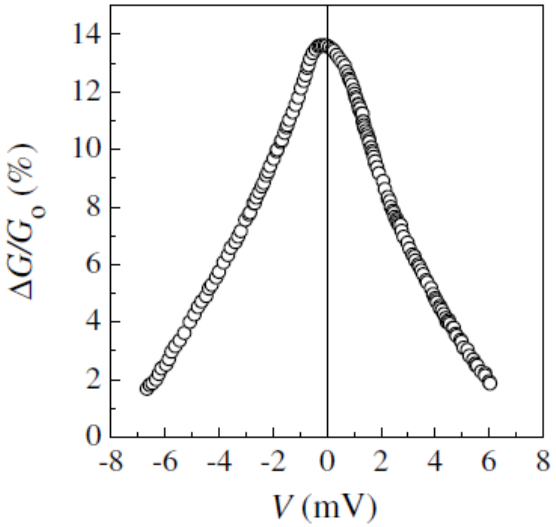

Fig. 12: The Original demonstration of the TMR effect at 4.2 K. (after Jullière[1])

Jullière's model was simple, but tunneling does not depend only on the number of electrons on the Fermi level but also on their tunnel probability. This is different for different electronic states. Stearns[51] pointed out that tunneling depends on the effective mass of electrons which is different for different band structures. The electronic bands that dominate tunneling are similar to the free electrons and the DOS of these bands at Fermi level is equal to their Fermi wave vectors. Therefore we can rewrite the spin polarization as:

$$P = \frac{k_\uparrow - k_\downarrow}{k_\uparrow + k_\downarrow} \tag{14}$$

where $k_{\uparrow}$ and $k_{\downarrow}$ are the Fermi wave vectors of the majority spins and minority spins respectively.

A more appropriate model for spin polarized tunneling effect was given by Slonczewski[52]. He considered tunneling through rectangular potential barrier of height U and distance d between two identical ferromagnetic electrodes. The ferromagnets were assumed to be two parabolic bands strongly shifted against each other by means of exchange coupling. He also assumed that the electrons undergo a coherent tunneling and by solving the Schrödinger's equation the conductance was determined with respect to the relative magnetization orientations of the ferromagnets. He found the effective spin polarization of electrons as[54]:

$$P = \left(\frac{k^{\uparrow} - k^{\downarrow}}{k^{\uparrow} + k^{\downarrow}}\right)\left(\frac{\kappa^2 - k^{\uparrow}k^{\downarrow}}{\kappa^2 + k^{\uparrow}k^{\downarrow}}\right) \tag{15}$$

Here κ is the constant of decay of the wave function into the barrier and is determined by the potential barrier height, U and $k^{\uparrow}$ and $k^{\downarrow}$ are the Fermi wave vectors of the majority and minority spins.

$$\kappa = \sqrt{\left(2m/\hbar^2\right)\left(U - E_F\right)} \tag{16}$$

Polarization depends on the height of the barrier. For high barriers the effective spin polarization becomes unity and Slonczewski´s formula is reduced to Jullière's. For low barriers the effective spin polarization decreases with decreasing height of the barrier and changes sign for very low barriers, which can be seen in Fig. 13.

This was the first important observation that the spin polarization depends not only on the electronic structure of the ferromagnetic electrode but also depends on structure and electronic properties of tunnel barrier and also the interface properties between the electrode and barrier. Slonczewski´s model can be used for describing epitaxially grown barriers and crystalline MgO barrier[53,15] based TMR junctions as this model assumes that the electrons tunnel through the barrier keeping the wave coherency.

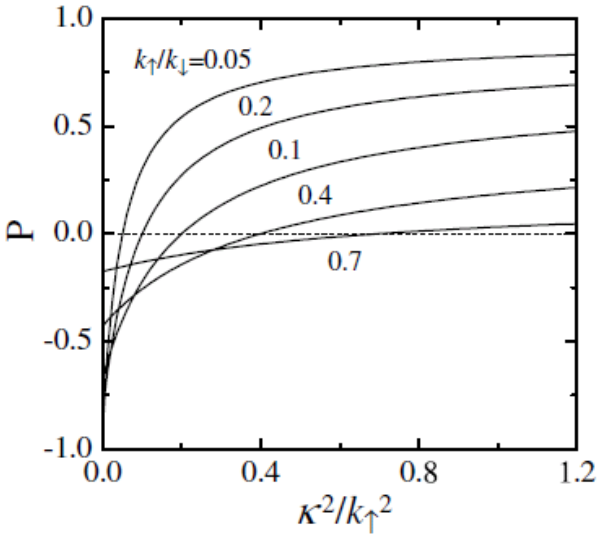

Fig. 13: Spin polarization of the tunneling conductance as function of the normalized potential barrier height for various values $k^{\uparrow}/k^{\downarrow}$ [54]

TMR junctions fabricated based on MgO tunnel barriers show TMR ratio from a few 100 % [55,56] to as high as 600 % [14] at room temperature. The application of these TMR junctions were demonstrated in logic devices, read write heads and in MRAM. But only a very few research has been performed in the fabrication of strain sensors based on the TMR effect[57,58]. Löhndorf et al [8, 44] prepared TMR junctions based on Al_2O_3 barrier layer and introduced intentionally magnetostrictive sensing layer like $Fe_{50}Co_{50}$. They achieved TMR ratio as high as 48% and also reported gauge factor in the order of 300 and 600. They further suggested that to develop strain sensors based on the magnetostrictive and magnetoresistance effect TMR junctions are favourable over GMR junctions due to high TMR ratio and high gauge factors. Further Meyners et al[9] fabricated TMR junction based strain sensors with MgO barrier layer which showed 120% TMR ratio and the highest strain sensitivity of 800.

2.5 Exchange bias

Exchange coupling between a ferromagnet (FM) and an anti-ferromagnet (AFM) result in the effect called exchange bias[59]. This phenomenon was first discovered by Meiklejohn and Bean in 1956[60,61] during the study of Co particles coupled with a naturally oxidized cobalt oxide anti-ferromagnetic material.

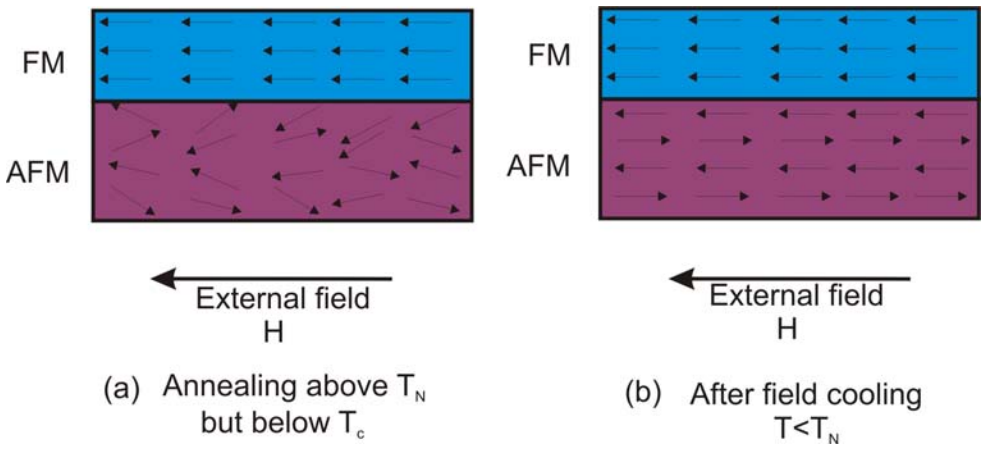

Fig. 14: Mechanism of establishment of exchange bias coupling

Fig. 14 shows the mechanism of formation of an exchange bias. Exchange biasing can be achieved by depositing a ferromagnetic film on top of an anti-ferromagnetic film, the FM/AFM film are heated above the Neel temperature (T_N) of the AFM but below the Curie temperature(T_c) of the ferromagnetic film. Due to this process the moments of the AFM are oriented randomly because of the thermal fluctuation induced by the annealing process. Cooling down below the T_N in the presence of a strong external magnetic field (H) pins or freezes the magnetic moments of anti-ferromagnetic film parallel to the moments of the ferromagnetic film at the boundary between FM/AFM. The result is a shift in the magnetization loop of FM horizontally in the positive or negative direction (shown in Fig.15b). If the shift of the hysteresis loop is in the direction of the external magnetic field the sample is said to be positively exchange biased. If the shift appears in the opposite direction of field, the FM/AFM junction is negatively exchange biased.

When an external magnetic field is applied to the exchange biased FM/AFM interface, the moments of FM starts to rotate in the direction of the field. The moments of a hard AFM will not rotate in the direction of field. This will result in high exchange bias. If the AFM is soft, the uncompensated spins in the form of a spring will be aligned at the interface between FM and AFM resulting in the reduction of the exchange bias. The magnitude of the exchange bias can be calculated by the following equation as[62]

$$H_{EB} = \frac{n}{\mu_0} \frac{J_{EB}}{M_s t_{FM}} \qquad (17)$$

Where n is the number of interfacial spin coupling per unit area, J_{EB} is the exchange constant at the interface; M_s is the saturation magnetization of the FM and t_{FM} the thickness of the FM. The exchange biases in the real systems are reduced as compared to theoretical predictions. This reduction is due to the reduced pinned moments at the interface which accounts to only a few percent of a monolayer. The domain wall formation also reduces the exchange bias field.

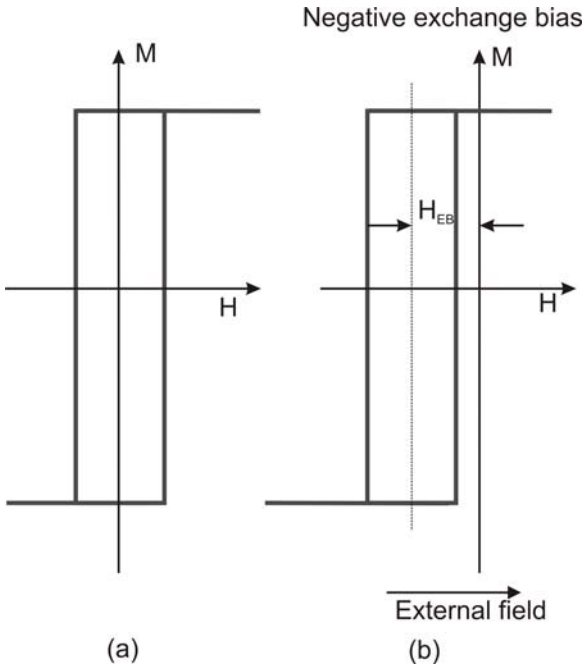

Fig.15: (a) Magnetization loop of a ferromagnetic material along the easy axis of magnetization, (b) Hysteresis loop horizontally shifted by a bias field H_{EB} of a FM by exchange coupling with AFM. The sample is negatively exchange biased if the loop shifts in the direction opposite to the external field direction.

2.6 State of the art of FeGa thin films

FeGa alloy was developed at Naval surface warfare center by Clark et al[87]. They showed that quenched bulk FeGa single crystals are highly magnetostrictive in (100) crystallographic orientation. They reported magnetostriction $(3/2)\lambda_{100}$ as high as 400 ppm at 19 at% Ga and a second large magnetostriction close to 27 at % of Ga. This alloy is ductile and can withstand high tensile and shear stresses which makes it a good choice for

the fabrication of actuators and sensors in the form of FeGa thin films. Butera et al[18] prepared FeGa thin film epitaxially on MgO(100) substrate under optimum argon (Ar) pressure of ~ $4*10^{-3}$ mbar and at low sputter powers. Wang et al[86] studied the effect of forming field on the FeGa films and found that FeGa thin films sputtered with magnetic forming field show an increase in the magnetostriction. They concluded that this increase in magnetostriction is due to an in-plane induced anisotropy of FeGa.

Magnetostriction of FeGa thin films were studied by many groups[102,86,104] and the values reported vary between 50-$147*10^{-6}$. Javed et al[104] investigated the effect of sputter power on the soft magnetic property of FeGa thin films and found out that sputter pressure of $3*10^{-3}$ mbar results in soft magnetic FeGa films. They further reported that increase in the pressure above $3*10^{-3}$ mbar resulted in change in the residual stresses during the growth, as a result the film became magnetically isotropic. ME sensors[63, 64] and the acoustic sensors[65] were some of the FeGa thin film based sensors. The above mentioned magnetostrictive, anisotropy and soft magnetic properties of FeGa thin film makes it an interesting candidate to be used in TMR junctions based pressure sensors.

3 Experimental methods

The fabrication and characterization techniques used during this work will be described briefly in this chapter. Fabrication procedures of two basic TMR junctions described below will be discussed:

- Thick FeGa electrode and thin FeGa electrode based magnetostrictive TMR junctions and
- Exchange biased magnetostrictive TMR junctions with FeGa sense layer and MgO tunnel barrier

The characterization techniques include structural, magnetic, electrical and strain characterization.

3.1 Fabrication techniques

FeGa based thin films and the TMR junctions were fabricated at the clean room facility of the *Kieler Nanolabor*. First the fabrication techniques in general will be discussed. A brief explanation of two types of the magnetostrictive TMR junctions fabricated will be discussed. Various steps involved during the fabrication of the above mentioned TMR junctions are represented in Fig. 16. Each process is discussed briefly below in the following sub-chapters.

3.1.1 Pre-cleaning of substrate

The MgO single crystal substrates were purchased from Crystec[66] and SWI Semiconductor Wafer, Inc.[67]. The dimensions of various substrates are as follows: 10 mm x 10 mm x 1 mm, 20 mm x 20 mm x 0.5 mm and 20 mm x 2 mm x 0.25mm. Before sputter deposition of various TMR stacks on MgO (100) oriented single crystal substrates, the substrates were cleaned by Ar-ion etching inside the Ardenne CS 730 S cluster deposition tool (see 3.1.2). The etching process is important to remove the hydroxyl groups formed during the storage and transfer process of MgO substrates.

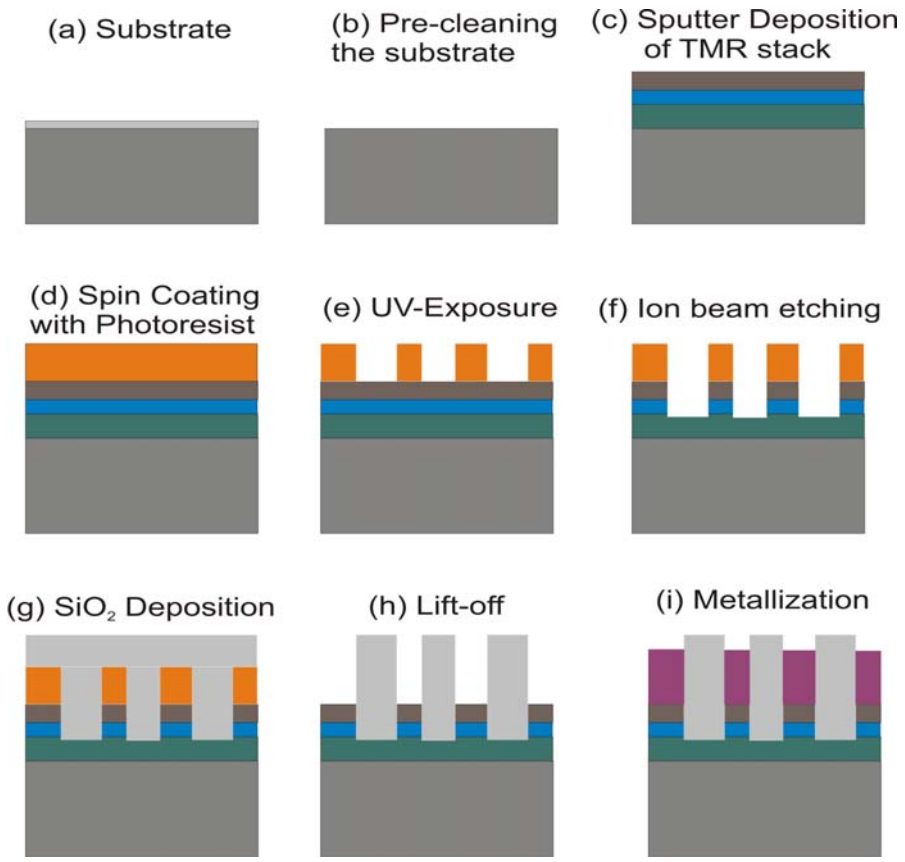

Fig. 16: Schematic showing the fabrication steps of TMR junctions

3.1.2 TMR stack preparation by magnetron sputter deposition

A Von Ardenne CS 730 S magnetron sputter depositing cluster tool was used to produce FeGa thin films and TMR junctions. The cluster sputter depositing tool has two chambers as shown in Fig. 17 on the right and left side each equipped with 4 sputter targets and an etch chamber in the middle. Left sputter chamber has two 8 inch sputter targets and two 4 inch sputter targets with two magnetic positions for the substrate. The right sputter chamber has one 4 inch sputter target and three 8 inch targets available to be used for sputter deposition. The base pressure of the sputter chambers were $2*10^{-7}$mbar before sputter deposition of TMR junctions. DC and radio frequency (RF) sources were used to generate plasma. The substrate can be heated at one of the four possible positions in the right and left chambers respectively. The heaters can heat to a maximum of 500°C. An additional in plane magnetic field of 9-12 mT could be supplied to the sample in the left chamber by means of two permanent magnets.

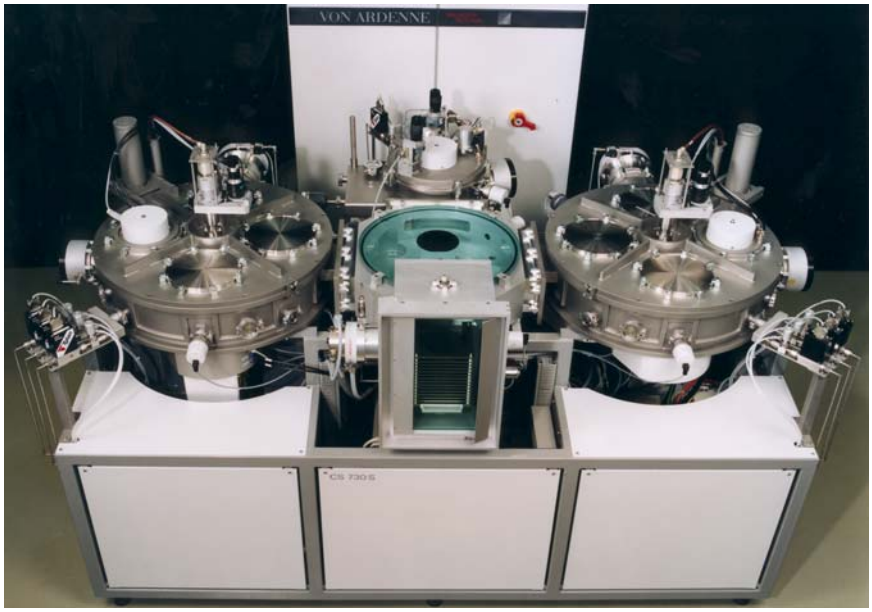

Fig. 17: Von Ardenne CS 730 S magnetron sputter depositing cluster tool

Two types of power sources were utilized for the sputter deposition of thin films namely :

(a) DC magnetron sputter deposition which works well for metals and
(b) RF magnetron sputter deposition

RF (radio frequency) plasma sputter deposition is preferred over DC for a few reasons:

- RF plasma allows sputtering of both metals and dielectrics.
- Sputter deposition can be carried out in lower pressure as compared to DC plasma sputter deposition.

An RF voltage usually in MHz and preferably 13.56 MHz (as it doesn't interfere with radio-transmitted signals) is applied between the target (cathode) and substrate (anode). Therefore the anode and the cathode are electrically reversed for a short period of time. It eliminates build up of charge on an insulating surface and provides an equal number of ions and electrons. This allows sputter deposition of insulators and also metals. Secondary electron emission from cathode is therefore not required to sustain plasma. The oscillating RF field imparts enough energy to the electrons to ionize the argon atoms, therefore the plasma can sustain even at low pressures. This oscillating field also increases plasma density, higher

ion-current and faster sputtering process. The process parameters used for the sputting of FeGa and other thin films for the deposition of the TMR stacks are shown in the table below:

Element	Power (W) RF/DC	In plane magnetic field	Pressure (mbar)	Deposition Rate (nm/sec)
FeGa	20, RF 200, RF	Field	$4*10^{-3}$	0.006 0.04
MgO	300, RF	No field	$1.2*10^{-3}$	0.03
Ta	200, DC	No field	$4*10^{-3}$	0.33
Ru	100, RF	Field	$4*10^{-3}$	0.14
Au	200, DC	No field	$6*10^{-3}$	1.10

Table 1: The parameters used for the sputter deposition of the thin films for the fabrication of TMR junctions.

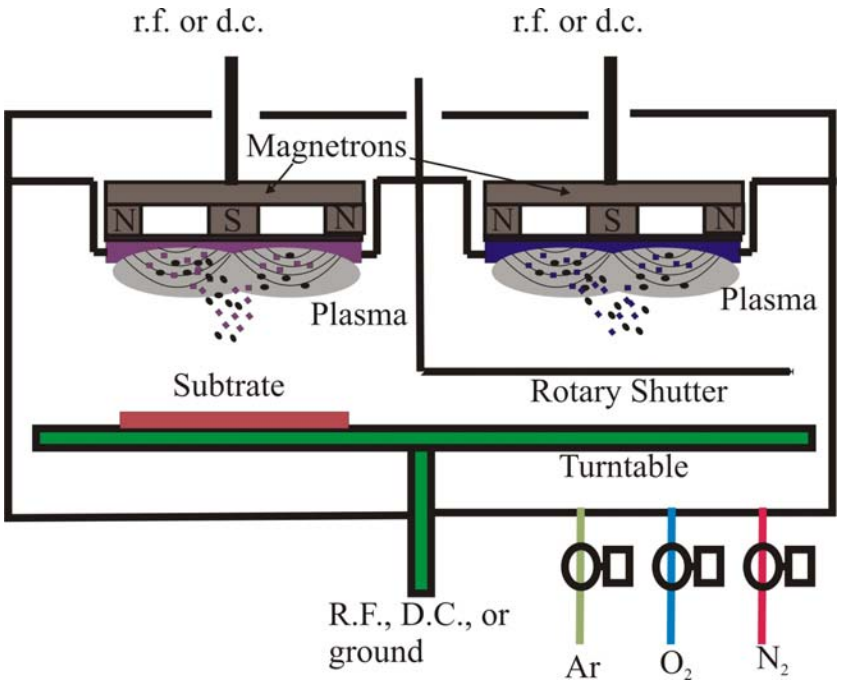

Fig.18: Schematic of magnetron sputter deposition[68]

Magnetron sputter deposition is one of the most widely used commercial thin film deposition techniques. The deposition rates are typically higher in magnitudes than those achieved by conventional sputtering techniques. It

utilizes magnetic field crosswise over the cathode (Fig.18). This magnetic field increases the mean free path of the electrons thus prolongs the residence time of the electrons in the plasma increasing the probability of ion collision. The electrons within the magnetic field of the magnetron experience the Lorentz force. The minimum pressure required to sustain the plasma is much lower as the travel path of electrons is longer than the electrode gap. The ionization of plasma near the target increases the sputter rate. It also eliminates the bombardment of the substrate by secondary electrons, which is a main source of unwanted sample heating. Magnetron sputter deposition can be used for both DC and RF power sources.

3.1.2.1 Fabrication of thick FeGa electrode and thin FeGa electrode based magnetostrictive TMR junctions

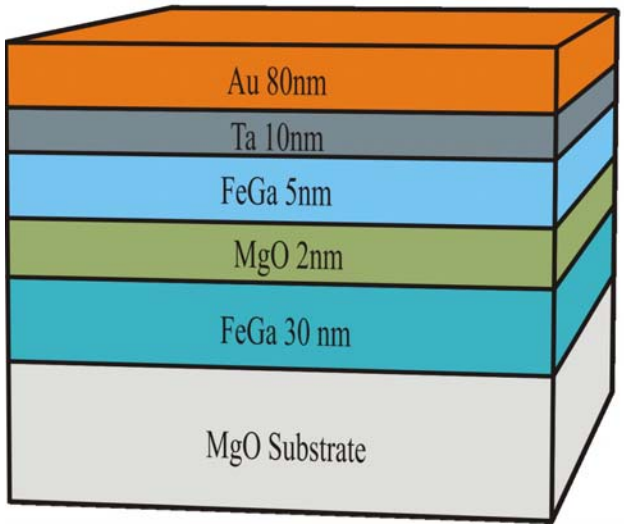

Fig.19: Stack configuration of thick and thin FeGa electrode based TMR junction.

The MgO single crystal substrates were argon etched for one minute to clean the surface and for better growth conditions[69]. The cluster deposition tool CS 730 S was used to sputter deposit the TMR stacks with the configuration shown in Fig.19. FeGa thin film was sputter deposited at a sputter power of 200 W and argon pressure of $4*10^{-3}$ mbar. MgO thin film was sputter deposited at 300 W sputter power and $1.2*10^{-3}$ mbar argon pressure. Both FeGa and MgO are sputter deposited by radio frequency (RF) power supply.

3.1.2.2 Fabrication of exchange biased magnetostrictive TMR junctions with FeGa sense layer and MgO tunnel barrier

The exchange bias based TMR junctions have the stack configuration as in Fig. 20. The TMR stack until the MgO barrier layer was sputter deposited by Siemens AG[70]. A 20 nm FeGa thin film was sputter deposited at a low sputter power of 20 W and argon pressure of $4*10^{-3}$ mbar. In the first set of wafers FeGa was directly deposited on 2 nm CoFeB as shown in Fig. 20 below, followed by tantalum and ruthenium top electrodes. In another set of wafers the MgO barrier layer was protected by 6 nm CoFeB. Before depositing FeGa electrode, 2 nm of the CoFeB was etched to clean the surface. The stack has the same lower electrodes configuration and the contact electrodes as in Fig. 20.

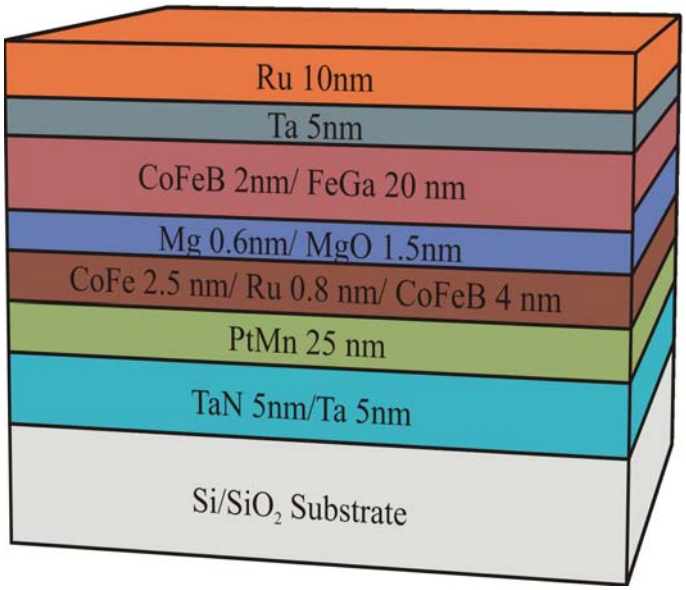

Fig. 20: General stack configuration of exchange bias based TMR junction

3.1.3 Priming and spin coating

The sputter deposited TMR junction sample was treated with a primer before spin coating to enhance adhesion of the photoresist to the sample surface. Hexamethyldisilazane (HMDS) is one of the typical adhesion promoters, used during this work. The samples were primed at 100°C exposed to HMDS vapor under N_2 gas atmosphere. The sample was clamped in a vacuum chuck and photoresist was dispensed on the sample. The sample

was spun at low speed first to spread the resist over the substrate and spinning at high speed later to achieve final thickness[71]. This also helps to achieve a uniform thickness of resist on the sample. A soft bake was performed at about 110°C to increase the adhesion of the resist to the sample and to reduce the remaining solvent concentration and built-in stresses.

3.1.4 UV Lithography

UV exposure of the spin coated TMR junctions were performed in a Süss Microtec MA6 mask aligner. The device is equipped with a 350 W Hg lamp as the power source which generates an intensity of 33 mW/cm^2 at the substrate. Different mask structures used for the fabrications of TMR junctions are shown in Fig. 21 and Fig. 22. Fig. 21 is the mask used for the fabrication of thick and thin film FeGa electrode based magnetostrictive TMR junctions. The mask consists of junctions sizes varying from 50 x 50-µm^2 to 1.5 x 7.5 µm^2 and a common ground electrode junction. The goal was to fabricate TMR junctions which show same TMR effect amplitude independent of the size of the junctions.

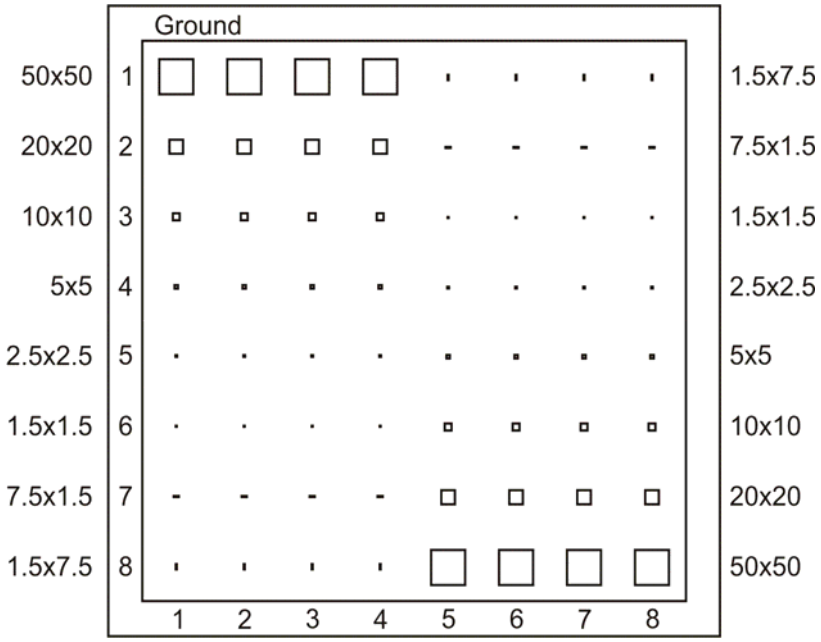

Fig. 21: Mask layout with TMR structures of various sizes (µm) used to fabricate thick and thin film FeGa based magnetostrictive TMR junctions.

The masks used for Exchange bias based TMR junctions are shown in Fig. 22a, Fig. 22b, Fig. 22c and Fig. 22d. Fig. 22a is the mask structure used for the fabrication of the bottom electrodes. Fig. 22b shows 8 TMR structures and 2 ground electrodes. In this mask structure the first four show similar junction size (e.g. 50x50 μm^2) and the second four TMR structures have same dimensions structures (e.g. 20x20 μm^2).

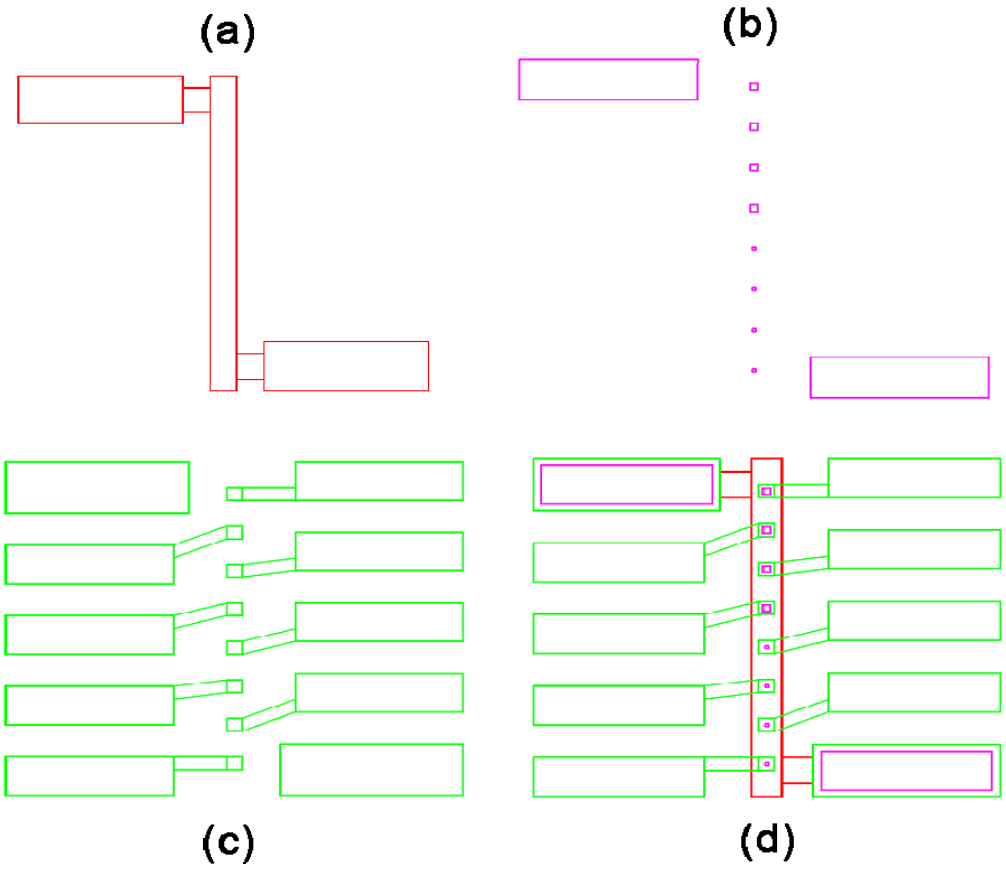

Fig. 22: (a) Bottom electrode mask, (b) TMR structures mask, (c) Top electrode contact pads mask and (d) Developed structures on wafer of exchange bias based TMR junctions

A four inch mask was used for this work with the possibility to fabricate the following structures 50x50 μm^2, 20x20 μm^2, 10x10 μm^2, 5x5μm^2, 2.5x2.5-μm^2 and 1.5x7.5 μm^2 on a wafer. Fig. 22c is the structure of the mask used for the contact pads of all exchange bias based TMR junctions and the ground electrodes. It facilitates contact of TMR structures using precision needles without damaging the actual TMR junctions to be measured during magnetoresistance measurements and strain measurements. The setup of these measurements will be discussed in the characterization section 3.3.4. Fig. 22d is an overlay of all mask patterns indicating the completely

fabricated structure of TMR junctions. Various photoresists and the UV dose utilized for different TMR stacks can be looked up in Table 2 and Table 3 respectively.

Thick and thin film FeGa electrode based magnetostrictive TMR Junctions	
Process	Parameters
Priming and Spin Coating	HMDS, 100°C and 1 minute. AZ6612 positive resist, 4000 rotations per minute (rpm), 1.2 μm photoresist
Soft bake	110°C and 1 minute
UV-Exposure	Dose: 40 mJ / cm^2 Exposure :1.2 seconds
Developer	AZ 726 for 1 minute followed by a deionised water dip
Hard Bake	120°C for 1 minute

Table 2: Process parameters for the fabrication of thick and thin film FeGa electrode based magnetostrictive TMR junction.

Exchange bias based TMR junctions	
Process	Parameters
Priming and Spin Coating	HMDS, 100°C and 1 minute. AZ 5214E image reversal resist, 4000 rotations per minute (rpm), 1.40 μm photoresist
Soft bake	110°C and 50 seconds
UV-Exposure	Dose: 59 mJ / cm^2 Exposure : 2.2 seconds
Image Reversal	120°C, 2 minutes in hotplate
Flood Exposure	Dose > 200 mJ / cm^2
Developer	AZ 726 for 1 minute followed by a de-ionised water dip
Hard bake	120°C for 50 seconds

Table 3: Process parameters for the fabrication of TMR junctions and contact pads

Following were the types of photoresist used during this work:

1. AZ 6612, Positive photoresist where the polymer resist dissolves at the places of exposure of UV- light (Fig. 23). A vertical profile as shown below can be achieved when the exposure dose of UV- light is moderate and when the sample is quenched in the developer.

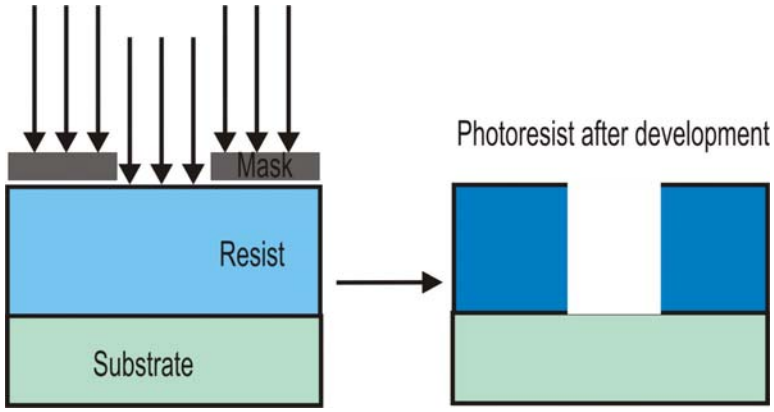

Fig. 23: Exposure and development of positive photoresist

2. AZ 5214 E, Image reversal photoresist which is capable of image reversal. This photoresist is positive resist in combination with a cross-linking polymer which results in a negative resist profile. Few advantages of using image reversal resist are that one can use a dark field mask and a positive resist. After developing the resist side walls shows an undercut. This undercut can prevent the resist sidewalls coated by the film during the deposition. Thus the use of an image reversal photoresist facilitates easy removal of the resist during the lift-off. Positive resists have high contrast, high aspect ratio and good step coverage. Image reversal is achieved by combining photosensitive compound with special cross-linking polymer which cross-links above 110°C, at the exposed areas. Because of the cross-link the exposed area is almost insoluble and not light sensitive. Whereas the resist in unexposed area behaves like a normal positive photoresist. A flood exposure makes the unexposed area soluble in developer. As a result a negative image of the mask is achieved. The mechanism of image reversal is shown in Fig. 24.

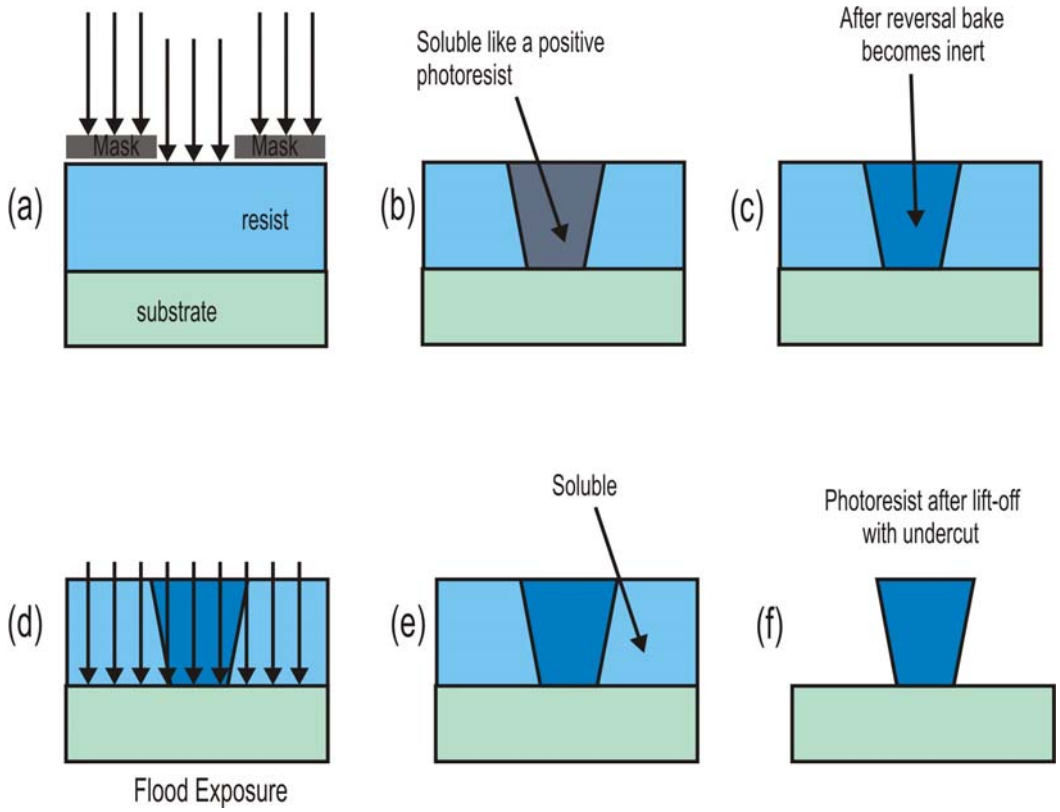

Fig. 24: Image reversal photoresist mechanism[72,73]

3.1.5 Ion beam etching (IBE)

Release etching of free standing TMR junctions was done by ion beam etching (IBE). An IonFab 300-plus from Oxford Instruments was used for this purpose. A 1000 W RF power supply with 13.56 MHz oscillator frequency was used, the diameter of the ion source is 35 cm. A 350 mA ion-beam current was applied and the beam voltage was maintained at 400V. Argon is used as the feed gas and 15 sccm flow was maintained during the process. The base pressure was maintained at lower 10^{-6} mbar and during the process an argon pressure of $1.9*10^{-4}$ mbar was maintained. The pressure during the etch process is given by the turbo molecular pumping system and the argon flow. A neutralizer supplies electrons into the argon ion beam to avoid the charging up of insulating samples during etching. Thus insulators can also be etched by IBE. During IBE etch process both photoresist and the thin film are etched away. The photoresist is much thicker and etch rate of the photoresist chosen is usually less than the film to be etched thereby protecting the thin film under the resist. The argon ions hit the sample at a

30° angle (Fig. 25). The surface coated with the photoresist remains protected during ion beam etching process, whereas the surface not covered by the photoresist is etched away. The sample holder is tilted to 30° and rotated at a constant speed 10 rpm during the etching process to establish uniform and better etch profile over the sample and to mitigate re-deposition effects such as shorting of the tunnel barrier at the structure edges.

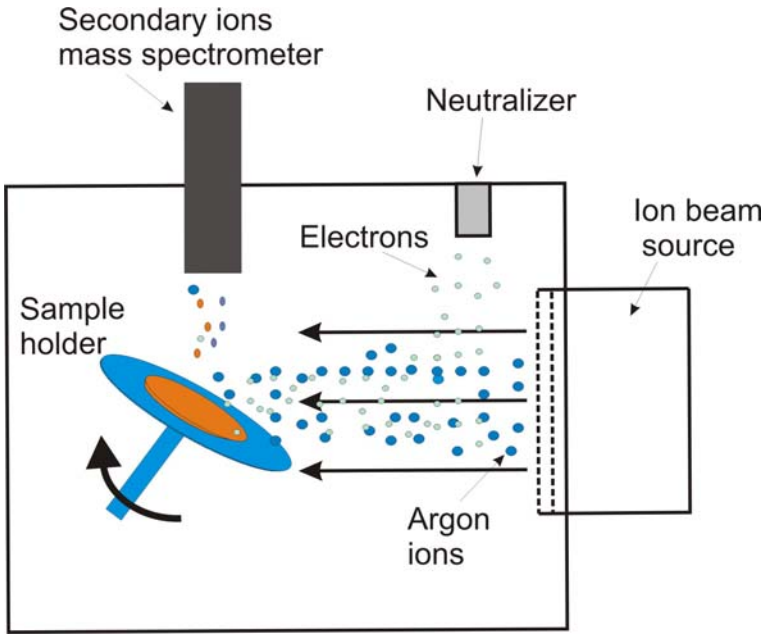

Fig. 25: Schematic set-up of ion beam etcher IonFab 300-plus

Ion beam etching is the key step to structure TMR stacks. The stack is etched from the top electrodes until the end of the barrier layer. A secondary ion mass spectroscopy (SIMS) detects the intensity of secondary ions formed by the bombardment of the sample surface by primary argon ions. SIMS is one of the standard end point detection tool used for etch stop of TMR stacks. Usually the etch of TMR junctions is stopped after completely etching through the barrier layer. IBE etch of TMR junction leaves free standing TMR structures with etch gaps. These etch gaps should be covered with passivation layer (SiO_2) to avoid any conducting lines between the junctions.

3.1.6 Insulating layer deposition and lift-off

After IBE etching, the sample was put immediately inside Ardenne CS730 S sputter depositing cluster tool. SiO_2 was sputter deposited by reactive sputtering of Silicon with 6 sccm O_2 and 14 sccm Ar. The pressure in the chamber during deposition was maintained at $4*10^{-3}$ mbar. About 100 to 150 nm of SiO_2 was deposited on the TMR stacks, such that the deposited SiO_2 was thicker than the stack. This serves as an insulating layer between the structures of different sizes. Fig. 26a is a schematic showing the deposition of SiO_2 on the resist coated TMR stacks and into the gap created by the IBE etch.

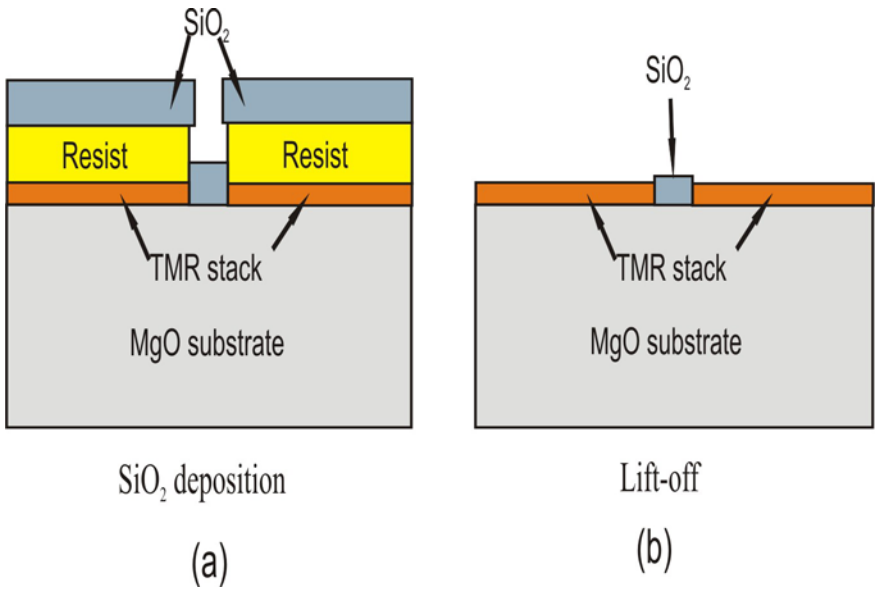

Fig. 26: (a) Deposition of SiO_2 on the TMR stacks with the photoresist protective layer, (b) The sample after lifting off the resist.

Lift-off is the process of removing the unwanted photoresist to produce free standing TMR stacks. After SiO_2 was deposited the sample was immersed in acetone and iso-propanol in an ultrasonic bath until the photoresist was removed shown in Fig. 26b. It was now important to perform another lithography to fabricate contact pads on top of the TMR structures. Fig. 22c is the mask used to fabricate contact pads for exchange bias based TMR junctions. The contact pads facilitate contact of high precision needles for magnetoresistance measurement.

3.2 Structural characterization techniques

3.2.1 Energy dispersive X-ray spectroscopy (EDX)

An Oxford instruments INCA 3.04 EDX detector constructed inside an FEI Helios Nanolab Dualbeam system, was used to analyze and determine the stoichiometry of iron gallium (FeGa) sputter deposited thin films. The reference target used for this work had the following composition: $Fe_{79}Ga_{21}$ atomic percent. Two different composition of sputter deposited FeGa thin films were used. FeGa sputter deposited at 200 W RF sputter power had a composition of 80.4 atomic percent Fe and 19.6 atomic percent Ga. A 20 W sputtered FeGa has the following composition 81.6 atomic percent Fe and 18.4 atomic percent Ga. The accuracy of the composition measurement can vary from ±0.5at % to ±1at %[74].

An analysis procedure called ZAF correction is widely used to correct the matrix effects in which correction for the atomic number effect (Z), absorption (A) and fluorescence (F) are calculated separately. To eliminate the influence of the matrix effects, reference measurements are performed on a standard and its relative X-ray intensities are used to fit for the final result. Advantage of this correction is that there is no need for matched standard, pure element standard is sufficient.

3.2.2 X-Ray diffraction (XRD)

A Seifert XRD 3003 with 4-circle goniometry was used for this work. A 40 kV and 40 mA power supply was used to bombard the copper anode to produce Copper K_α radiation. The generated X-rays are collimated and focused on the thin film surface. The difference in the travel path of x-rays after being reflected from thin film surface should be integer multiple of the wave length to have a constructive interference. This will happen if the angle of incidence of x-rays and the angle of reflection are the same. This can be explained on the basis of Bragg's law[75]:

$$n\lambda = 2d \sin\theta \qquad (18)$$

Where n= order of diffraction, λ= wavelength of X-ray, d= distance between lattice plane and θ= angle of diffraction. The phase and texture of FeGa thin films sputter deposited on different substrates and different sputter power were analysed by X-ray diffraction during this work. For this purpose θ-2θ scans were performed for the values of 2θ between 20-120. The depth of penetration of the X-rays depends on the type of the material and intensity of the incident X-ray. This is usually around a few μm to about 100 μm.

3.2.3 Transmission electron microscopy (TEM)

A Philips CM 30 microscope was used to determine the microstructure of the FeGa thin films and the TMR Junction. The samples were prepared by focussed ion beam (FIB) installed in Scanning electron microscope, FEI Helios and also by electro polishing. Ray diagram of a TEM can be seen in Fig. 27.

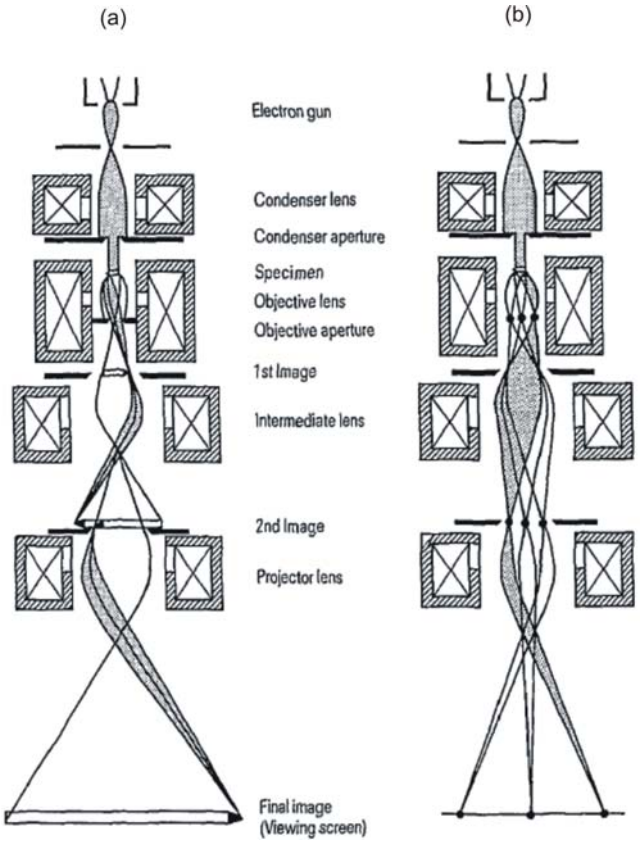

Fig. 27: Schematic layout and ray diagrams of a transmission electron microscope. (a) Ray diagram for bright field imaging: the aperture angle of the bundle of rays leaving each object point is limited to approx. 1 mrad by the objective aperture, and (b) ray diagram for selected area of diffraction (SAD)[76].

High energy electrons (300 keV) from the electron gun irradiate the sample of thickness 200nm or less. The shape of the electron beam from the electron gun is controlled by condenser lens and condenser aperture. The electrons are transmitted through the sample and the objective lens receives these electrons. The first image of the specimen is formed after the objective lens. This image is magnified by means of intermediate lens and projector lens. There are two basic modes of imaging in Transmission electron microscopy. The diffraction mode, where the electrons diffracted from the sample are imaged on the viewing screen and image mode, where the image of the specimen is projected on illuminated screen. Basically there are two important types of imaging modes:

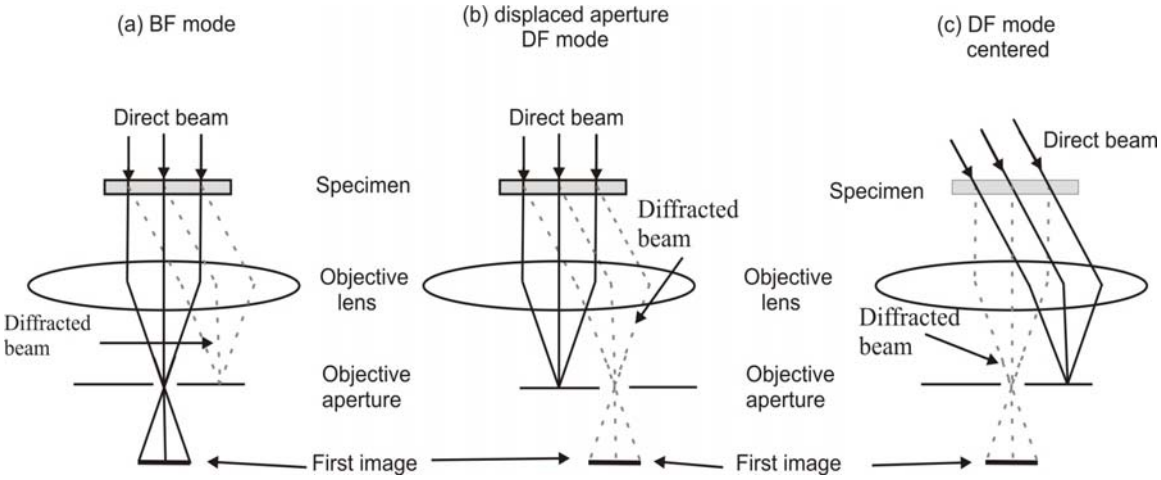

Fig. 28: Imaging modes: (a) bright field (BF) mode, (b) dark field(DF) mode (displaced aperture) and (c) dark field (DF) mode (centered) [77]

The bright field (BF) imaging mode, an aperture is placed to the center of the optical axis. The electrons scattered larger than a certain angle will not contribute to the image and only the electrons passing through the center of the aperture will be displayed (Fig. 28a). The dark field (DF) shown in Fig. 28b is another mode imaging where the aperture is displaced from the center and the image is generated by the intensity of diffracted beam or scattered electrons. But this method has a disadvantage that the DF image will move on the screen and it is difficult to focus because the off axis electrons suffer aberrations. In order to avoid the incident beam on the sample, the beam can be tilted so that the diffracted beam will travel through the centered aperture. This is also known as DF Mode centered as shown in Fig. 28c.

3.3 Magnetic characterization techniques

3.3.1 Vibrating sample magnetometry (VSM)

The fundamental properties of a magnetic material can be determined by magnetizing the material under external magnetic field. Hysteresis, permeability, magnetic anisotropy field and Curie temperature of the magnetic materials can be measured by magnetizing the sample material in an external magnetic field. In this work the VSM measurements were performed using a Lake Shore 7300 magnetometer.

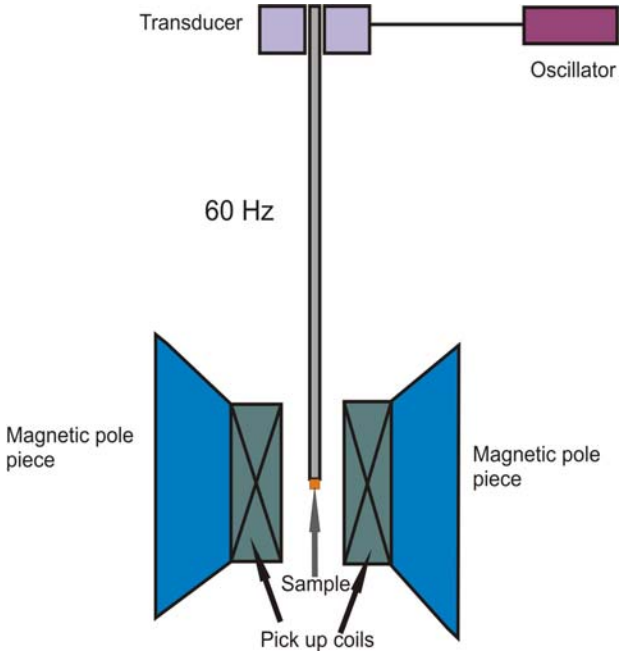

Fig.29: Schematic of Vibrating Sample Magnetometry (VSM)[78]

Fig.29 shows a schematic of VSM. The operating principle of VSM is based on Faraday's law. According to his law an electromagnetic force is generated in the coil when there is a change in the flux lines linking the pickup coils[78].The sample was magnetized by electromagnets which can generate highly uniform magnetic fields in the x-axis. The pole pieces can generate field resolution as small as 1 μT. Maximum field strength of 2.1 Tesla can be generated by the pole pieces. The measurement setup can detect magnetic moments as low as nAm^2 (μemu).

Pickup coils were fixed on the electromagnets to measure the change of flux. The VSM was calibrated every time before doing a measurement. A spherical Ni standard was used for this purpose. After this the sample was clamped to the sample holder and adjusted to lay at the center of the pickup coils. A sinusoidal signal produced by the oscillator can be changed into vertical vibration by means of a transducer (see Fig.29). The sample and the sample holder connected to the transducer, which vibrates at a frequency of 60 Hz and amplitude of 1mm. The result is change in the magnetic moment of the sample thereby inducing voltage in the pickup coils. The induced voltage is proportional to the magnetic moment of the sample, the frequency and amplitude of the vibration, and the distance to the pickup coils. The frequency and the amplitude of the vibration can be separated by using a lock-in amplifier. The distance to the pickup coils can be adjusted by proper calibration before the measurement. The error in the measurements arise due to the difference in the shape of the sample in comparison with Ni standard and in determination of the volume of sample to calculate magnetization. The range of the error can therefore be about 5%[79,82].

3.3.2 Magneto-optic Kerr effect (MOKE)

A Nano MOKE2 microscope from Durham Magneto optics was used to perform MOKE measurements. MOKE is used to study the magnetic properties of materials like the magnetic domain pattern evolving during magnetization reversal and magnetic hysteresis. Metallic and light absorbing magnetic materials which have a smooth surface can be studied by Kerr effect[80]. When a polarized light falls on the surface of the sample it will be reflected with small rotation of the polarization plane.

During this work longitudinal Kerr effect was used to study the properties of thin films. Fig. 30 shows the electrical polarization (E), V_L the direction of Lorentz force and K the Kerr vector. In this case the magnetization is oriented parallel to the surface. A linearly polarized light will induce electrons to oscillate parallel to its plane of polarization. This is the plane of electric field E of the light. Majority of the light is reflected regularly and do not change its polarization plane, this component is called R. The Lorentz force (V_{Lor}) acting on the sample induces a small component of vibrational motion perpendicular to the primary motion and to the direction of the magnetization. This motion is proportional to V_{Lor}=-mxE. Because of Huygen´s principle this motion leads to secondary amplitude K, the Kerr

amplitude for reflection. The superposition of regular reflection R with the kerr reflection K leads to magnetization-dependent polarization rotation.

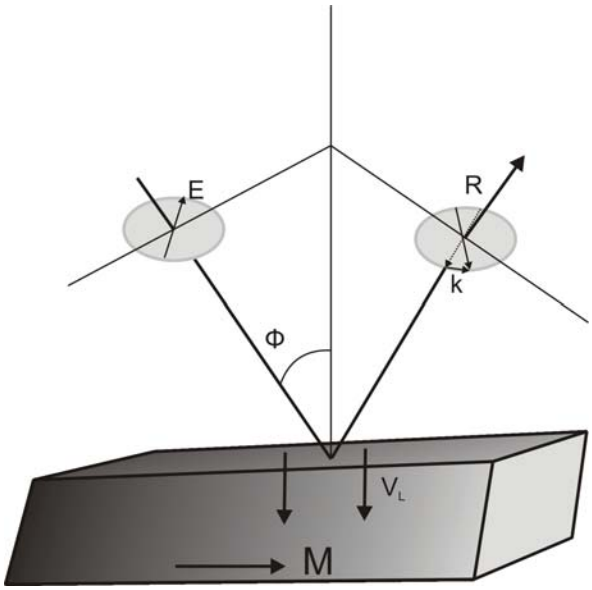

Fig. 30: Longitudinal Kerr effect for polarization perpendicular to the plane of incidence.

The setup of MOKE is shown in Fig. 31. The laser light of wave length 630 to 640 nm enters the system setup. A laser collimator collimates the beam to 10 mm diameter. The beam passes through beam splitting cube which mixes white light into the beam path. Laser and white light are then focused onto the sample by means of an objective lens.

The sample is mounted on a sample stick and is placed between the poles of the electromagnet. The mounted sample is capable of x, y and rotational movement. The sample can be moved in 500µm, 10µm and 1µm steps to allow the user to focus the laser light at particular spot on the sample. The electromagnets are capable of producing up to maximum 22 mT cyclic field. The light reflected from the sample passes through the receiving lens and then to the beam splitter. The beam splitter again mixes white light, a part of which is sent to the microscope CCD camera and the rest of the beam reaches the longitudinal kerr detector. A polarization analysis was performed on the received laser light to access the longitudinal kerr effect. For the measurement of magnetic hysteresis characteristics and strain sensitivity a specially designed three point sample holder was used. The sample holder allows equal amount of stress to be applied uniformly on the sample surface.

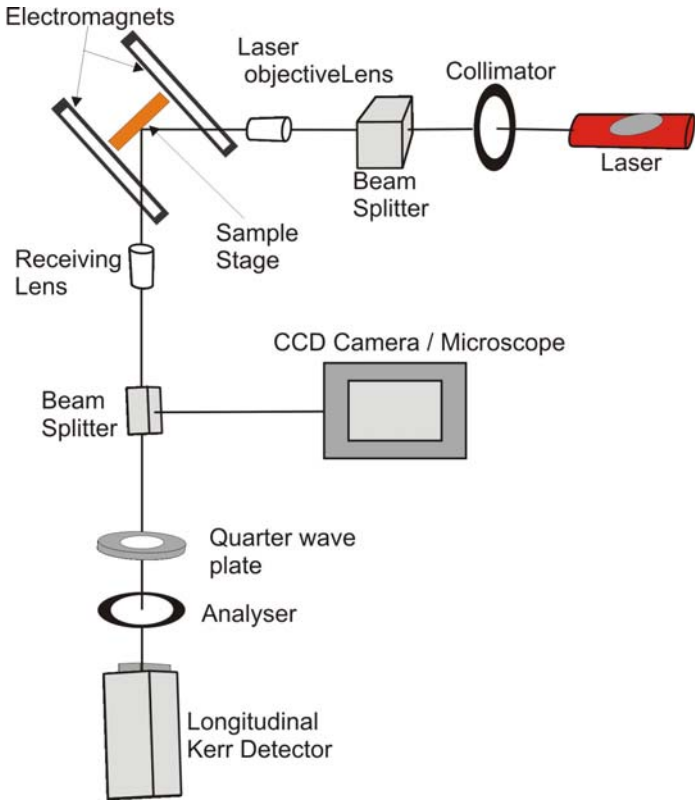

Fig. 31: Schematic diagram of the MOKE measurement set up

3.3.3 Magnetostriction measurement

Characterization of anisotropic magnetostriction of the sputter deposited FeGa thin films was perfomed by thin film cantilever deflection[81] based magnetostriction measurement setup shown in Fig. 32. To maximize the bending effect, the shape of the substrates was chosen to be cantilever shaped with the following dimensions: 2 mm width, 20 mm length and 0.25 mm thickness. The thickness of the substrate should be small compared to the length of the beam to minimize the bending due to the substrate and increase the bending effect due to the deposited thin film. FeGa thin film to be characterized were sputter deposited on MgO (100) oriented single crystal cantilever substrate. One end of the cantilever is clamped to the sample holder and other end is free.

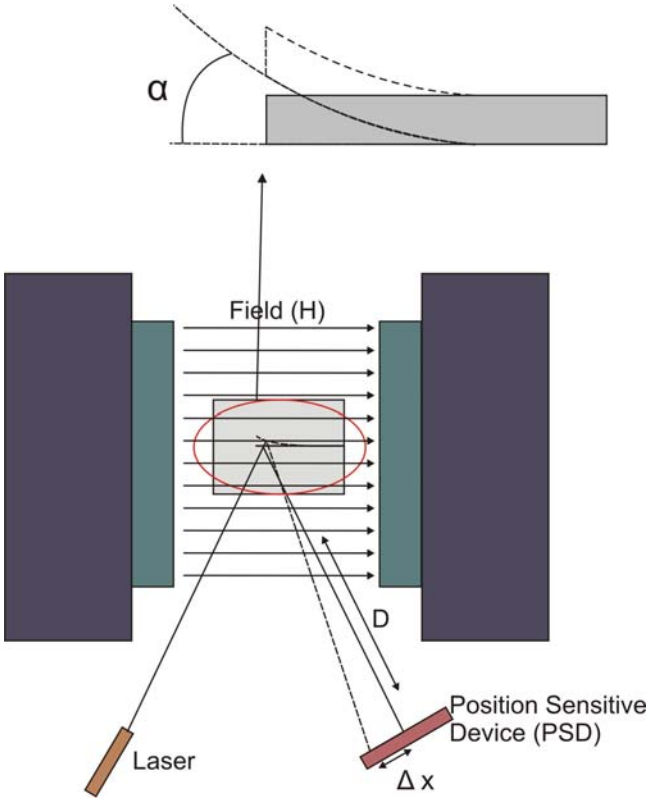

Fig. 32: Schematic representation of magnetostriction setup. Deflection of the cantilever coated with the magnetostrictive material in magnetic field is measured by a change in the deflection of the laser beam at the tip of the cantilever detected by the PSD as the change in the voltage.

Laser is focused on the tip of the free end of the cantilever and it is reflected. The reflection is adjusted to hit on the center of a position sensitive device (PSD). A PSD is a light sensitive element with a surface area of 100 mm^2. On applying an external magnetic field the free end of the cantilever bends due to the anisotropic magnetostriction of the magnetostrictive thin film samples. This will result in a change in the position of the laser reflection at the tip of the sample which is measured by the PSD and converted into voltage. The bending behavior of thin film is determined by factors such as thickness of the substrate and the thickness of the thin film, t_s and t_f, the young's moduli of the film E_f and the substrate E_s and also the corresponding Poisson's ratio υ_s and υ_f.

The displacement of the laser can be measured from the bending angle α (in Fig. 32) because of the magnetization of magnetostrictive thin film on cantilever substrate.

Since the bending of the cantilever is very small, we can calculate the bending as[82]:

$$\tan\alpha \approx \alpha = \frac{\Delta x}{2D} \tag{19}$$

The displacement on the PSD is Δx and D is the distance between the sample and the PSD. From the value α, we can calculate b, the magnetoelastic coupling factor of the thin film by the following formula[83]:

$$b = -\frac{\alpha t_s E_s}{l_s t_f 6(1+\upsilon_s)} \tag{20}$$

The value of b is measured in mega Pascal (MPa). l_s is the length of the free standing cantilever substrate. From b we can now calculate magnetostriction constant λ as shown below[84]:

$$\lambda = -b\frac{(1+\upsilon_f)}{E_f} \tag{21}$$

The saturation magnetostriction constant, λ_s can be derived by measuring the magnetostriction constants in parallel ($\lambda_{\parallel/s}$) and perpendicular direction ($\lambda_{\perp/s}$) as[85]:

$$\lambda_s = \frac{2}{3}(\lambda_{\parallel/s} - \lambda_{\perp/s}) \tag{22}$$

3.3.4 Magnetoresistance (MR) and strain measurement

Fig. 33 shows the schematic setup for measuring magnetoresistance. MR measurements were performed by placing the samples between the pole pieces of an electromagnet. The electromagnet is capable of supplying a maximum field of 1.5 Tesla. The patterned TMR junctions were contacted by two gold-plated beryllium copper precision needles. A Keithley 2400 source meter supplies constant voltage (10 mV was used during this work) to the needles and measures the current, at the two points of contact. To record the magnetoresistance a cyclic magnetic field is swept between the pole pieces and simultaneously the current is measured and recorded. The

field was increased and decreased in steps of 3 mT/s. The control of the magnet and measurements are performed by a computer program called "Test point". The program plots change in the resistance as a function of the applied field. From these measurements the TMR ratio were calculated using equation (1.1).

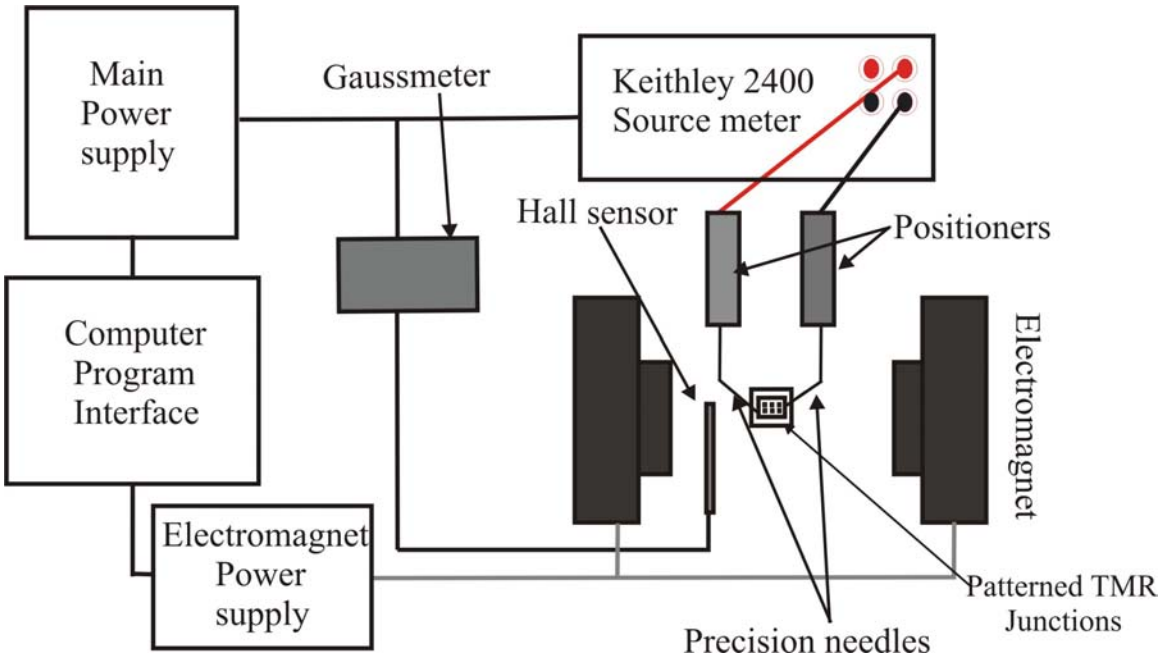

Fig. 33: A schematic of the TMR measurement setup showing the electromagnets and the precision needles used to contact the TMR junction. The positioners help for the movement of the precision needles to the exact location and contact the TMR junctions

In order to perform strain measurements the TMR junctions were fabricated on cantilever shaped substrates. This is achieved by using the masks shown in Fig. 22a, Fig. 22b and Fig. 22c. After lithography, the wafer is diced into cantilevers of dimensions 3 mm x 23 mm. Shown in the Fig. 34 is the schematic of 50 µm x 50 µm and 20 µm x 20 µm tunnel junctions patterned on a cantilever substrate. In Fig. 34 the first and the last contact pads represent the ground electrodes. First four contact pads after the ground electrode have same dimension (in case of Fig. 34 it is 50 µm x 50µm) and the next four contact pads represent 20 µm x 20 µm TMR junctions. Other TMR junction sizes fabricated using the above mentioned masks are 10 µm x 10 µm, 5 µm x 5 µm, 2.5 µm x 2.5 µm, 1.5 µm x 7.5 µm and 7.5 µm x 1.5 µm respectively.

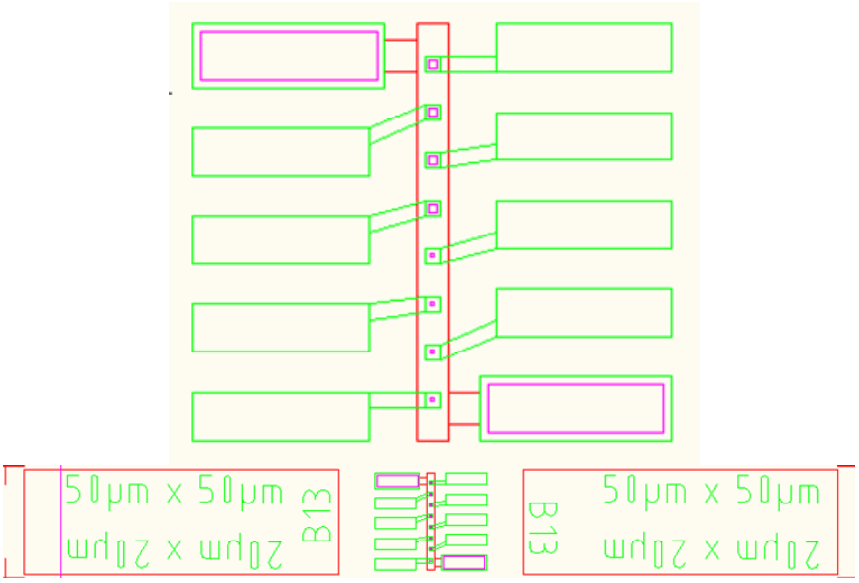

Fig. 34: Schematic of exchange bias based TMR junctions on a cantilever substrate used for the strain measurement. The first and the last junctions correspond to the ground electrode 1 and ground electrode 2 respectively.

The strain measurements of the TMR junctions were performed using a bending apparatus (the schematic-setup is shown in Fig. 35a). It allows measurement of the resistance by applying cyclic magnetic field simultaneously capable of straining the sample homogeneously in parts per thousand range. The cantilever sample with TMR junction is placed between the four points of contact. The sample is strained by the displacement of the pusher block. A motion controller connected to the linear actuator controls the forward and backward movement of the pusher block. The forward or backward movement of the linear actuator exerts compressive stress or tensile stress to the sample. The pusher block can be moved as small as 1 µm per step. During the measurement the actuator was moved in 20 µm displacement steps. Selected junctions were wire bonded to the sample holder to establish electrical connectivity. Through Keithley source meter a constant bias voltage (10 mV) was applied to the junctions at different applied stress conditions and the corresponding tunnel resistance was simultaneously recorded. The distance between the outer most points of contact is 18 mm. The strain calculated for a 20 µm displacement was 0.11‰.

(a)

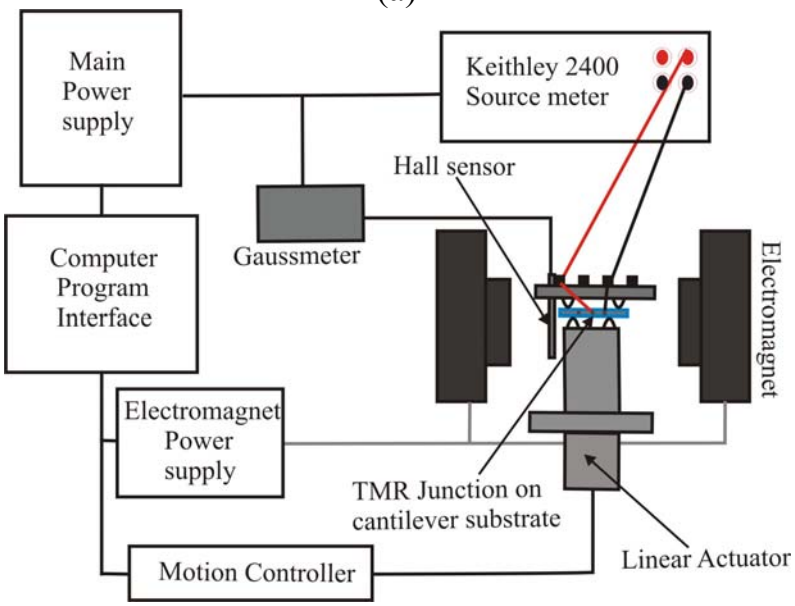

(b)

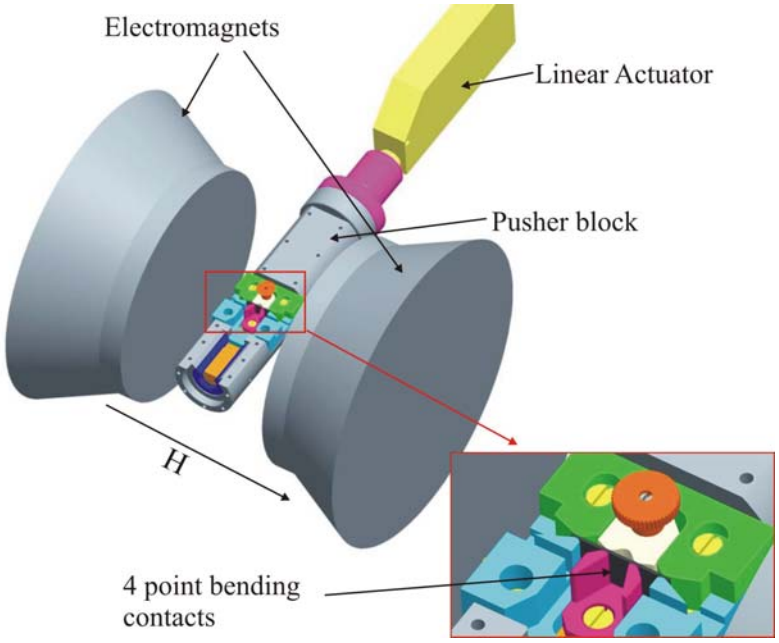

Fig. 35: (a) Schematic of strain measurement setup using four point bending device and (b) Linear actuator strain gauge and wire bonded sample placed between the four point bending device for supplying stress or strain

4 Results and discussion

4.1 Fabrication and characterization of FeGa thin films

4.1.1 Characterization of the sputter deposited FeGa thin films and composition determination by EDX

FeGa thin films were prepared during this work in a CS 730S cluster deposition tool using a RF magnetron power source. The composition of the FeGa target was determined by EDX as 79:21 at % (Fe:Ga). The deposition rate and homogeneity were analyzed for the sputter deposited FeGa thin films as a function of with and without magnetic forming field. The homogeneity of deposition with and without magnetic forming field was analyzed first. For this purpose nine silicon pieces (5 mm x 5 mm) coated with photoresist (2 mm width) at the center were placed at nine points equally distributed on a wafer sized substrate holder.

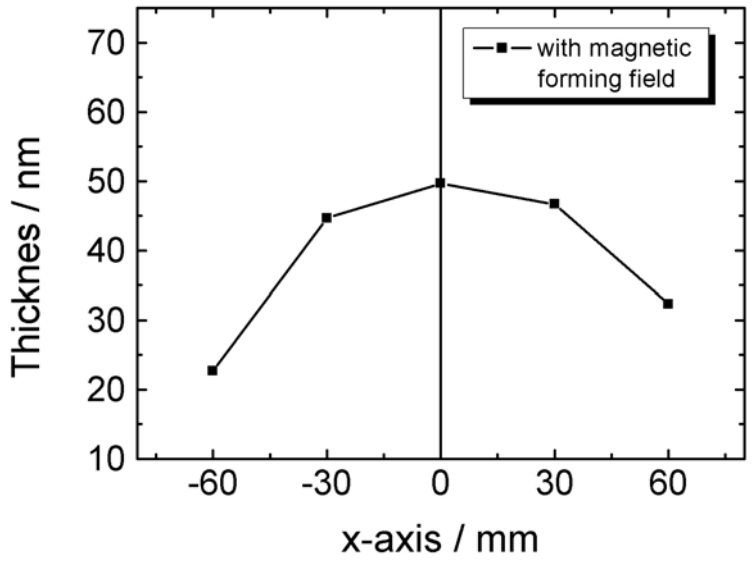

Fig. 36: Distribution of the sputter thickness of FeGa on the substrate holder plate. The sample was sputtered at 20 W, $4*10^{-3}$ mbar argon pressure, sputter deposition time of 2 hours and magnetic field was applied during deposition.

After sputter deposition the photoresist was removed by the lift-off procedure described in the experimental section 3.1.6. The thickness of FeGa at equally distributed points on the substrate holder were measured. During the sputter deposition parameters like sputter power, time of deposition and argon pressure were maintained constant for deposition with and without magnetic field.

Fig. 36 is a plot showing the homogeneity of FeGa film thickness distribution at different positions on the substrate holder. X axis denotes position of the measurement points in the substrate holder. The Y axis shows the thickness distribution of FeGa film after two hours of sputter deposition. A 20 mT constant magnetic forming field was applied to the samples perpendicular to the x-axis during sputter deposition. From the Fig. 36 an inverted parabolic distribution of the thickness can be observed. The film thickness was maximum in the middle of the substrate holder and gradually decreases towards the edges. The first zone extends to a radius of 30 mm and the thickness of FeGa in this zone was in the range of 45-50 nm. The second zone corresponds to thickness varying between 25-45 nm.

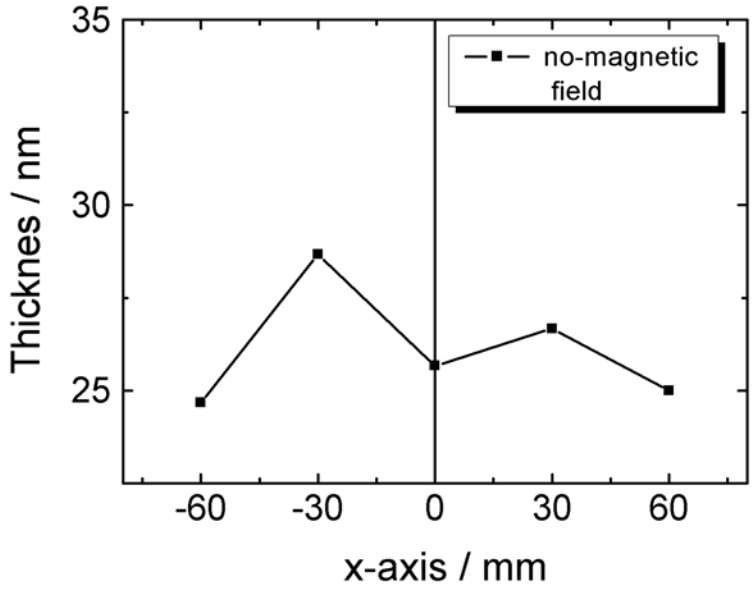

Fig. 37 : Distribution of the sputter thickness of FeGa on the sputter plate. The sample was sputtered at 20 W, $4*10^{-3}$ mbar argon pressure sputter deposition time of 2 hours and no magnetic field was applied during deposition

Fig. 37 shows the plot for FeGa thin films sputter deposited with the same parameters as shown in Fig. 36, but no magnetic forming field was supplied

during sputter deposition. Therefore no additional magnetic field was supplied to the films except the magnetic field from the magnetron during the sputter deposition. The sputter deposition thickness varies between 25-29 nm. No clear dependency of the film thickness with the position of the sample holder was observed. Further it can be observed that FeGa thin films sputtered with magnetic field show a higher deposition rate as compared to the film sputter deposited without magnetic field.

Secondly, the deposition rate of the sputter deposited FeGa thin films as a function of with and without magnetic forming field at various sputter powers was analyzed. The samples were sputtered at an argon pressure of $4*10^{-3}$ mbar and 30 minutes sputter time was maintained for all the sputter powers. FeGa thin film sputter deposited with forming field indicate an increase in the sputter deposition thickness as compared to the film deposited without magnetic forming field. An investigation performed to determine the above mentioned effect at different sputter powers can be seen in Fig. 38.

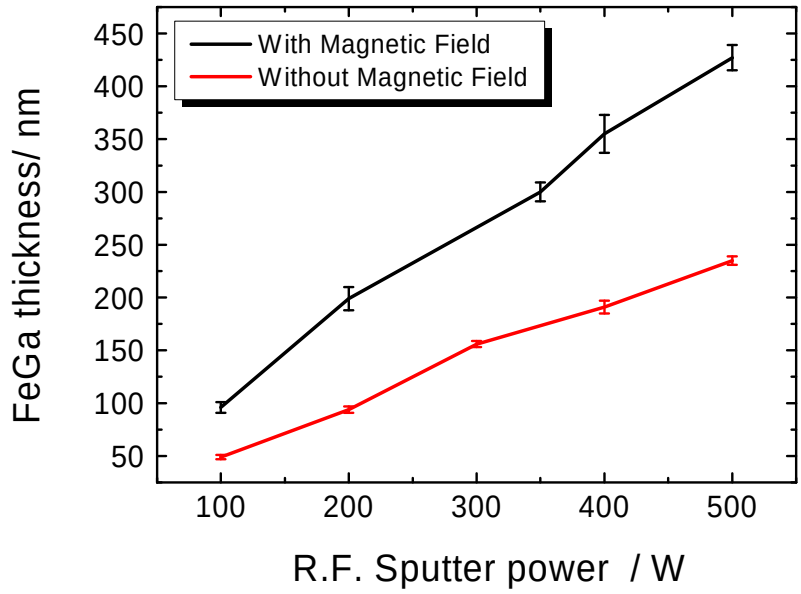

Fig. 38: Thickness of FeGa films sputtered at different sputter power with magnetic field and without magnetic field are shown. All films were sputter deposited for 30 minutes at $4*10^{-3}$ mbar argon pressure and 20 sccm Ar flow.

It can be inferred that at all sputter powers the FeGa deposition with forming field show always a higher deposition thickness as compared to the samples sputtered without magnetic field. The sputter deposited FeGa released from the target was trapped by the additional forming field near the substrate

holder. This trapping results in an additional increase in the sputter deposition rate. A linear increase in the sputter rate is expected with increase in the sputter power and the same can also be observed from the Fig. 38. The error bars corresponds to the standard deviation calculated from the measured mean thickness values. Also the sputter rate increases with increasing sputter power. This is because at high sputter power ionization of argon ions are enhanced, therefore more ions bombard the target resulting in higher sputter deposition rate. As discussed earlier, Wang et al[86] showed FeGa films deposited with forming field show an increased magnetostriction as compared to films deposited without magnetic forming field. Therefore a forming field was supplied during the sputter deposition of FeGa thin films during this work.

The magnetostriction of FeGa is maximum at 19 at % of Ga as shown by Clark at al[87]. So the sputter deposited FeGa thin films with magnetic forming field were characterized by EDX spectroscopy for composition analysis. The sputter power was varied from 20 W to 500 W. The argon pressure and the thickness were maintained constant for all sputter powers. As mentioned earlier the composition of the sputter target was 79:21 at % (Fe:Ga). The variation of Ga as a function of the sputter power is shown in Table 4.

Sputter power	Ga at %
20	18.4 ± 0.52
50	17.3 ± 0.55
100	17.2 ± 0.54
150	16.9 ± 0.54
200	17.6 ± 0.51
250	18.6 ± 0.52
350	19.4 ± 0.65
400	17.4 ± 0.51
450	16.9 ± 0.52
500	10.3 ± 0.50

Table 4: Atomic percentage of gallium at different sputter power. The pressure was maintained at $4*10^{-3}$ mbar and 20 sccm argon flow in the sputter chamber. The thickness of the samples were approximately 400nm

At 20 W sputter power the Ga at % was 18.4±0.52 %. A small reduction of Ga (2 at %) was observed for an increase in the sputter power until 150 W. Further increase in the sputter power however shows an increase of Ga %

until 350 W. At 350 W the Ga atomic percent was measured as 19.4±0.65 %. When the sputter power was increased further (400 W and 450 W) there is a reduction (17.4 ± 0.51 at % and 16.9 ± 0.52 at %) in the Ga %. At higher sputter power (500 W) there is a drastic reduction in the Ga % (10.3±0.5 at %). As shown by Clark et al[87] the magnetostriction of FeGa from 17.5 to 19.5 at % Ga is on the increasing slope of the first magnetostriction peak. Therefore on the basis of the composition FeGa thin films sputter deposited from 20 W to 400 W can be used to fabricate highly magnetostrictive films.

From literature[88,89,90] it was shown that annealing of as sputtered TMR junctions as high as 500 °C show a very big increase in the TMR ratio. To be used as a sensing layer in the TMR junctions FeGa thin film requires that the Ga composition does not vary at annealing temperatures as high as 500 °C. Table 5 shows the effect of high annealing temperatures on the gallium percentage of the FeGa films. A 400 W sputter power was chosen because of the high sputter deposition rate. The deposited FeGa thin films were annealed at different temperatures for 1 hour in a rapid thermal annealing apparatus and the composition of the as prepared (as deposited) and annealed samples were measured by EDX.

Temperature	Ga at % ± 0.5 %
As prepared	17.4
500°C	17.1
600°C	13.5
700°C	7.9

Table 5: Rapid thermal annealing of FeGa sputtered at 400 W and thickness 400 nm.

The FeGa film annealed at 500°C show a small reduction in gallium resulting in 17.1±0.5 at % Ga, which is at the bottom of the first magnetostriction peak shown by Clark et al[87]. With increasing annealing temperatures of 600°C and 700°C the Ga percent are reduced to 13.5 and 8 at%. This shows that annealing of FeGa thin films at very high temperatures to recrystallize would result in the reduction of magnetostriction. It can be inferred on the basis of composition that annealing below 500°C does not show a big reduction in the Ga content. Usually to establish exchange bias temperatures as high as 300°C is enough and this can be achieved without loss of the Ga content thus there would be no reduction in the magnetostriction.

4.1.2 Structural characterization by XRD

MgO (100) oriented single crystal substrates were used for the deposition of FeGa thin films as it was suggested by Butera et al[18] that the crystalline cell of FeGa should be rotated 45° to accommodate into MgO lattice, resulting in epitaxial growth in the (200) direction. Epitaxially grown TMR junctions show high TMR ratio[91]. For this thesis work it is therefore an advantage to epitaxially grow FeGa thin film on MgO substrates. The epitaxial growth can further proceed from the FeGa electrode to the MgO barrier in the TMR junctions resulting in high TMR ratio.

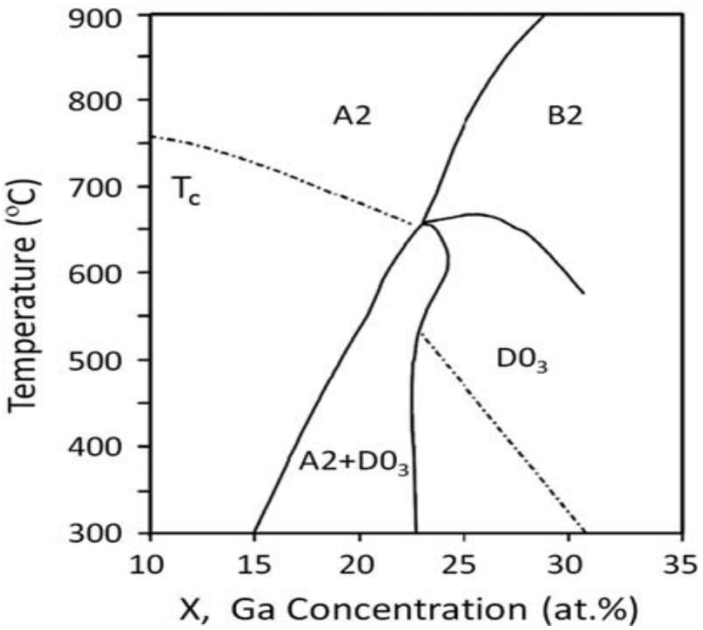

Fig. 39: Meta-stable phase diagram for Fe-Ga alloys[92].Solid lines describe solid-solid phase transformations between the A2, B2, and DO3 ordered alloy phases. The dash-dotted line indicates the ferromagnetic ordering Curie temperature.
[Taken from Du et al[93]]

To find out the phases of the sputtered film a meta-stable phase diagram of FeGa shown in Fig. 39 was used. The meta-stable phase diagram does not show the phases at room temperature. During the sputter deposition, highly energetic sputtered species are quenched on to the substrate[94]. Quenching is assumed to preserve the phases of FeGa observed at high temperatures. Therefore the meta-stable phase diagram of FeGa can be used for determining phases of the sputter deposited FeGa film. The FeGa sputtered at sputter powers 20 W- 350 W has 16.5-19.5 at % of Ga. The corresponding phase from the meta-stable phase diagram is $A2+DO_3$. From literature[95], the

DO_3 ordered body centered cubic (bcc) phase takes long time to stabilize and is achieved only by a very slow cooling rate. It states further that quenching of FeGa (~consisting of Ga 19 at %) results in disordered A2 bcc structure. Since sputter deposition process is similar to quenching, one can expect to suppress the DO_3 phase resulting in highly magnetostrictive A2 phase.

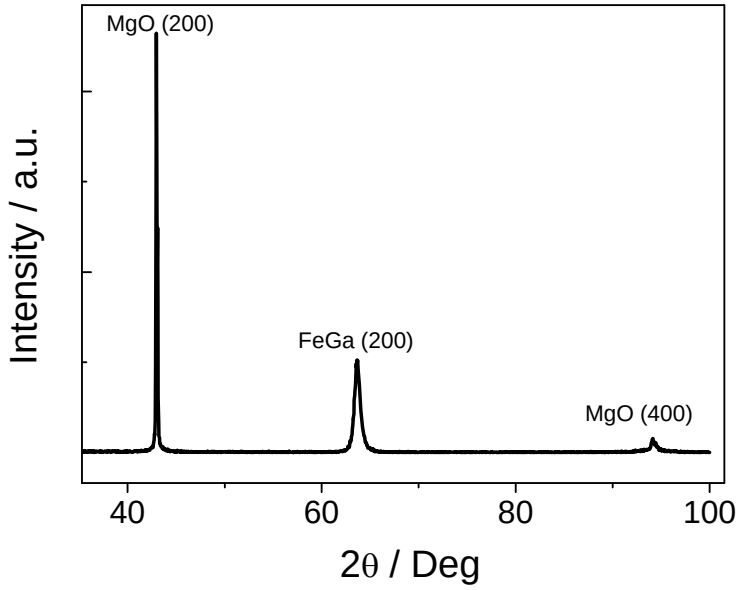

Fig. 40: XRD spectra of FeGa sputter deposited on MgO (100) substrate at 200 W, 20 sccm argon flow and $4*10^{-3}$ mbar argon pressure. The thickness of the FeGa film was 200 nm.

Fig. 40 shows X-ray diffraction intensities of FeGa sputter deposited on MgO single crystal substrate. A highly oriented growth of FeGa film in (200) crystallographic direction was observed. The (200) peak of FeGa at 2θ=64° as a function of the increasing sputter power is shown in Fig. 41. It can be observed that from 100 W to 200 W the peak position reduces to smaller 2θ values and after 200 W it remains constant. At 350 W sputter power an additional peak of FeGa can be observed at 2θ=56°. This is (210) peak of the $L1_2$ face centered cubic (fcc)[96] phase of FeGa film. High magnetostriction values were observed for the disordered bcc phase of FeGa[96]. Therefore to sputter deposit FeGa in TMR stacks sputter power below 300W was preferred.

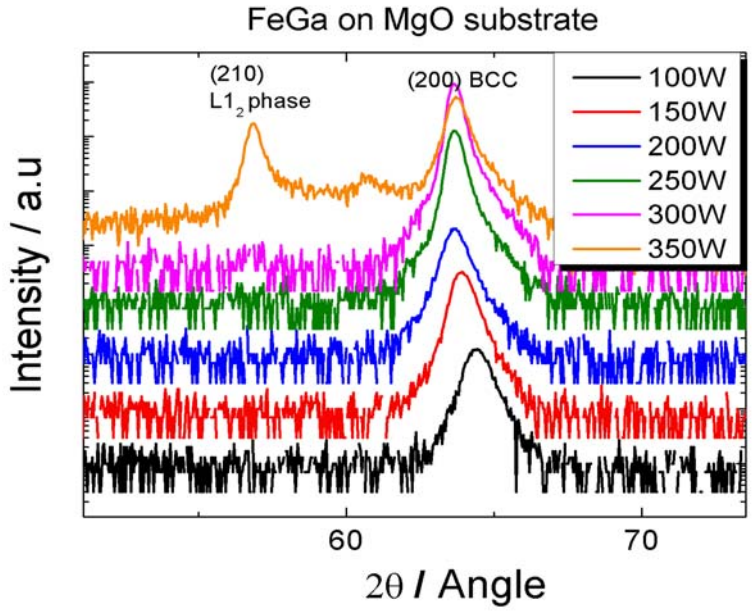

Fig. 41: X-ray diffraction pattern of as deposited FeGa thin film on MgO(100) substrate at different sputter power. The peak position at 2θ=64° denotes the (200) peak of FeGa and at 350 W the (210) $L1_2$ peak is observed.

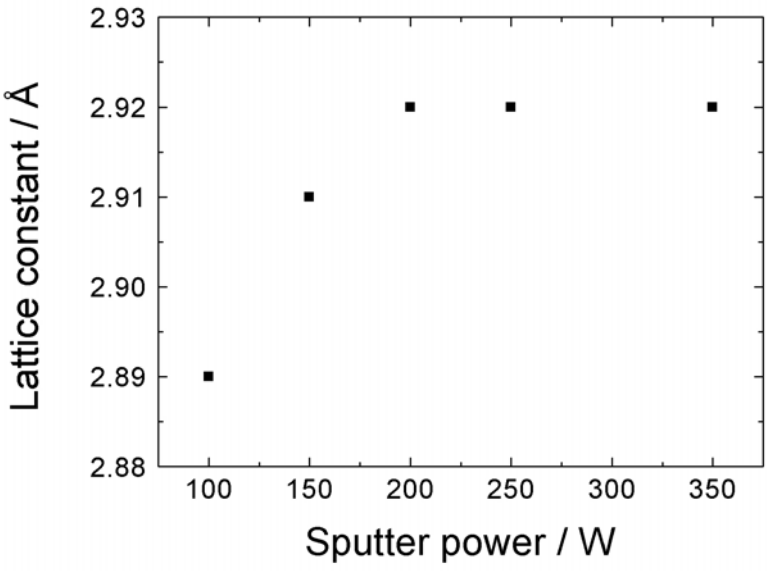

Fig. 42: Lattice constant of FeGa as a function of sputter power. The peak at 2θ=64° was used to calculate the lattice constant.

The lattice constant of the FeGa was calculated for the (200) bcc peak and is plotted against the sputter power as shown in Fig. 42. The lattice constant at

100 W sputter power is 2.89 Å. The lattice constant increases with the increase in sputter power because of the increase in the Ga content and reaches 2.92 Å at 200 W, thereafter it remains constant. It is known from the literature[97, 98] that the lattice constant of bulk FeGa showing a bcc phase is 2.92 Å. Since the lattice constant of the thin FeGa film reaches the energetically stable lattice constant of the bulk, as observed there would be no further increase in the lattice constant.

The position of MgO (200) peak at 2θ=42.9° closely overlaps the (110) peak of FeGa at 2θ=44.2°. To clearly distinguish these peak positions and other peaks a three dimensional area detector XRD measurement was performed at the caesar research institute, Bonn. Following thicknesses of FeGa thin films: 10 nm, 90 nm and 800 nm were analyzed. Fig. 43 (a) and (b) shows the intensities of a 90 nm FeGa film sputter deposited at 200 W and MgO substrate detected by the area detector. Point intensity in these figures mean that the film is highly oriented and the line intensity would represent polycrystallinity of the FeGa film.

Fig. 43 (c) and (d) are the spectra obtained by integrating the intensities of Fig. 43 (a) and (b). The intensities of a MgO substrate was measured earlier for comparison (not shown here). At 2θ=63.9° a point intensity of FeGa was observed (red dot in Fig. 43 (a) and (b)) whose intensity is smaller than the intensity of MgO substrate. This intensity corresponds to a highly oriented (200)[99, 100] crystallographic growth of the FeGa film. Similar measurements of a 10 nm FeGa film (not shown here) on MgO substrate resulted in a very weak reflection at 2θ=63.9° and the (200) peak was less oriented as compared to 90nm film. An 800 nm FeGa film showed line intensity corresponding to the polycrystalline (110) and (211) peaks at 2θ=44.2° and 81.5° in addition to highly oriented (200) peak (not shown here). An increase of the film thickness from 90 nm to 800 nm increases the polycrystallinity in FeGa thin films.

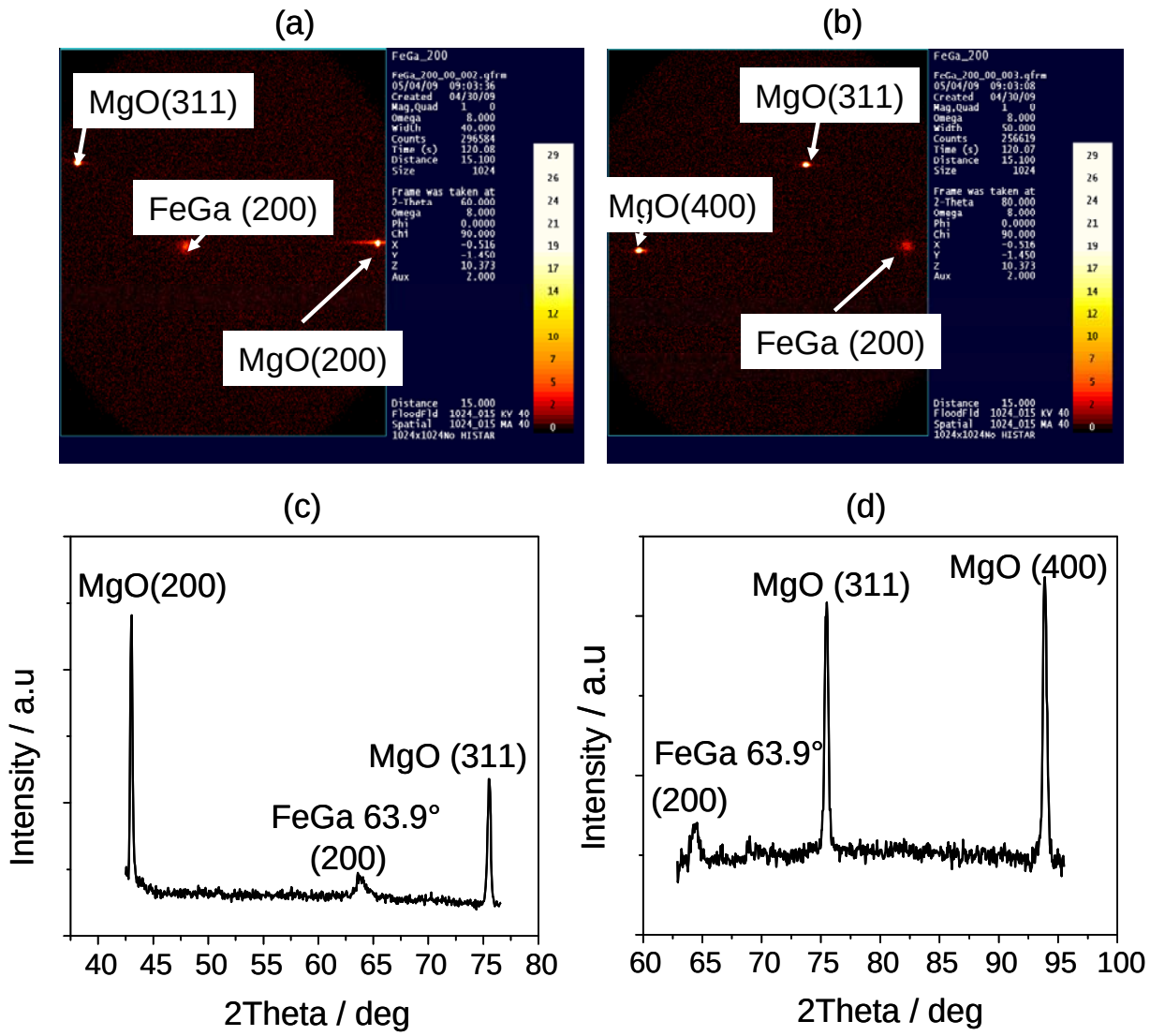

Fig. 43: XRD using a three dimensional area detector of 90 nm FeGa on MgO (100) substrate at 200 W, $4*10^{-3}$ mbar pressure and 30 minutes sputter time scanned using an area detector. The images (a), (b) are formed on the 3-D detector at various scan angles, (c) and (d) the spectra of MgO and FeGa obtained by integration of the intensities from the detector. PS: The direction of the scan for a and b and the spectra direction of c and d are not the same.

4.1.3 Magnetic characterization of FeGa thin films

The magnetic properties of FeGa thin films were characterized by MOKE and magnetostriction measurements. The strain sensitivity, the coercive field and the remanence of the as prepared FeGa thin films were characterized by a special three point sample holder using MOKE measurements. A 500 W

sputter power corresponding to low Ga content and 20 W sputter power showing an optimum Ga at % were analyzed. Shown in the Fig. 44 is a magnetic hysteresis measured for strained and unstrained state of a sample sputter deposited at 500 W. The thickness of the FeGa film was 800 nm. The film was deposited on a 2 mm x 20 mm MgO cantilever substrate.

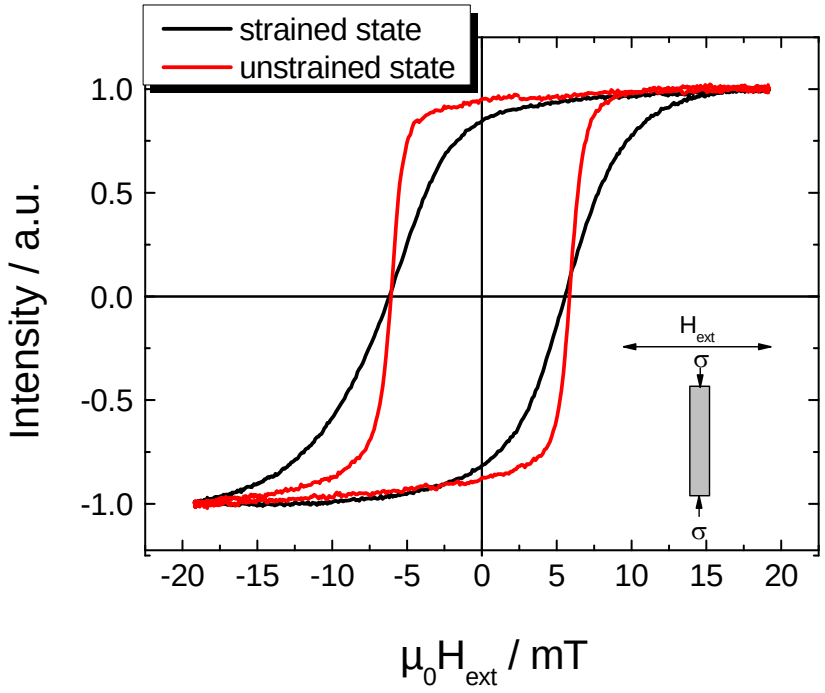

Fig. 44: MOKE Measurements of the magnetic hysteresis of an unstrained and strained FeGa thin film sputter deposited at 500 W and 800 nm film thickness and the sample perpendicular to field during measurement.

The position of the sample during the measurement with respect to the external magnetic field and the strain applied (compressive) are shown as an inset diagram in Fig. 44. A compressive strain was applied at right angle to the sample. The hysteresis corresponding to the unstrained and strained state was recorded, and from the magnetic hysteresis, the coercive field for the unstrained state was 5.9 mT and reduces to 5.8 mT for strained state. The normalized squareness (μ_r/μ_s) ratio for unstrained sample state is 0.90 which reduces to 0.83 at strained state. This is a clear indication that the FeGa thin films sputter deposited even at higher sputter power (10 at % Ga) are strain sensitive.

A MOKE measurement of 30 nm FeGa thin film sputter deposited at very low sputter power (20 W) is shown in Fig. 45. The coercivity of the FeGa

thin film without strain was 3.7 mT and by applying strain the coercivity reduces to 2.6 mT. The normalized squareness ratio of the unstrained FeGa film was 0.85 and the strained sample show squareness ratio of 0.79. The change of the squareness ratio from the unstrained state to the strained state shows that it is possible to change the magnetization of a 30 nm FeGa film by applying strain. It can further be observed that the coercive field of thin FeGa film (unstrained) is just 3.7 mT indicating that it can be used as a soft magnetic material. Therefore FeGa thin films sputtered at 20 W can be used as a soft magnetic as well as inverse magnetostrictive sensing layer in the TMR junctions.

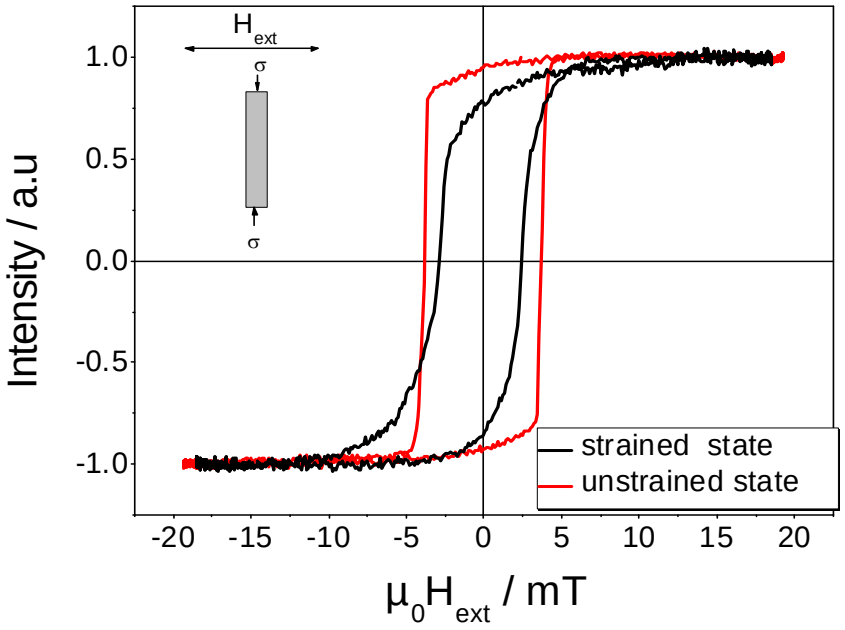

Fig. 45: MOKE Measurements of a 30 nm FeGa thin film sputtered at 20 W. The longitudinal axis of the cantilever was perpendicular to the field during the measurement. The inset drawing shows the direction of the external field and the applied compressive stress.

On the basis of gallium content from the EDX measurements in section 4.1.1 sputter powers between 20 W and 400 W were assumed to show high magnetostriction. This can be verified by measuring the magnetostrictive properties of the FeGa thin film at various sputter powers by utilizing the cantilever deflection set up shown in section 3.3.3. For these measurements three sputter powers: 20 W, 200 W and 400 W were chosen. Fig. 46 is a measurement of magnetoelastic coupling factor, b as a function of the applied field for FeGa thin film deposited on a MgO (100) single crystal

substrate. The film was sputtered at 400 W in the presence of magnetic forming field and the thickness of the film was 800 nm.

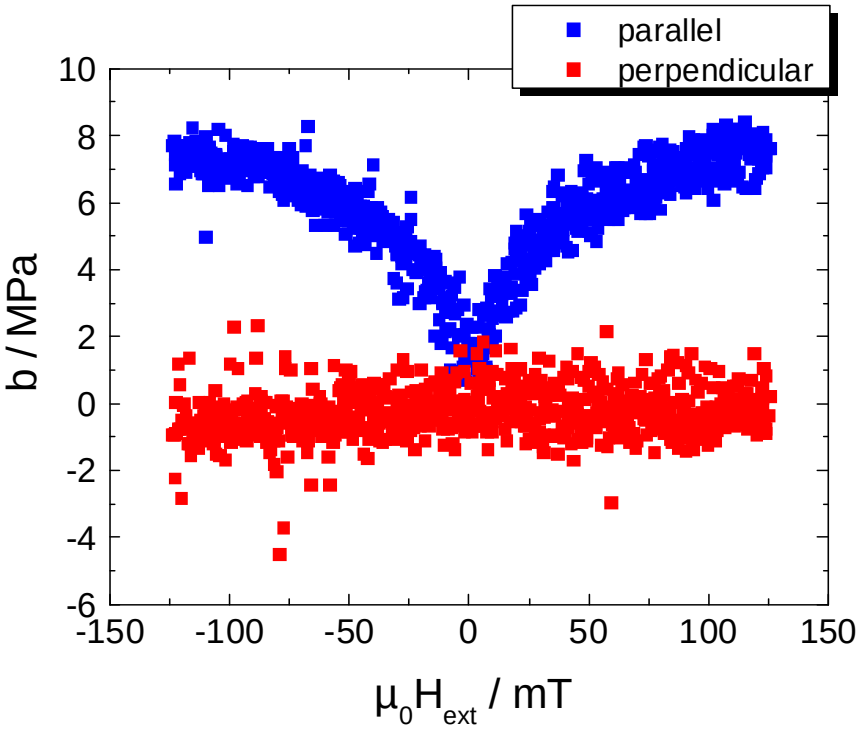

Fig. 46: Magnetostriction measurement of FeGa as sputtered at 400 W sputter power and 800 nm thickness.

When the longitudinal axis of the cantilever was parallel to the external field direction, a deflection of the cantilever was measured. This behaviour as expected proves that the sputter deposited FeGa thin films are positive magnetostrictive. From the deflection of the cantilever the magnetoelastic coupling factor was calculated as 7.5±0.5 MPa. When the longitudinal axis of the cantilever was perpendicular to the external field direction the value of b was close to zero (as shown in Fig. 46). The saturation magnetostriction (λ_{sat}) was calculated using equations (21) and (22). The value of the λ_{sat} for FeGa sputter deposited at 400 W was calculated as $100\pm10*10^{-6}$. The Young's modulus and Poisson's ratio values for FeGa film were assumed as 77 GPa[101] and 0.3[102] respectively. The Young's modulus for MgO was taken as 249 GPa[103] and Poisson's ratio as 0.18[103].

The magnetostriction of FeGa sputter deposited at 20 W and 200 W were also measured. To measure noise free magnetostriction measurements from our measurement set-up a minimum thickness of 600 nm was required.

Therefore the thicknesses of both samples were maintained at 600 nm. The value of $b_{parallel}$ for 20 W was 7±0.5 MPa and $\lambda_{parallel}$ was $90\pm10*10^{-6}$. A small increase in the magnetostriction was observed for films sputtered at 200 W and the corresponding b value was calculated as 7.5±0.5 MPa and $\lambda_{parallel}$ was $100\pm10*10^{-6}$. For both sputter powers the measurement of magnetostriction did not show any effect above the noise level when the field was perpendicular to the cantilevers longitudinal axis.

Magnetostriction measurements of FeGa thin films were also performed by Basant Kumar et al[102]. They assumed the value of Young´s modulus for FeGa film between 72.4-86.3 GPa and sputter deposited FeGa on glass and tungsten substrate to achieve a maximum magnetostriction of $147*10^{-6}$. The gallium composition of their film showing the above mentioned magnetostriction was 18.4 at %. Wang et al[86] studied the magnetostrictive and structural properties of FeGa sputter deposited from a sputter target of composition $Fe_{81}Ga_{19}$. They reported a $50*10^{-6}$ magnetostriction for as deposited films. They used Si (100) as the substrates. The magnetostriction properties of FeGa thin films were also studied by Javed et al[104]. They measured $60*10^{-6}$ to $70*10^{-6}$ λ_{eff} for Ga composition varying from 19 to 24 at %. They further concluded that FeGa films sputtered at $3*10^{-3}$ mbar are magnetically soft.

Two sputter powers were chosen for the deposition of FeGa thin films in the TMR junctions. A 200 W sputter power to sputter deposit FeGa thin film for the thick and thin FeGa electrode based TMR junctions. It was known from the section 4.1.2 that at 200 W sputter power FeGa grows (200) oriented on MgO (100) single crystal substrate, which might result in high TMR ratio because of coherent tunneling. A 20 W sputter power was used to deposit the sensing layer on top of CoFeB on exchange bias based TMR junctions. Low sputter power means small activation energy of the sputtered FeGa. This would avoid intermixing or diffusion of CoFeB and FeGa during sputter deposition.

4.2 Tunneling magnetoresistance (TMR) junctions with FeGa electrodes and MgO tunnel barrier

TMR junctions with MgO tunnel barrier and FeGa electrodes were fabricated based on two basic configurations namely the thick and thin FeGa ferromagnetic electrode based TMR junctions and exchange bias based

TMR junctions. The principle behind the above mentioned junctions are discussed in section 2.4.3.

4.2.1 Thick FeGa electrode and thin FeGa electrode based TMR junctions

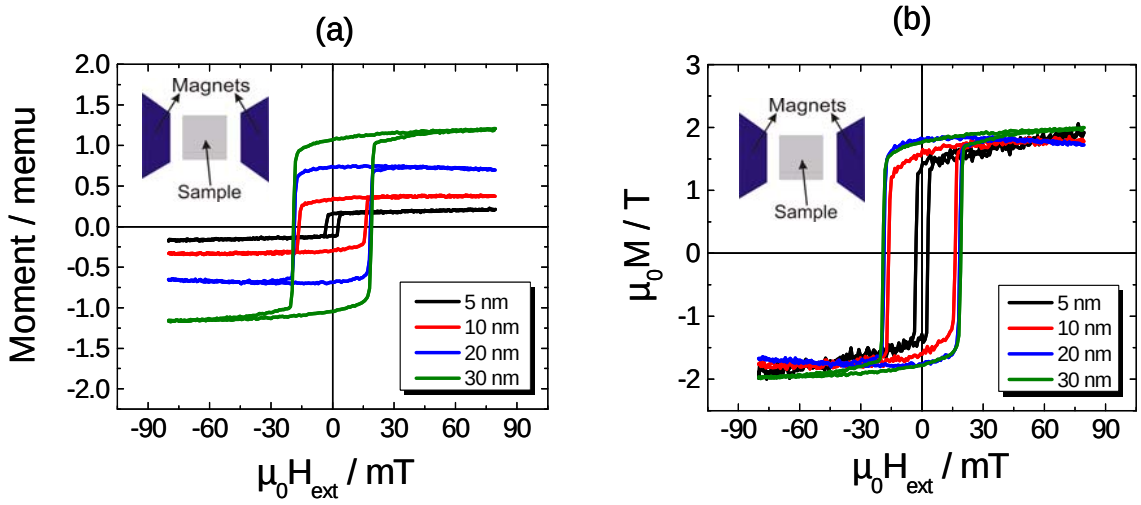

Fig. 47: VSM measurement of FeGa thin films of varying thicknesses sputter deposited at 200 W sputter power and argon pressure of $4*10^{-3}$ mbar on 5 mm x 5 mm MgO substrates. (a) Magnetic moment of the FeGa films plotted against the external magnetic field and (b) moment converted to magnetization (by dividing the moment by volume) and plotted against applied external magnetic field.

To realize a full TMR effect a well separated parallel and anti-parallel magnetization alignment should be achieved in the junctions. The simplest way to achieve this is by using two ferromagnetic materials with different coercive field. In general hard ferromagnetic and soft ferromagnetic materials are used on either sides of the barrier layer to achieve different coercive fields[46]. A VSM investigation of FeGa thin films of different thicknesses sputter deposited at 200 W and $4*10^{-3}$ mbar argon pressure are shown in Fig. 47. The setup of VSM is discussed in section 3.3.1. MgO single crystal substrates of dimension 5 mm x 5 mm were used for the sputter deposition of FeGa. The position of the sample during the measurement is also shown as an inset diagram in Fig. 47.

From the figure the coercive field of 5 nm FeGa thin film is 2.9 mT and when the thickness was increased to 10 nm the coercivity increases to 16.3 mT. This behaviour could be because the grain growth increases with

thickness, the bigger the grain size the larger the coercive field[105]. Further increase in thickness to 20 nm and 30 nm does not show a considerable increase in the coercivity. The change in the coercive field was reduced when the grain sizes are close to optimum at about 30–40 nanometers[106]. Table 6 shows the change in the coercive field for FeGa thin films with varying thicknesses. A 20 nm FeGa film show 18.5 mT coercive field and the coercive field of a 30 nm thick FeGa film is 19 mT, whereas a 5 nm film show just 2.9 mT coercivity. Therefore a 5 nm FeGa thin film can be used as a soft ferromagnetic electrode and 30 nm FeGa can behave as hard magnetic electrode under the external field.

Thickness (nm)	Coercive field, Hc (mT)
5	2.9
10	16.3
20	18.5
30	19.1

Table 6: The increase in the coercive field of the FeGa thin films taken from the VSM measurements of sample shown in Fig. 47.

The principle behind the thick and thin FeGa electrodes based TMR junction can be motivated by Fig. 47b. When a strong negative external field was applied both FeGa electrodes are saturated into the same direction resulting in a parallel configuration (P) of magnetization. Increasing the field saturates the thin FeGa film in the new direction first; the thick FeGa still shows no change in the magnetization. This results in an anti-parallel (AP) configuration of magnetization. At higher external magnetic field the thick film is also saturated resulting in parallel (P) magnetization of both thick and thin films (not shown in the figure). Therefore well separated parallel and anti-parallel magnetization states are expected to be achieved by varying the thickness of FeGa in the TMR junction. The preparation of TMR stacks and the stack configuration are mentioned in the section 3.1.2.1.

A cross-sectional TEM image (Fig. 48) shows the stack configuration of an as prepared TMR junction. It can be observed that there is a sharp interface boundary between MgO barrier layer and FeGa electrodes. Hence a direct magnetic coupling between the two FeGa layers can be ruled out. The tunnel junction was covered by tantalum and gold capping layer to avoid any further oxidation or contamination of the top FeGa thin film.

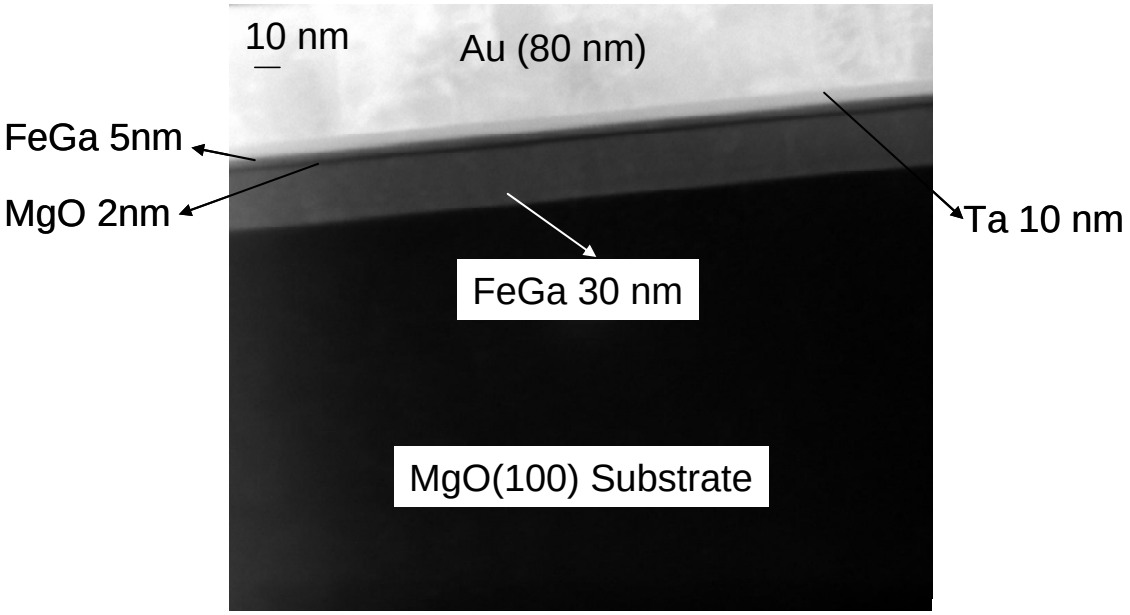

Fig. 48: A cross-sectional TEM image showing the stack configuration of the as prepared TMR junction on MgO (100) substrate.

An in-plane VSM investigation of as prepared TMR stacks is shown in Fig. 49. It was shown by Javed et al[107] that by applying a forming field during sputter deposition FeGa thin films showed a hard axis and easy axis of magnetization. As mentioned in section 4.1 FeGa thin films during this work were sputter deposited by applying a forming field. The VSM measurement of as deposited FeGa based TMR stacks shows that an in-plane induced anisotropy was well established. The positions of the sample during the measurements are shown also as an in-set diagram in the figure. The anisotropy was observed by rotating the sample 45° from the hard axis. This suggests the rotation of FeGa lattice by 45° to grow on MgO substrate as suggested by Butera et al[18].

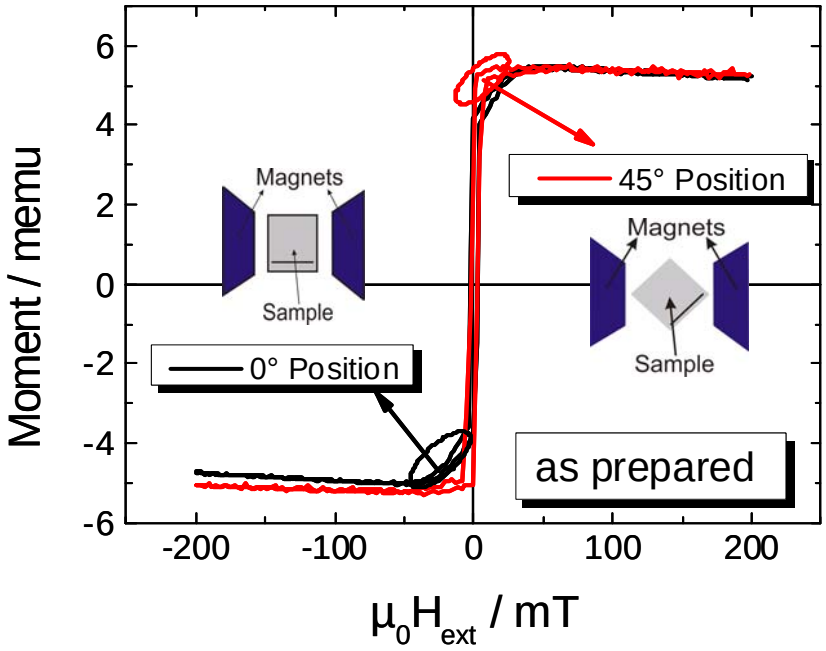

Fig. 49: VSM measurement of an as prepared TMR stack on 10 mm x 10 mm MgO substrate. The hard axis was observed by rotation of the sample 45° from the easy axis.

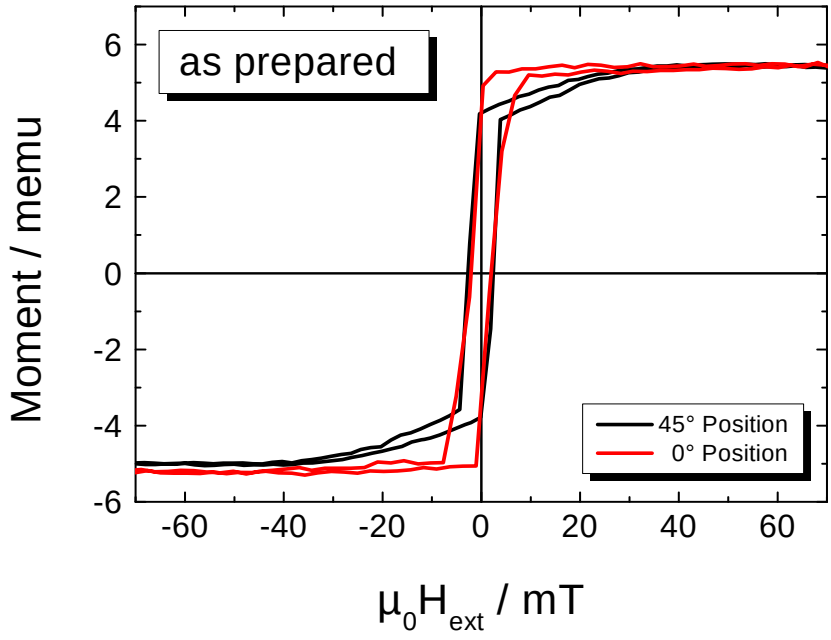

Fig. 50: Magnified image of VSM measurement of as prepared TMR stack on 10 mm x 10 mm MgO substrate.

Fig. 50 is the magnified image of the magnetic hysteresis measurement of an as prepared thick and thin FeGa based TMR junction by VSM. The junctions show magnetic moment value of ±5.25 memu. When the external field was about 2.9 mT the magnetization of the thin FeGa film completely switches towards the external field (saturation). Due to a magnetic interlayer coupling (e.g. orange peel coupling) between the thick and thin FeGa films the magnetization of the thick FeGa film switches spontaneously in the direction of the magnetic field before the coercive field of 19 mT was reached. Further increase in the field rotates the magnetization of the thick FeGa until it reaches saturation. At this point both thick and thin FeGa films were saturated. By reducing the field back to zero and further to the negative saturation the same behavior was observed.

4.2.2 Magnetoresistance measurements

Magnetoresistance measurements were performed by placing the sample between the pole pieces of a solenoid. The experimental setup and measurement procedure can be looked up in section 3.3.4. Fig. 51 shows a magnetoresistance measurement of a 10 µm x 10 µm as prepared (as fabricated) TMR junction.

At the beginning of the looping field (negative saturation) the magnetization of both FeGa electrodes are parallel to each other resulting in parallel resistance state (P). Increase in the magnetic looping field towards zero gradually increases the resistance. A sudden large increase in the resistance could be observed near zero field. This happens when the external field corresponds to the coercive field of thin FeGa film (5 nm FeGa). The anti-parallel configuration of magnetization was approached but not achieved, as further increase in the field sweep decreases the resistance.

This is because a further increase in external field results in partial switching of the thick FeGa film due to the magnetic coupling between the ferro-magnetic electrodes (as explained in section 4.2.1) resulting in the sudden reduction of the resistance (showed by blue down arrow in Fig. 51). Presence of domains in the thick FeGa electrode results in the rotation of domains towards the field resulting in stepwise reduction of resistance (shown by red circle). When all the domains are magnetized in the direction of the external field the resistance drops to the parallel state. Again both electrodes are magnetized in the parallel direction. Looping the field back

the magnetization of the thin FeGa film rotates first followed by the thick FeGa electrode resulting in nearly symmetrical magnetization loops. The resistance at parallel state was 4420 Ω and anti-parallel resistance was 4850 Ω. The corresponding TMR ratio and resistance area (RA) product were 9.3 % and 442 kΩμm^2. Therefore for our samples a stable anti-parallel state which is important to realize the full TMR effect was not observed. The RA product is usually calculated taking the value of the resistance when the magnetizations of both FeGa electrodes are parallel to each other and by multiplying it with the area of the corresponding TMR junction being measured. The above mentioned 9% TMR ratio is comparable to the TMR ratio reported by other groups[108,109,110] for not annealed (as prepared) TMR junctions. The work of these groups shows that a further increase in the TMR ratio was possible by annealing of these junctions.

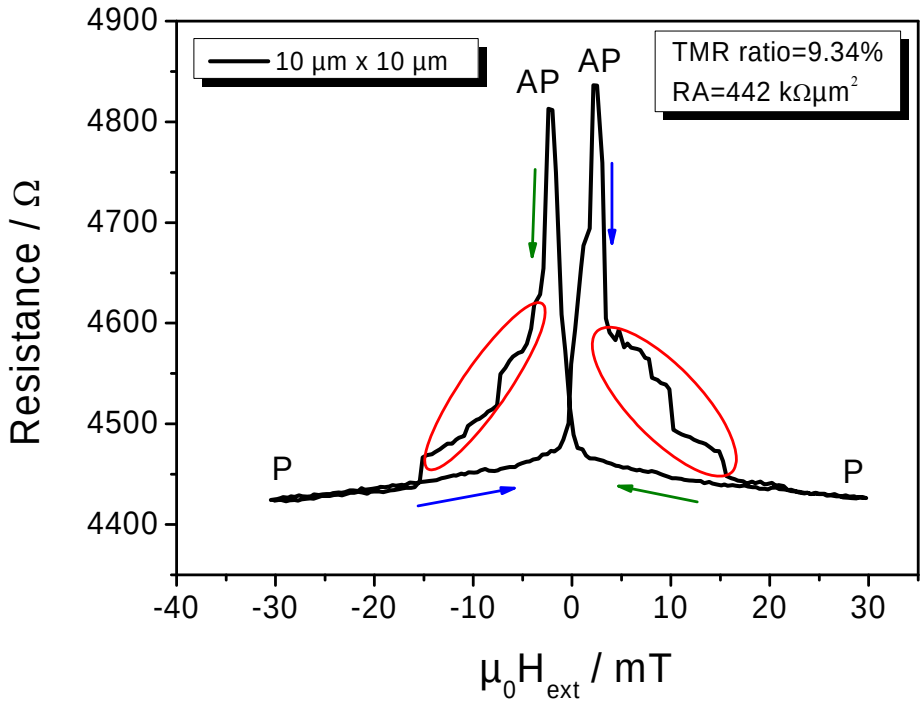

Fig. 51: Magnetoresistance measurement of an as prepared 10 μm x10 μm TMR junction. The junction show a partially stable minor loop and build up of domains in the thick FeGa electrode (red circles). P denotes the parallel resistance and AP the anti-parallel resistance states respectively

Fig. 21 of section 3.1.4 shows the lithography mask layout used for the fabrication of TMR junctions of various sizes. The size of the mask used for lithography was 100 mm x 100 mm and the sample size was 10 mm x 10 mm. A good vacuum contact was not achieved during UV-lithography. As a result junctions smaller than 100 μm^2 were not properly realized (shown in Fig. 52) for the above mentioned sample sizes. Therefore for further analysis only 2500 μm^2, 400 μm^2 and 100 μm^2 junctions were chosen. Further it is expected to observe a constant TMR ratio and a constant resistance area product independent of the size of the TMR junctions.

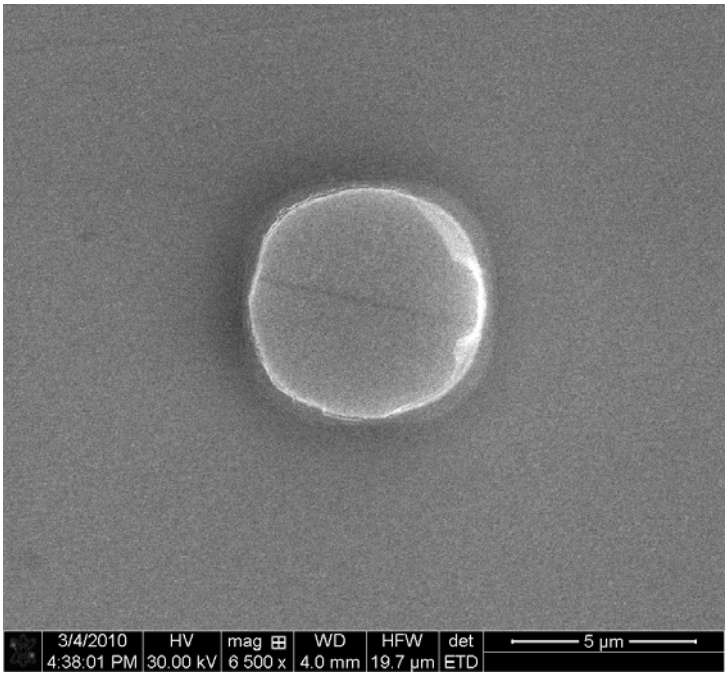

Fig. 52: SEM image of a nominally (5 µm x 5 µm) sized TMR junction after UV-lithography showing clearly visible corner rounding.

The dependency of the TMR ratio on the absolute area of the junctions is shown in Fig. 53. It can be observed that many 100 μm^2 and 400 μm^2 show TMR ratio of about 8-9 %. All of the measured 400 μm^2 junctions show an average TMR ratio of 8-9 %. The 400 μm^2 junctions also show the smallest spread of TMR amplitudes. Most of the 2500 μm^2 junctions show TMR ratio below 6%. In the as prepared junctions, high TMR ratio was observed for smaller junction sizes.

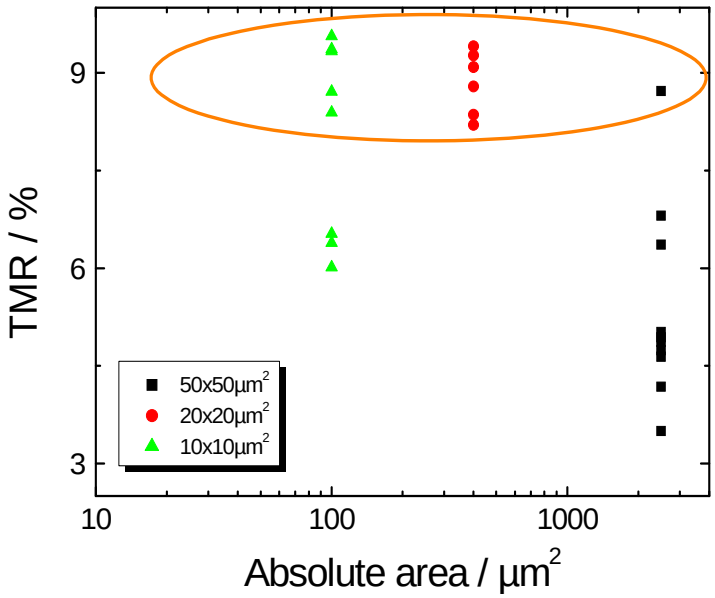

Fig. 53: TMR versus absolute area of the as prepared TMR junctions

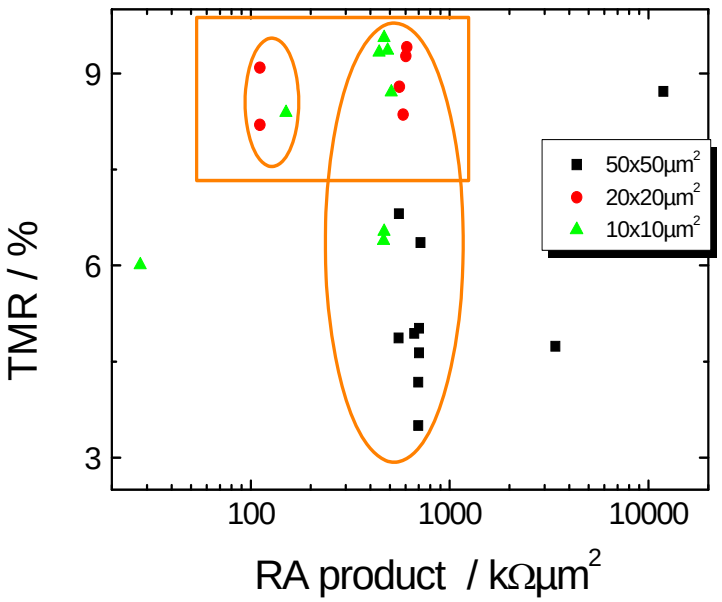

Fig. 54: TMR versus resistance area (RA) product of the as prepared TMR junctions

The resistance area product of the TMR junctions as a function of TMR ratio is plotted in Fig. 54. In general, majority of junctions show RA in the range of 400-700 kΩµm^2 for all junction sizes. Two groups of RA product were observed for junctions showing TMR ratio above 8 %. The first group shows

3 junctions having RA in the range of 100 kΩμm^2 and the second group has a RA product of 500-600 kΩμm^2. High density of working TMR junctions which show parallel state and approaching the anti-parallel state were found for the junctions sizes 10 μm x 10 μm and 20 μm x 20 μm. The 50 μm x 50 μm junctions has large defects probability may be because of the lithography processes resulting in the reduction of the TMR ratio.

It is well known that annealing the TMR junctions based on MgO barrier above 300°C results in very high increase in TMR ratio[14,111]. Annealing induces crystallization of the thin film in direct interface with the MgO barrier layer resulting in coherent tunneling between the barrier and the electrodes, thus increasing the TMR ratio. Since the thick and thin FeGa electrodes based TMR junctions also have an MgO barrier layer, annealing at high temperatures was expected also to increase the TMR ratio. Therefore the thick and thin FeGa electrode based TMR junctions were annealed at 350°C for 1 hour and a magnetic field was applied during annealing and cooling down to induce the easy axis.

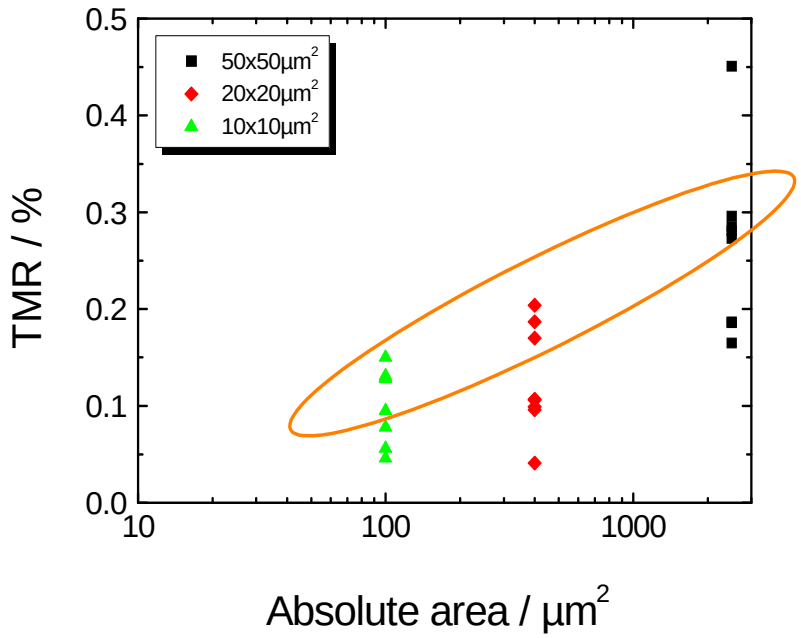

Fig. 55: TMR versus absolute area of thick and thin FeGa based TMR junctions after annealing at 350°C for 1 hour. A magnetic field of 230 mT was applied during annealing and cooling.

Fig. 55 shows the TMR ratio as a function of the absolute area for the samples annealed at 350 °C. These samples were prepared in the same way

together with the samples shown in Fig. 53, but annealed at 350°C before the measurement of magnetoresistance. It can be observed that the overall TMR ratio has reduced from 6-9 % (for as prepared junctions) to about 0.2 % - 0.3 % for annealed junctions.

The TMR ratio of the annealed junctions as a function of the resistance area product is shown in Fig. 56. The RA products are in the range of 15-300 $k\Omega\mu m^2$. The fact that the TMR ratio and RA decreases together with decreasing absolute area of the junctions shows that annealing reduces the overall TMR ratio in the junctions by introducing parallel spin-independent current paths. One possible explanation for these parallel current paths could be because of the Ga diffusion into the barrier layer.

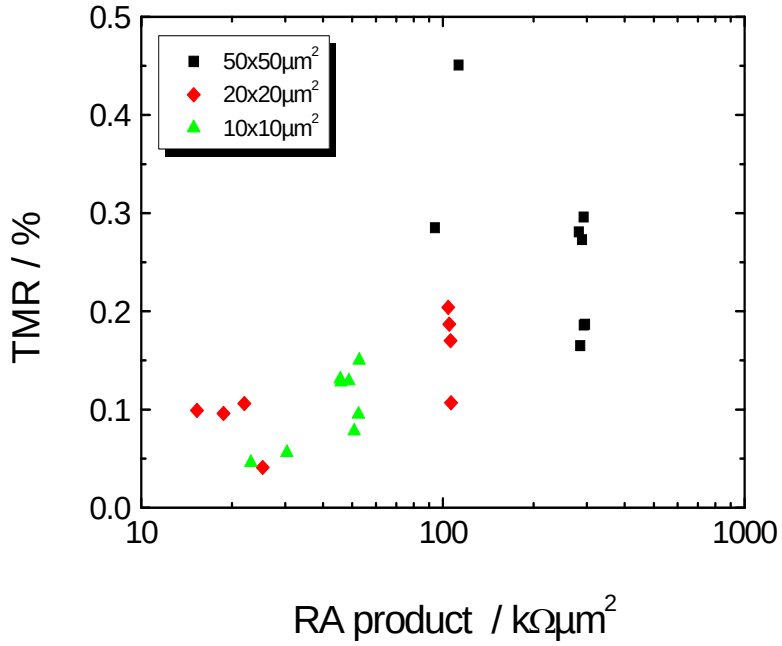

Fig. 56: TMR versus resistance area (RA) product of thick and thin FeGa based TMR junctions after annealing at 350°C for 1 hour. Magnetic field (230 mT) was applied during annealing and cooling down.

A VSM investigation of the TMR stack annealed at 350°C is shown in the Fig. 57. The sample shows a decrease in the magnetic moment from 5.25 memu (shown in Fig. 49) to 3.25 memu. This decrease in the magnetic moment could be also because of the reduction in Ga content of the FeGa film during annealing.

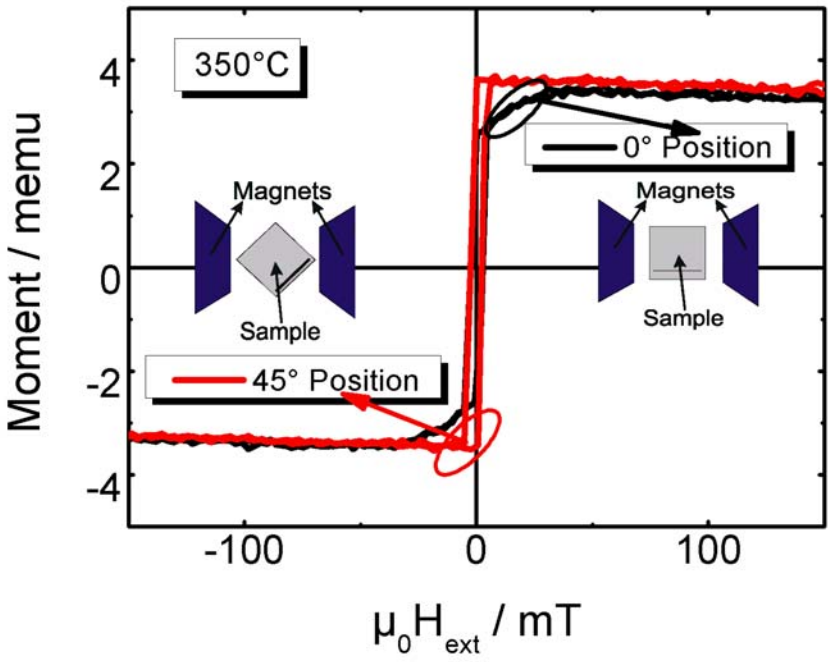

Fig. 57: VSM measurement of a TMR stack on 10 mm x 10 mm MgO substrate after annealing at 350°C.

To understand further the reason for the reduction of TMR ratio and magnetic moment, TEM investigation was performed. The samples with the following stack configuration were sputter deposited on the MgO (100) oriented substrates:

FeGa (50nm) / MgO (50nm) / FeGa (50nm) / Ta (10nm)

The sputter power for deposition of the FeGa thin film was 200 W in the presence of magnetic forming field at $4*10^{-3}$ mbar argon pressure. For MgO thin film 100 W sputter power and $3*10^{-3}$ mbar argon pressure were supplied. One sample was analyzed as prepared in TEM and the other sample was annealed at 350°C for 1 hour in the presence of magnetic field to study the effect of annealing on the structural and chemical properties of the samples. The sample preparation by FIB cutting in most cases utilizes Ga ions source, resulting in Ga contamination of the TMR stacks. In order to avoid Ga contamination the samples for TEM were prepared by conventional thinning.

Fig. 58a shows an overview of the FeGa and MgO layers of the as deposited thin films. From the bright field image of the stacks (Fig. 58a), it can be clearly seen that the interface between the first FeGa layer and the MgO layer is sharp and well defined. At the boundary between the second FeGa layer and MgO layer the roughness increases, typically in the order of about 2-5 nm. Fig. 58b is the EDX spectra of FeGa, MgO and tantalum layers. The approximate thickness for each layer is about 50 nm and a 10 nm Ta protection layer can also be detected. At the interface between the FeGa layers and MgO layer a gradual transition can be observed. From EDX the thickness of this transition zone was roughly 5 nm. This transition can be also observed for the first FeGa and MgO layers interface, but the bright field image shows a sharp interface between these layers. This could be because the sample was tilted at a certain angle to the electron beam during the measurement.

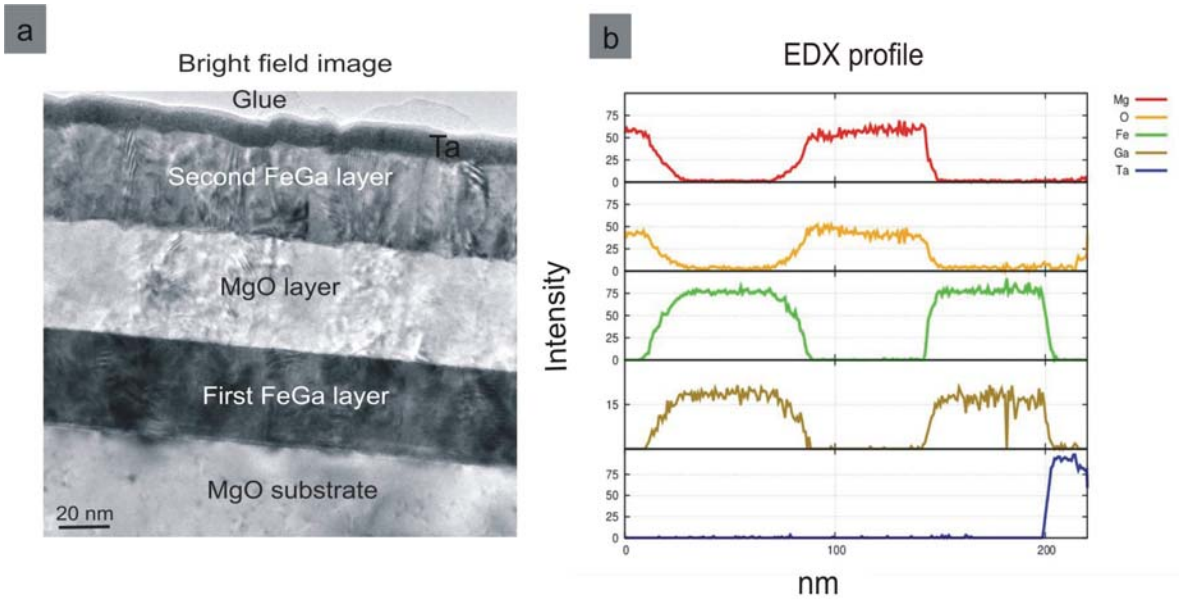

Fig. 58: (a) Overview of a TEM image and (b) EDX profile of as prepared FeGa and MgO layers with a Ta capping layer on the MgO substrate

Shown in Fig. 59a and Fig. 59b are the high resolution images of the first and the second FeGa layers grown on the MgO substrate. From the figure it can be seen that the interface between the first FeGa and MgO layer is very sharp. A local epitaxial growth was observed in these layers and one such area is indicated by a red box in the figure. The second interface was rougher as compared to the first FeGa layer. All layers were polycrystalline. To analyze the composition of Ga and Fe at these interfaces EDX was

performed at the boundaries between FeGa and MgO layers. The ratio of Fe:Ga was determined as ~82:18 in both FeGa layers. This ratio is equal to the Fe:Ga ratio for the FeGa thin film sputtered at 200 W sputter power measured by EDX measurements (in section 4.1.1).

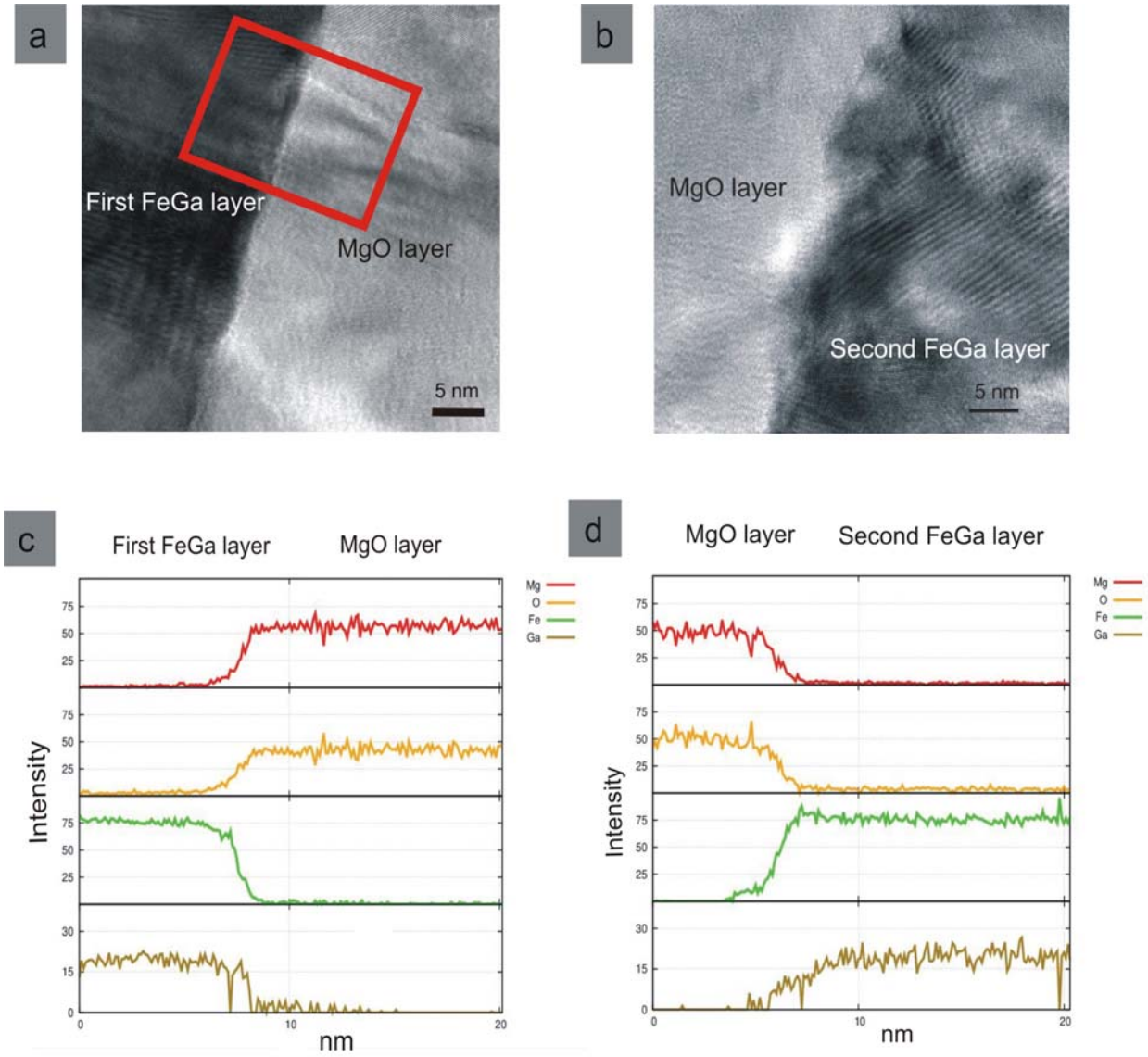

Fig. 59: (a) High resolution images of as prepared sample showing the sharp interface between the first FeGa layer and the MgO layer, (b) High resolution image of the MgO and second FeGa layer showing a not so sharp interface, (c) and (d) EDX profile of the above mentioned layers.

From EDX spectra in Fig. 59c and Fig. 59d one can see that there is no sharp interface as seen in the high resolution micrographs. An overlap of the layers to about 2 nm was observed. This is probably due to the beam resolution and a slight tilt of the sample to the beam. The EDX profile of the first FeGa and MgO layer interface show a small signal of Ga inside the MgO layer. This signal was invalidated by making measurements at other spots and no such behaviour was observed in other spots. Therefore this small signal of Ga was concluded as noise.

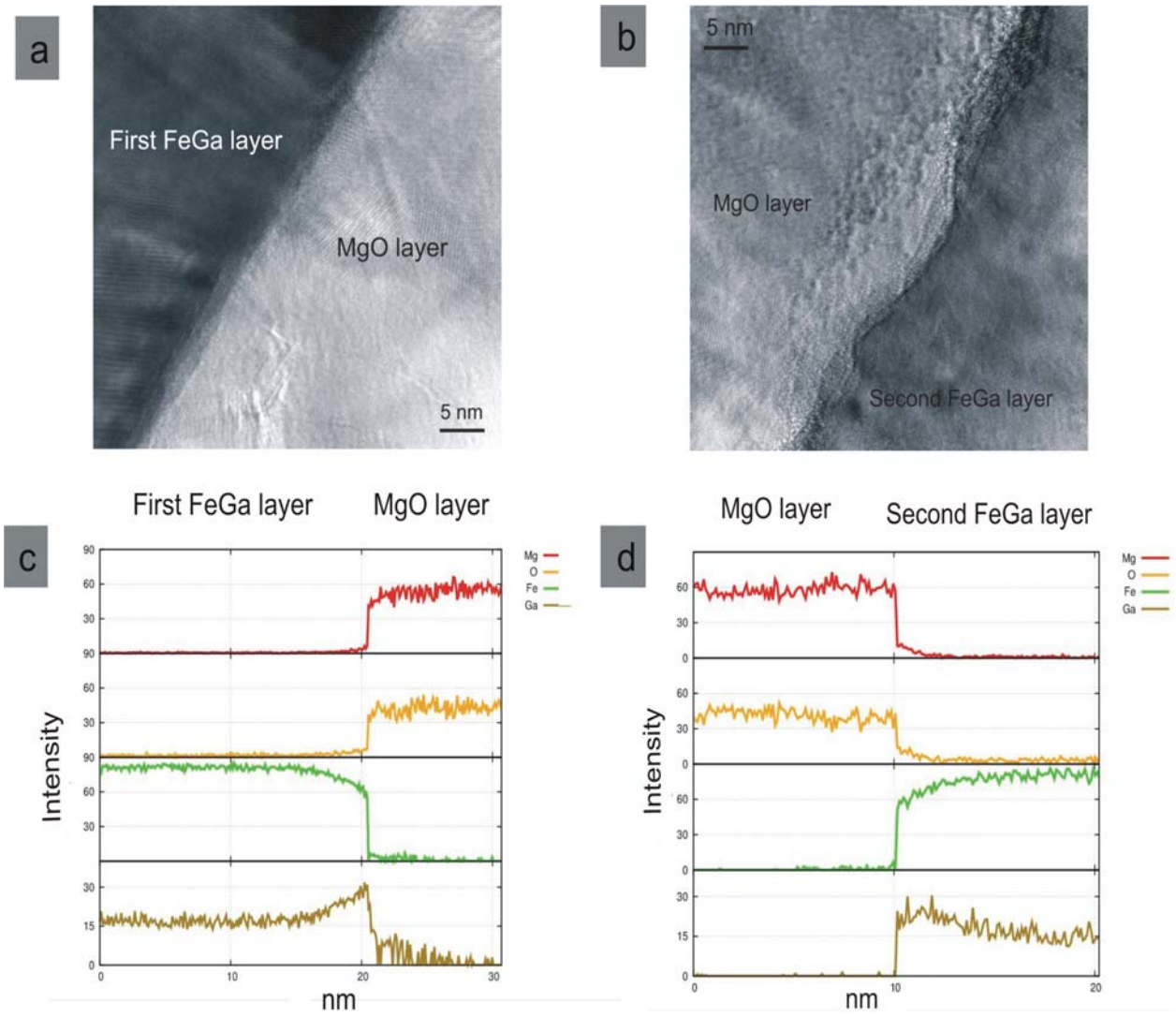

Fig. 60: (a) High resolution images of samples annealed at 350°C showing the sharp interface between the first FeGa layer, (b) the second FeGa layers´s interface with MgO layer, (c) and (d) EDX profile of the above mentioned layers.

Fig. 60 (a) and (b) shows the high resolution images of the first and second FeGa layer in interface with MgO layer after annealing. The interface between the first FeGa layer and MgO layer is still flat and sharp, but no local epitaxial growth was observed in the first FeGa layer. The second FeGa layer is rough as compared to the as prepared sample. The EDX profile (Fig. 60 (c) and (d)) show no direct overlapping of the layers. The interface is actually sharper which was not expected. But this could happen because of the drift correction image. When an EDX profile is performed at a particular area of the sample, the computer scans the reference image at a given time interval to check if the sample drifted from the reference position. If drifted the sample position will be adjusted to reference position. This is called drift correction image. This might have shifted the sample a few nanometers back resulting in such sharp interfaces.

Further from the EDX scan spectra it can be observed that at both interfaces between the FeGa and MgO layers there is a sharp increase in the Ga signal and a decrease in the Fe signal. The increase of Ga signal starts about 5 nm before the interface. Until about 2-5 nm inside the MgO layer Ga signal was observed. In contrast to Fig. 59 it was verified at the first interface for the annealed samples that the Ga signal has an intensity higher than the background noise. At the second interface the same behaviour was also observed, but it is more diffuse because of the rough interface. The EDX compositional analysis performed at the first interface show the Fe-Ga ratio to be 70:30 at %. At the center of the FeGa layer Ga percent was reduced to about 15 at %. At the second layer also we can see a sharp increase of the Ga signal towards the interface. The composition of Ga inside the second layer was 14 at %. At the interface between FeGa and MgO the ratio of Fe:Ga was 70:30 at %.

This is a clear indication that the Ga in the FeGa upon annealing (at 350 °C) diffuses towards the interface layer (MgO barrier layer). From Fig. 59 and Fig. 60 at the FeGa and MgO interface Ga diffuses to a few (2-5 nm) nanometers into the MgO layer. Therefore the reduction in the TMR ratio observed from the magnetoresistance measurements of the annealed samples compared to the as prepared (un-annealed) samples and the reduction of the magnetic moment of the annealed samples from the VSM measurements were due to the diffusion and movement of Ga into the MgO barrier layer.

4.3 Exchange bias based TMR junctions with FeGa sense layer and MgO tunnel barrier

The thick and thin FeGa electrodes based TMR junctions did not show high TMR ratios as well as stable anti-parallel configuration of magnetization. It was verified in section 4.2.1 that annealing of FeGa thin film in direct interface with MgO layer results in the Ga diffusion into the MgO layer. Introduction of a thin CoFeB interlayer might avoid Ga diffusion into the barrier layer. It is well known that CoFeB/MgO/CoFeB based exchange biased TMR junctions show stable sensing layer and high TMR ratio[14] at room temperature. Deposition of FeGa on amorphous CoFeB surface does not require MgO single crystalline substrates. MgO sputter deposited on amorphous CoFeB grows (001) oriented[111] and annealing the CoFeB and MgO interface based TMR junction at temperatures as high as 375°C[112,113,91,55,114] induces crystallization of CoFeB in (001) crystallographic direction because of the small lattice mismatch between MgO (001) and CoFeB (001)[115]. The result is coherent tunneling and high TMR ratios at room temperature. Therefore in this section exchange bias based TMR junctions with configuration similar to CoFeB/MgO/CoFeB are investigated. The general stack configuration of these exchange bias based TMR junctions were discussed in the experimental section 3.1.2.2.

4.3.1 Exchange bias based TMR junctions with 2 nm CoFeB interlayer

The stack configuration of the exchange bias based TMR junctions with 2 nm CoFeB interlayer is shown below:

TaN 5 nm / Ta 5 nm / PtMn 25 nm / CoFe 2.5 nm / Ru 0.8 nm /
$CoFe_{40}B_{20}$ 4 nm / Mg 1.5 nm / MgO 1.5 nm /
$CoFe_{40}B_{20}$ 2 nm / FeGa 20nm / Ta 5 nm / Ru 10 nm

The stack was sputter deposited by Siemens AG in Erlangen, Germany until the 2 nm COFeB (above the MgO barrier layer). A dual chamber DC magnetron sputter system (KENTOTEC) was used for the deposition. The system has eight sputter targets (4 targets / chamber). FeGa, tantalum and ruthenium were sputter deposited at our clean room facility (in the Kieler Nanolabor). Accordingly there was a vacuum break in between the deposition of TMR stacks until the top CoFeB film and the FeGa with top

electrodes. A magnetically stable reference layer was provided by PtMn / CoFe / Ru / CoFeB artificial anti-ferromagnetic exchange coupled sandwich layers. The anti-ferromagnetic alignment of CoFe and CoFeB arises due to the interlayer exchange coupling. A CoFeB / FeGa layer was used as sensing layer. The MgO barrier layer separates this magnetostrictive layer from the reference layer. The masks used for the lithography are shown in Fig. 22 of section 3.1.4. The TMR stacks deposited on the wafer were patterned in three steps of lithography. The first step was to fabricate bottom electrodes. Fig. 22a shows the mask used to structure the bottom electrodes by UV lithography. The parameters used can be looked up also in section 3.1.4. After structuring by lithography the stack was etched in IBE. The parts of the stack which were covered by photoresist remained un-etched and the rest of the stack (which was not covered by resist) was etched by Ar ions until the beginning of the barrier layer. A second lithography was performed again on this wafer using the mask shown in Fig. 22b. This lithography was performed to fabricate the TMR structures and the ground electrodes, which were release etched by IBE.

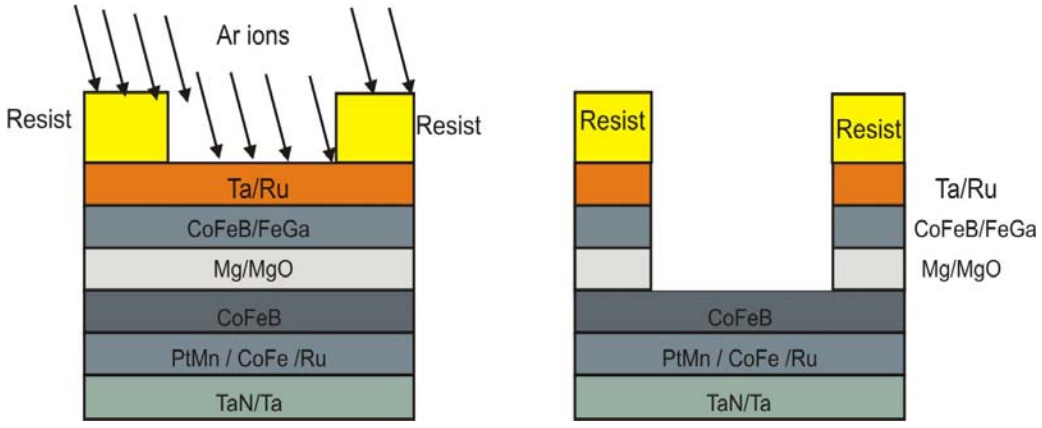

Fig. 61: Release etch of the TMR stack by Ar ions in IBE to form free standing TMR junctions.

Fig. 61 shows free standing TMR junctions after the second release etch in IBE. SiO_2 was sputter deposited after the second etch to cover the etch trench around the TMR junctions and the bottom electrode. SiO_2 deposition ensures that the electrical current passes from the TMR structures to the bottom electrodes only through the ground electrode during a two point magnetoresistance measurement. A third lithography using the mask in Fig. 22c enables the fabrication of contact pads. The contact pads facilitate easy

contact of the precision needles between the ground electrodes and the TMR junctions for magnetoresistance measurement.

The TMR junctions were fabricated on the wafer level and was annealed at 285°C for 100 minutes at 320 mT to establish the exchange bias. Exchange bias was not achieved during this field annealing due to the poor thermal contact between the heating stage and the wafer. So the wafer was diced into cantilevers of dimensions 3 mm x 23 mm. The various junction sizes realized for this configuration are mentioned in Fig. 34 of section 3.3.4. The diced cantilevers were annealed again in the presence of 320 mT magnetic field but at various annealing temperatures to study the effect of annealing temperature on the junctions. Exchange bias was established on the diced cantilever pieces. The effect of various annealing temperatures on the TMR ratio of the junctions will be discussed below in detail. The minor loop, the major loop and the IV-curve measurements of one of the junction at a particular annealing temperature will be discussed first, followed by the comparison of the TMR ratio as a function of absolute area and the RA product of various junction sizes at different annealing temperatures.

The minor loop of a 50 µm x 50 µm junction in Fig. 62a shows that at negative looping field the magnetization of the FeGa sensing layer and exchange coupled CoFeB hard magnetic layer are in the parallel state (P) to each other. Therefore a low resistance was measured. When the magnetic field was increased, the magnetization of the magnetostrictive FeGa layer switches towards the direction of the external field. Hence an anti-parallel state (AP) of magnetization between the reference and sensing layer was observed. When the junction is in the anti-parallel state a high resistance was measured. Exchange biasing induces a stable hard magnetic layer; the result is a plateau at the AP state. The red arrow shows the direction of the forward looping field. When the field was looped back (shown by the blue arrow) the resistance follows a hysteresis like loop called Minor loop. The coercivity of the sense layer can be derived from the minor loop and measures 2 mT. This value is much less compared to the VSM measurements of a 20 nm FeGa (shown in section 4.2.1) thin film. The coercive field measured by VSM is 18 mT. But the MOKE measurements of a 30 nm strained FeGa film measures 2.6 mT (section 4.2.1). Internal stress might be induced in FeGa film sputter deposited on CoFeB during annealing due to the lattice mismatch. This could lead to such soft magnetic behaviour. Another possible reason could be that in the patterned FeGa films domains could be

formed reducing the total energy required to change the magnetization direction.

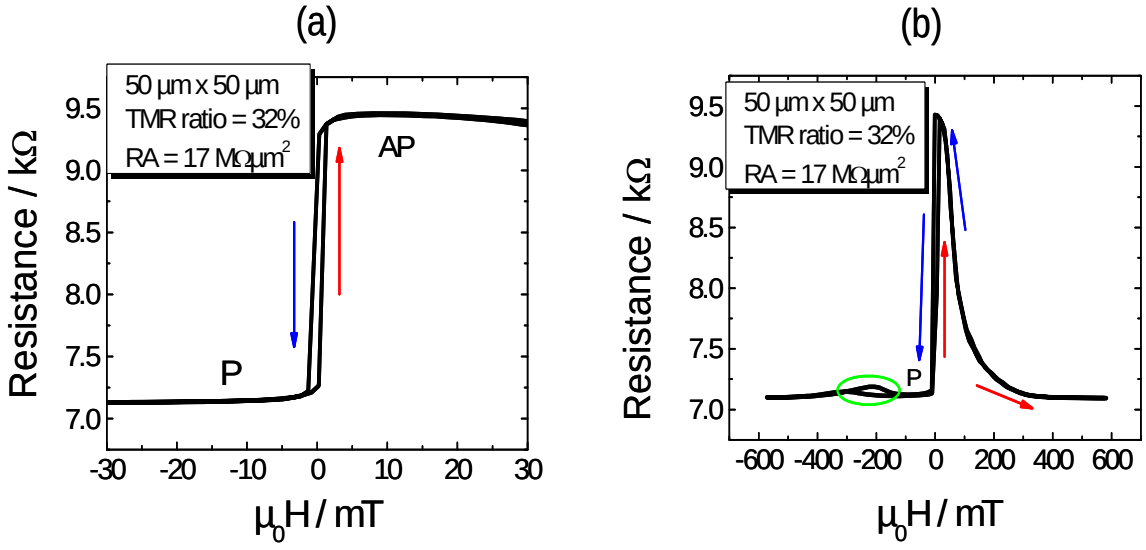

Fig. 62: (a) Minor loop of a 50 µm x 50 µm TMR junction annealed at 400°C for 100 minutes at 320 mT field, (b) Major loop of the same junction. P and AP denote the parallel and anti-parallel configuration of magnetization between the sensing and reference layer. The red arrows denote the forward looping field direction and the blue arrows the reverse looping direction of the applied external field

Fig. 62b shows the major loop of the same 50 µm x 50 µm junction. At large negative fields the magnetization of the reference and FeGa sensing layer are parallel to each other. At higher fields the CoFe coupled to PtMn switches its magnetization towards the direction of the field resulting in a small increase in the resistance between 300-200 mT shown by the green ellipse in the figure. When the looping field was decreased the magnetization of sensing layer rotates first resulting in a high resistance state or AP configuration of magnetization. Increasing the external field (until a certain range of field) showed a plateau corresponding to a stable anti-parallel configuration. Further increase in the external field results in the switching of hard magnetic film showing a low resistance state. Similar major and minor loops behaviour were also measured for samples annealed at 285°C, 350°C, 400°C and 450°C.

The stability of the TMR junctions was characterized by measuring the I-V characteristics. I-V characterizations of various TMR junction sizes were performed by varying the voltage and measuring the current at constant negative and positive bias fields (±60 mT). I-V curve measured for a 50 µm x 50 µm junction annealed at 400 °C is shown in Fig. 63a. The I-V curve for

-60 mT indicates nearly an ohmic behaviour. From the Fig. 63a it can be seen that -60 mT represents parallel configuration. The curve at +60 mT shows non-linear behaviour which is characteristic of tunneling. Such response to the I-V behaviour in parallel configuration was also reported by Hayakawa et al[114]. According to Hayakawa et al. the ohmic behaviour at parallel configuration might arise due to the match of the symmetry of the tunneling electronic states as inferred by the theoretical studies[15,53,116]. Bias voltage higher than 300 milli-volts resulted in the destruction of our junctions. Therefore large bias voltages were not applied to prevent the damage of the junctions.

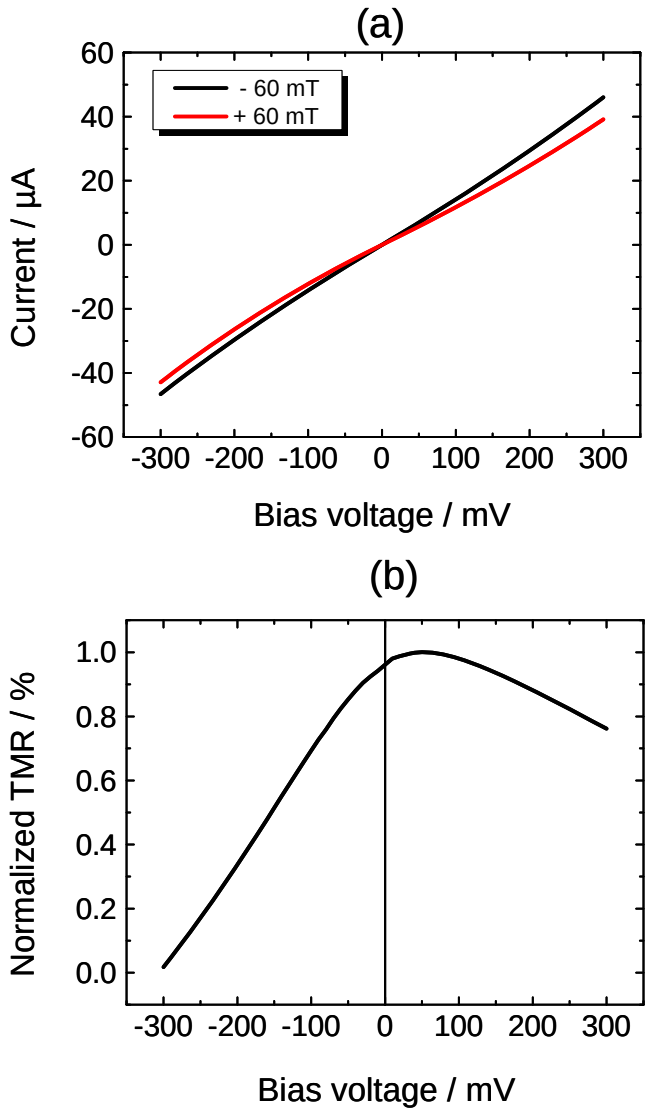

Fig. 63: (a) I-V curves of the junction shown in Fig. 62 at ±60 mT field and (b) normalized TMR ratio calculated from I-V curves versus applied voltage.

From the I-V curves it is possible to calculate the TMR ratio as a function of the bias voltage. A highly asymmetric normalized TMR ratio as a function of the bias voltage is plotted in the Fig. 63b. As there is CoFeB on both sides of barrier a symmetric tunneling was expected. CoFeB as deposited is amorphous and annealing at 375°C re-crystallizes as shown by many researchers. It was shown in the section 4.2 that annealing FeGa at 350°C results in the diffusion of Ga. As the TMR junction corresponding to Fig. 63 was annealed at 400°C, Ga might diffuse into the CoFeB changing the structure of CoFeB in interface with MgO barrier layer. Therefore a difference in the structure at the bottom and at the top CoFeB electrodes is the reason for such pronounced asymmetry.

An asymmetric in the bias voltage dependence of the TMR ratio for CoFeB/MgO/CoFeB based TMR junctions was observed also by Feng et al[117]. They interpreted that the different structure at the top and the bottom of CoFeB/MgO interfaces to be the reason for such an asymmetry, which is in good correlation with our discussion. A shift of the maximum TMR from the zero bias voltage can also be seen in the Fig. 63b. The shift of the maximum TMR was also reported for AlO_x based tunnel junctions by Oepts et al[118]. They presumed that the barrier asymmetry can be the reason for the shift in the maximum TMR. Feng et al[117] accepted this speculation and described that the barrier asymmetry might arise due to the variations in the degree of film texture between the MgO barrier and the CoFeB layer. Thus according to Feng et al tunnel barrier asymmetry was expected to reduce by annealing at high temperatures. Since in our stacks annealing at high temperatures might permanently change the structure of the top CoFeB/FeGa layer in interface with MgO barrier layer a shift in maximum TMR is still observed at 400°C.

The effect of different annealing temperatures on the TMR ratio of different junction sizes is plotted in Fig. 64a. The directions of external field and the easy axis of the samples during the TMR measurements are shown as an inset drawing. Exchange bias was established for the TMR junctions at 285°C annealing temperature. But the TMR ratio achieved at this annealing temperature was just 10-14%. A constant TMR ratio was observed independent of the junction size at this annealing temperature. An increase of the TMR amplitude with the increasing annealing temperature was reported by many research groups[119,120]. TMR junctions annealed at 350°C show a further increase in the TMR ratio. The highest TMR ratio at this

annealing temperature was 24% and was achieved for the junction size of 2500 μm^2. A large number of defective junctions were observed for samples annealed at 350°C showing large variations in the TMR ratio (Fig. 64b).

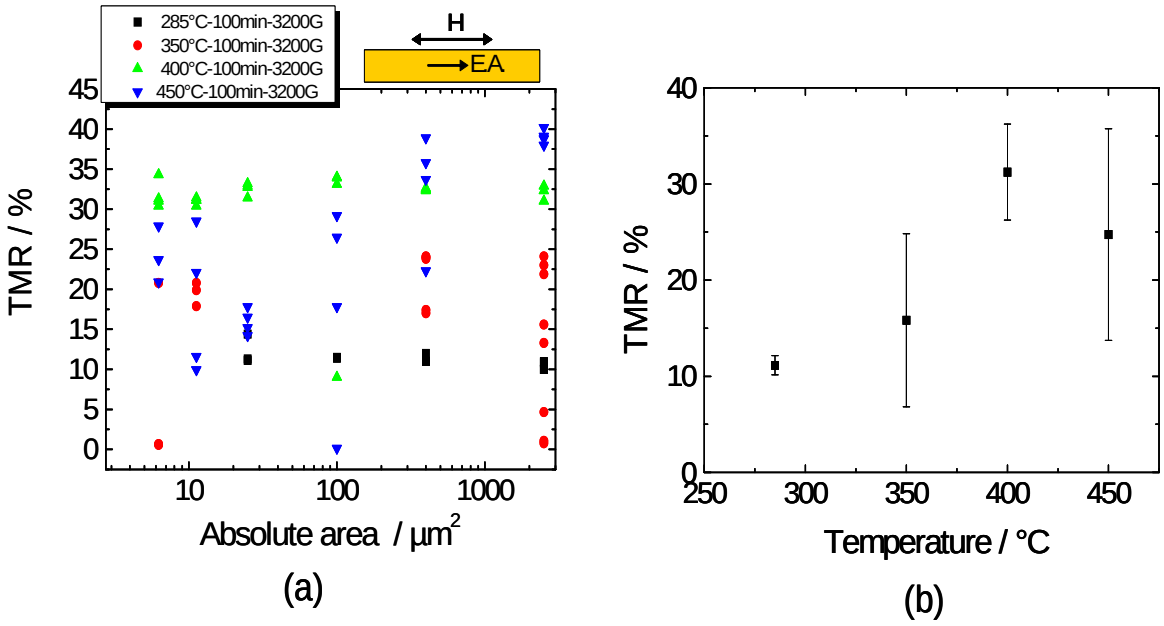

Fig. 64: (a) TMR vs. absolute area measurements of the 2 nm CoFeB interlayer based TMR junctions at different annealed temperatures and (b) average TMR at different annealing temperatures.

Junctions annealed at 400°C show further increase in the TMR ratio. Independent of the junction size TMR ratios between 31±5 % were achieved for this annealing temperature as shown in Fig. 64b. Annealing above 425°C,[14,123,121] resulted in the reduction of the TMR ratio for exchange bias based TMR junctions. Several reasons were put forward to explain the reduction in the TMR ratio. Mn and Ru diffusion into the barrier layer are the most suspected reasons for decrease in the TMR ratio. From Fig. 64 it can be seen that further increase in the annealing temperature to 450°C resulted in the increase of the TMR ratio for some of the junctions above 38 %, while most of the small junctions show low TMR ratio below 30 %. Fig. 64b indicates that at 450 °C the mean TMR however reduces to 25 % with a standard deviation of ±11 %. The TMR effect amplitude achieved for junctions with similar stack configuration (without FeGa sensing layer) were much higher than 100 % at room temperature[9]. The possible reason for the observed low TMR ratio could be an incoherent tunneling because of the

intermixing of CoFeB and FeGa during the sputter deposition or annealing. This also explains the asymmetric nature of the IV- curves measured.

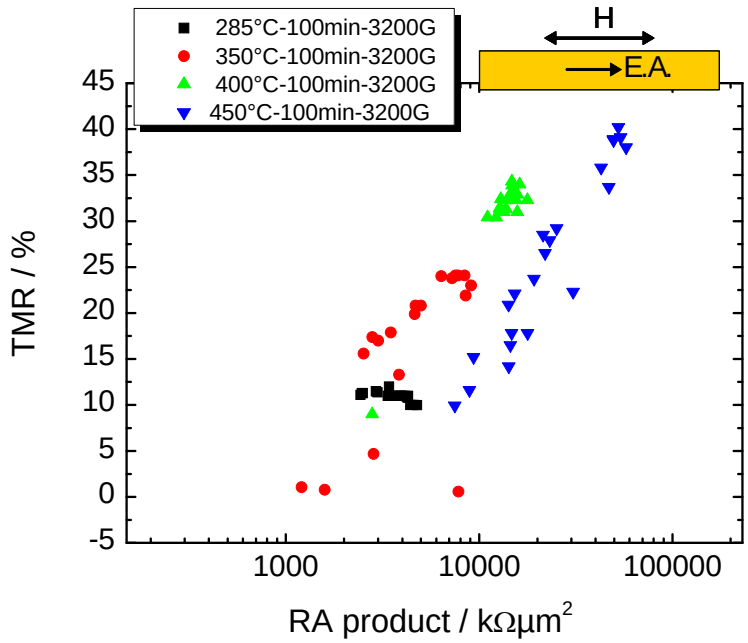

Fig. 65: TMR ratio vs. RA product of the 2 nm CoFeB interlayer based TMR junctions at various annealing temperatures.

The relationship between TMR ratio and the RA product is shown in the Fig. 65. The RA of junctions at 285°C annealing temperature varies from 4±1 MΩμm^2. Junctions annealed at 350°C show an increase in the RA product (5±3 MΩμm^2) and at 400°C annealing temperature the RA of the junctions were 14±3 MΩμm^2. For this annealing temperature the variation in the TMR ratio was also small (31±5 %). High RA product of the junctions were also reported by Matsumoto et al[122]. There is a clear tendency of increase in the RA product of the junctions with increasing annealing temperature. One possible explanation for this behavior is the presence of an additional oxide layer in series between CoFeB and FeGa thin film causing an increase in the RA product. This can be easily fixed by sputter etching a few nanometers of CoFeB film before the deposition of FeGa sense layer. To find out the maximum annealing temperature the junctions were annealed at 450°C. At this annealing temperature the junctions shows a large variation of the TMR ratio (10-40 %) as well as the RA product (27±18 MΩμm^2). This could be because at annealing temperatures as high as 450°C it is stated in many literatures that there is a Mn diffusion in addition to it the presence of an oxide film can further increase the resistance.

The average TMR ratio also increases with increasing annealing temperature (shown in Fig. 64b). Magnetoresistance measurements of samples annealed 400°C show only a very small variation of TMR ratio (31±5 %) for all junction sizes. Whereas the junctions annealed at 350 °C and 450 °C show large variations in the TMR ratio. Therefore the optimum annealing temperature for achieving highly reliable TMR ratio for these TMR stacks is 400 °C. In general the RA product of all the junctions at all annealing temperatures are in the order of several $M\Omega\mu m^2$, which is very high for applications based on TMR effect. For applications of TMR junctions as pressure sensor[9,8] the range of the RA product was between a few $\Omega\mu m^2$ to 400 $K\Omega\mu m^2$.

During the two point MR measurements a variation in the resistance was noticed depending on the position of the ground electrodes (ground 1 or ground 2 shown in Fig. 34 of section 3.3.4) contacted by the precision needle. In order to calculate the resistance of the junctions independent of the ground electrodes a simple formula was used:

$$R_{cal} = \left(R_{measured}\right) - \left(\frac{(D_{Jn}(m) * R_{ground-ground}(\Omega))}{D_{total}(m)}\right) \tag{23}$$

In equation (23), $R_{ground\text{-}ground}$ is the resistance measured when both needles were placed on the ground electrodes and 10 mV constant bias voltage was applied. D_{Jn} is the distance from the selected ground electrode to a particular TMR junction and D_{total} is the total distance between both ground electrodes. This distance was known from the design parameters as 2600 μm.

$$TMR_{cal}Ratio = \frac{(R_{max}(\Omega) - R_{min}(\Omega))}{R_{cal}(\Omega)} * 100 \tag{24}$$

$$RA_{cal} = (R_{min\,cal}(\Omega) * \text{Area of the junction } (\mu m^2) \tag{25}$$

From equations (24) and (25) it was possible to calculate the TMR ratio and the RA product independent of the resistance from the ground electrodes. Fig. 66 is the plot showing the calculated TMR ratio as a function of the calculated RA product. It can be noticed that for most of the junctions there is no pronounced change in the values of the TMR ratio and the RA product. Only a very few junctions annealed at 350°C show a very small variation of

the RA product. Therefore the effect of the resistance from the ground electrode can be neglected for this configuration of TMR junctions.

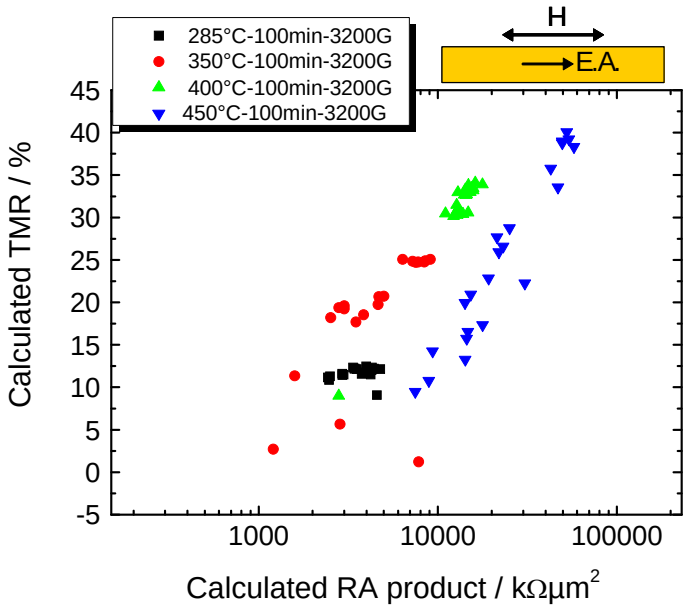

Fig. 66: Calculated TMR ratio vs. calculated RA product of the 2 nm CoFeB interlayer based TMR junctions at various annealed temperatures.

From these experiments it can be concluded that the high RA product of the 2 nm CoFeB/FeGa based TMR junctions is due to the presence of an oxide layer in series between the CoFeB (2 nm) and FeGa. Presence of oxide layer and intermixing of CoFeB/FeGa at high annealing temperatures reduces the overall TMR ratio to about 30%. As observed in the literature until 400°C the TMR increases with increasing annealing temperature and at 450°C there is a reduction of the TMR ratio. This reduction in the TMR ratio is due to the Mn, Ru and Ga diffusion.

4.3.2 Strain sensitivity of exchange bias based TMR junctions with 2nm CoFeB interlayer

The setup for the strain characterization of TMR junctions is discussed in section 3.3.4. Since the thick and thin FeGa electrodes based TMR junctions show no stable anti-parallel configuration, the measurements were concentrated on the exchange bias based TMR junctions which show a stable anti-parallel configuration. A useful measure of the strain sensitivity of a TMR junction is the gauge factor which is defined as the relative change in the resistance (ΔR) of the sample to the change in the applied strain ($\Delta\varepsilon$):

$$\text{Gauge Factor (GF)} = \frac{(\Delta R/R_{min})}{\Delta\varepsilon} \qquad (26)$$

The stack configuration of these exchange biased junctions is shown in section 4.3.1. The measurements were performed by applying a 10 mV constant bias voltage and by increasing the displacement of the strain holder on the sample in positive direction (compressive strain) or in the negative direction (tensile strain) and consequently measuring the magnetoresistance curves at various strain states. All strain sensitivity measurements were performed such that the hard axis of the sensing layer (FeGa 20nm and 2nm CoFeB) was perpendicular to the direction of the external magnetic field. The easy axis of the sensing layer was parallel to the external field.

Fig. 67 illustrates the effect of tensile strain on a 400 μm^2 TMR junction. The TMR ratio of the junction was 34%, when no stress was applied. The TMR junctions annealed at 400°C was chosen for the strain measurements as these show uniform TMR ratio independent of the size of the junctions (see Fig. 64 and Fig. 65 of section 4.3.1).

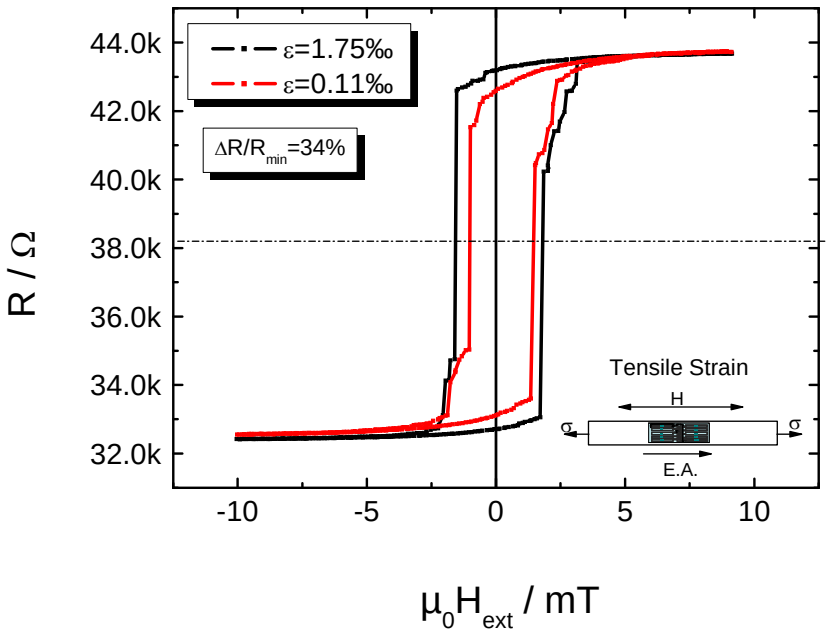

Fig. 67: Magnetoresistance measurements of a 20 µm x 20 µm TMR junction at different strain settings, annealed at 400°C and cooled down in the presence of a magnetic field of 320 mT. A tensile strain was applied to the sample. The direction of the external field and strain during the measurement are shown as an inset diagram.

It can be observed that tensile strain applied to the junction increases the coercive field. Further the squareness of the hysteresis also increases. The increase in the coercive field in this case is from 1.7 mT to 2.2 mT. This shows that the magnetization remains in the easy axis and starts to stabilize with increasing strain. When a tensile strain was applied to a positive magnetostrictive ferromagnetic film the domains in the film stabilize in the direction of the applied strain increasing the coercivity and squareness. Since the 20 nm thick FeGa layer dominates the magnetostrictive response of the two layer system (CoFeB/FeGa) and since CoFeB is also positive magnetostrictive the same behaviour was also observed.

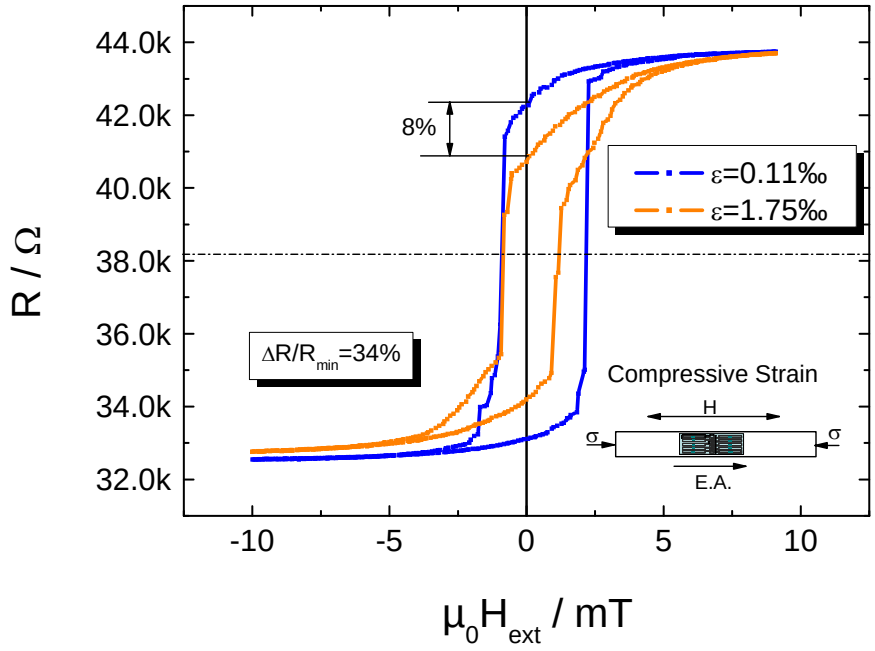

Fig. 68: Magnetoresistance measurements of a 20 µm x 20 µm TMR junction at different strain settings, annealed at 400°C and cooled down in the presence of a magnetic field of 320 mT. Compressive strain was applied to the sample and the magnetoresistance curve was measurement for the TMR junction

The effect of compressive strain measurement on the same TMR junction mentioned above is shown in Fig. 68. The magnetization of the positive magnetostrictive film is expected to rotate away from the easy axis under compressive strain. From Fig. 68 it can be observed that the magnetization direction of the magnetostrictive free layer rotates perpendicular to the easy axis. This rotation stops when the magnetization of the sensing layer reaches the hard axis. The magnetization of sensing layer rotates towards the hard axis because under compressive strain the domains of the FeGa film are

brought to unfavorable energy state and therefore by rotating away from the easy axis state the energy of the domains are lowered. A maximum strain of 1.75‰ changes the magnetization of the sensing layer resulting in 8% reduction of the TMR effect at zero magnetic field. From this reduction the gauge factor can be calculated. A gauge factor of 21 was achieved at zero external field for maximum strain state (1.75‰).

Furthermore compressive strain measurements of 100 μm^2 and 2500 μm^2 TMR junctions annealed at 400 °C and 450 °C are shown below (Fig. 69 and Fig. 70). FeGa is positive magnetostrictive and from the measurements shown in Fig. 67, under tensile strain only stabilization of the easy axis was observed and the maximum strain sensitivity was observed for compressive strain measurements (inverse magnetostriction of 2 nm CoFeB can be neglected as compared to 20 nm FeGa), therefore from these measurements it can be concluded that to characterize the strain sensitivity of these junctions it is sufficient to perform compressive strain measurements.

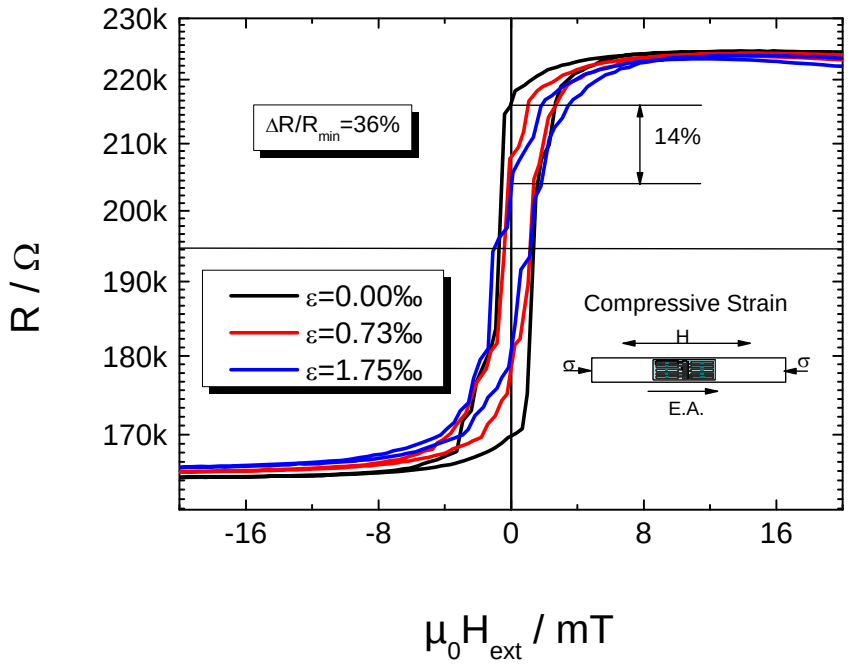

Fig. 69: Magnetoresistance measurements at different strain states of a 100 μm^2 TMR junction annealed at 400°C and cooled down in the presence 320 mT.

The magnetoresistance measurements under compressive strain of a 100 μm^2 TMR junction is shown in Fig. 69. The junction shows 36% TMR ratio.

The coercive field of the junction at unstrained state is 1.5 mT. The hysteresis curve is shifted 0.63 mT towards the negative field, leading to a small assymettry. This shift is due to the exchange bias coupling of the hard magnetic layer which shifts the minor loop of the sensing layer towards the left. Increasing compressive strain results in the reduction of the steepness of the hysteresis. This is because the magnetization of the sensing layer rotates away from the easy axis to reduce the energy of the domains. A maximum strain of 1.75‰ was applied to the junction resulting in about 14% total reduction of TMR ratio at zero magnetic field. The gauge factor was calculated as GF=33.

Fig. 70 is the magnetoresistance measurement of a 2500 μm^2 junction showing a TMR ratio of 40%. The coercive field of unstrained sensing layer is 1.75 mT. An assymetric shift to the right of the hysteresis as mentioned above for Fig. 69 can also be observed for these junctions, the shift value corresponds to 1 mT. Compressively straining the sensing layer leads to the rotation of the magnetization towards the hard axis. A maximum 1.02‰ strain results in 11% reduction of the TMR ratio. The gauge factor corresponding to the maximum strain was 42.

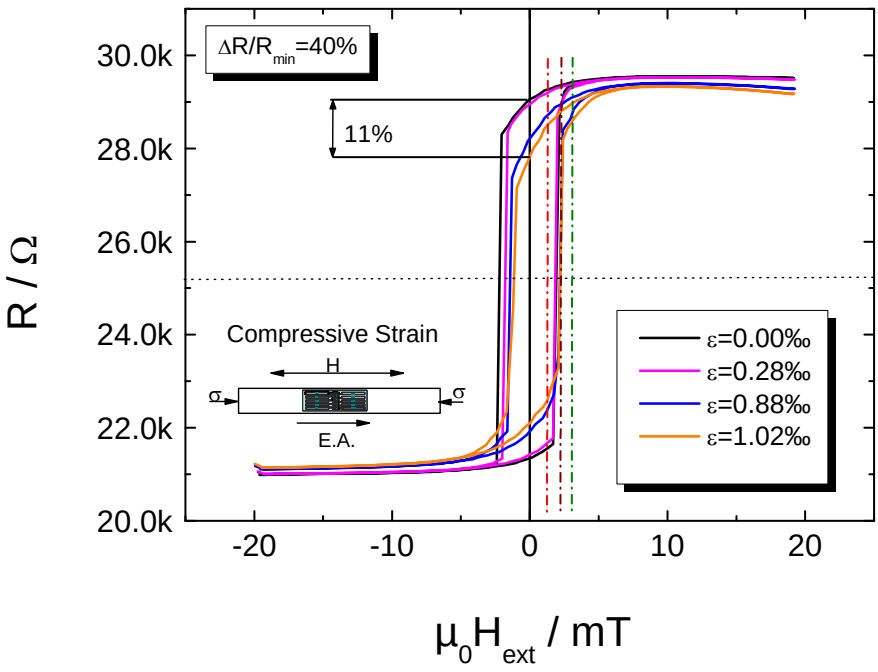

Fig. 70: Magnetoresistance measurements at different strain states of a 2500 μm^2 The junction was annealed at 450°C and cooled down in the presence 320 mT field. The vertical dotted lines drawn on the right side indicate the bias fields at 1 mT, 2 mT and 3 mT used to measure resistance versus strain measurements.

Further the strain versus resistance property of the TMR junction at different bias field was measured. This characterization is important to determine the operating point of the junctions to be used as strain sensor. The sample was strained uniformly until a maximum strain value was reached and the resistance change was recorded. After reaching maximum, the strain was reduced in the same uniform steps back to 0‰.

The strain vs resistance measurements of 2500 μm^2 junction at 1 mT, 2 mT and 3 mT are shown in Fig. 71. The magnetic easy axis was initially (without applying mechanical stress) parallel to the external field. The position of the bias fields in the hysteresis is marked in Fig. 70. In Fig. 70, the red line denotes 1 mT bias field, brown line denotes 2 mT and the green line represents 3 mT respectively. The first two bias fields (1 and 2 mT) are within the hysteresis area of the minor loop and the third bias field (3 mT) is at the interface between the hysteresis and the saturation magnetization of the minor loop.

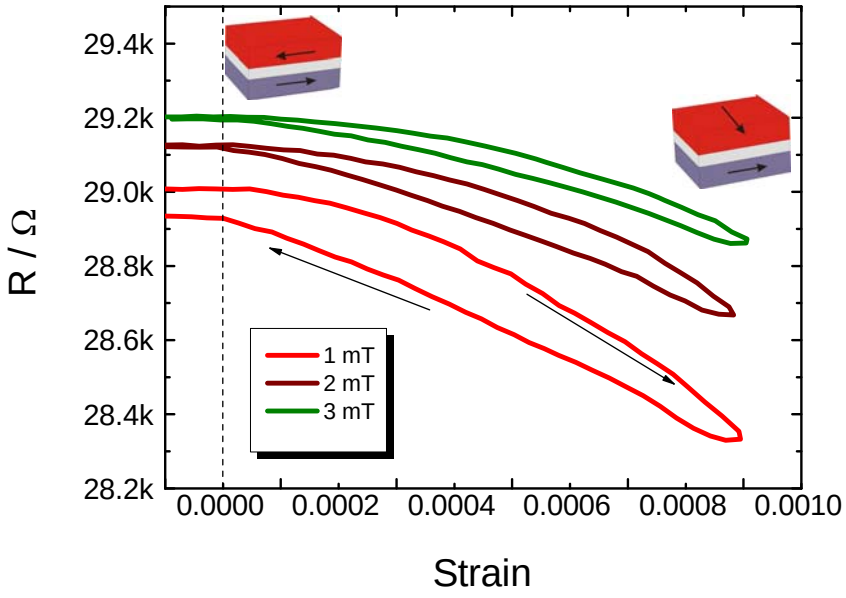

Fig. 71: Resistance-strain measurements of a 50 µm x 50 µm junction. The strain was increased and decreased in steps of 0.11‰. The insets show idealizations of the magnetization configuration approached during the strain loop.

The sample was saturated at the positive saturation field of the sensing layer first after which a bias field of 1 mT was applied to the junction. At 1 mT bias field as shown in Fig. 71, the junction shows high resistance (29 kΩ) at the beginning of the strain resistance measurement. This high resistance is because the junction is approaching the anti-parallel magnetization. The bias field of 1 mT lies inside the hysteresis regime; therefore the change in the resistance (i.e. the starting point and the end point do not coincide) was due to the sudden switching of the domains. When the strain was increased the resistance decreases. At maximum strain ε=1.02‰ the resistance reaches 28.3 kΩ. At this maximum strain the sample is still inside the elastic limit. Therefore a further increase in strain is possible. The substrate of other samples broke after the strain reached ε=1.02‰. Therefore in order not to break the samples, during the experiment the maximum strain was chosen as 1.02‰. The strain was reduced back to zero in uniform steps (0.11‰).

When the strain was reduced the resistance reduces and reaches 28.9 kΩ at zero strain. A hysteresis was observed when tracing the increasing and decreasing strain directions. This hysteresis appears because of the change in the magnetic properties of domains which cannot be reversed back during the reduction of the strain. The value of resistance does not reach back to its original starting resistance by reducing the strain. One of the possible reasons could be because of some irreversible domains.

The brown and the green curves show the resistance at varying strain when the bias fields are 2 mT and 3 mT. These bias fields as shown in Fig. 70 correspond to the area outside the minor loop of the hysteresis. At B=1 mT and at zero strain the junction is approaching the anti-parallel state. The width of the hysteresis decreases for 2 mT bias field and decreases further more for 3 mT. Therefore a less hysteretic behaviour is expected for the bias field outside the hysteresis. But the gauge factor is small as compared to the measurement inside the hysteresis loop. It can be noted that the change in the resistance with the applied strain starts not at zero strain but at 0.11‰. Therefore the point of contact between the pusher block and the cantilever TMR junction is shifted as shown by the dotted lines in the Fig. 71. Under maximum strain the measured resistance of the junctions does not reach the middle of the hysteresis shown by the dotted lines in Fig. 70. Therefore the magnetization state shown as inset figure in Fig. 71 is clearly not reached.

4.3.3 Exchange bias based TMR junctions with 4 nm CoFeB interlayer

Two wafers with the following configuration were prepared and analyzed:

TaN 5 nm / Ta 5 nm / PtMn 25 nm / CoFe 2.5 nm / Ru 0.8 nm /
$CoFe_{40}B_{20}$ 4nm / Mg 1.5 nm / MgO 1.5 nm /
$CoFe_{40}B_{20}$ 4 nm / FeGa 20 nm / Ta 5 nm / Ru 10 nm

Initially 6 nm of CoFeB was deposited on top of MgO barrier layer by Siemens AG, 2 nm out of 6 nm was etched by Ar ions in the etch chamber of Ardenne cluster deposition tool followed by the deposition of 20 nm FeGa, Tantalum and Ruthenium top electrodes without break of vacuum. The advantage of sputter deposition without break of vacuum is that the TMR stack will be free from the dust and contaminants from the atmosphere. It would further be possible to avoid or remove the native oxide on CoFeB layer. The junctions were fabricated by two steps of lithography. In the first lithography the mask from Fig. 22b (shown in section 3.1.4) was used to pattern the TMR structures on a continuous ground electrode. The samples were etched by IBE through the MgO barrier layer. SiO_2 was sputter deposited to serve as the passivation layer. The second step of lithography involves the fabrication of contact pads. The wafer was diced into cantilevers and was annealed at 285°C, 325°C, 375°C and 400°C for 100 minutes at 320 mT to study the effect of different annealing temperatures.

Fig. 72a is an exemplary magnetoresistance measurement (minor loop) of a 10 µm x 10 µm junction. The junction showed 62% TMR ratio. The resistance area product of the junction was 61 $k\Omega\mu m^2$. A stable anti-parallel magnetization state can be observed because of annealing the junction at 350°C and at 320 mT field. The major loop (Fig. 72b) shows the parallel resistance state at large applied fields (~ 400 mT). This is because at higher fields the magnetization of the pinned CoFeB layer also switches in the direction of the field resulting in a parallel configuration of magnetization.

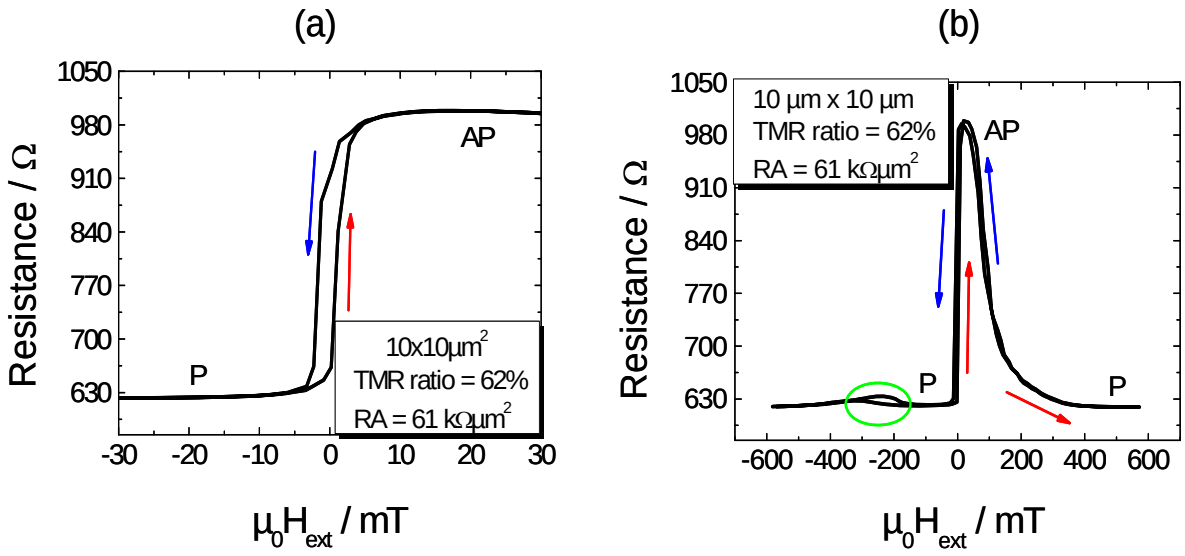

Fig. 72: (a) Minor loop of a 10 μm x 10 μm junction annealed at 350°C for 100 minutes at 320 mT field, (b) Major loop of the same junction. P and AP denote the parallel and anti-parallel configuration of magnetization of sensing and the reference layer. The red arrows denote the forward looping direction of the field and the blue arrows denotes the reverse looping direction of the applied external field.

Fig. 73a is an I-V curve measurement of the same junction. The measurements were performed at ±60 mT field and by varying the voltage between ±300 mV. The curve at –60 mT shows a pronounced ohmic behaviour as compared to the junction with 2 nm CoFeB, this corresponds to a large flow of current in the junction (±500 μA). At +60 mT field the I-V curve shows a cubic behaviour which represent tunneling.

From I-V curves the normalized TMR ratio was calculated and plotted as a function of the bias voltage in Fig. 73b. At higher bias voltages the sample shows low TMR ratios and at smaller bias voltages maximum TMR ratio was achieved. Only a small asymmetry of the TMR ratio was observed versus bias voltage in Fig. 73b as compared to a large asymmetry observed for 3 nm CoFeB based TMR junctions shown in Fig. 63b. The voltage when the TMR is reduced to half on the left side is -189 mV and on the right side it is +162 mV. This suggests that TMR ratio decreases quicker on the right side as compared to the left side. This small bias asymmetry of 27 mV reflects the different states of electronic configuration at the CoFeB/MgO interface during annealing. It can further be observed that the maximum of the TMR curve is close to the zero bias voltage. Therefore the junctions annealed at 350°C approaches coherent tunneling.

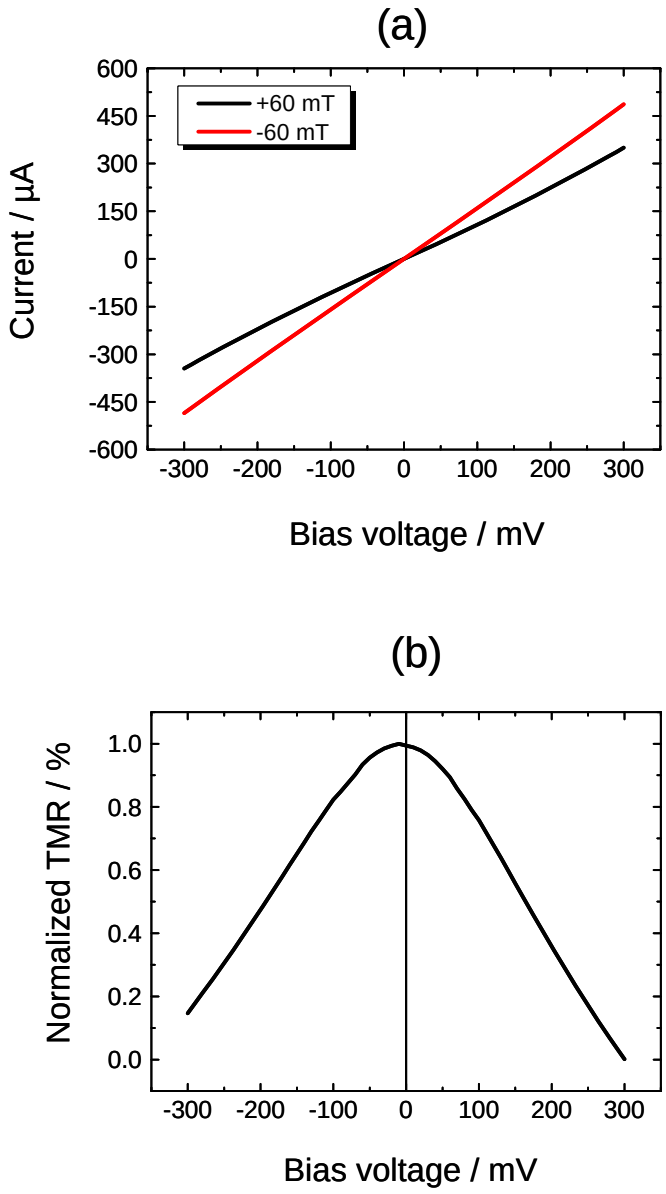

Fig. 73: (a) I-V Curve of the 10 µm x 10 µm junction measured at positive and negative saturation field of the soft magnetic FeGa layer and (b) Normalized TMR ratio calculated from the I-V curve versus supplied bias voltage.

Fig. 74a shows the TMR ratio versus absolute area of the 4 nm CoFeB interlayer based TMR junctions at different annealing temperatures. The direction of easy axis was parallel to the external magnetic field during the measurement (shown as inset in Fig. 74a). From the figure it can be concluded that maximum TMR ratios from 60% to 64% were achieved at annealing temperatures from 325°C to 375°C. Further increase of annealing temperature to 400°C results in the reduction of TMR ratio. Larger junction

sizes show reduced TMR ratio as compared to small junctions at all annealing temperatures. In comparison to the 2 nm CoFeB interlayer based TMR configuration, there was an overall increase in the maximum TMR ratio from 40% to 64%. The mean TMR ratio increases with increasing annealing temperature and reaches maximum at 325°C. Further increase in the annealing temperatures reduces the mean TMR ratio as shown in Fig. 74b. It was shown by Feng et al[123] that annealing at 375°C and above reduced the TMR ratio. They stated that this was due to the break down of exchange bias in a MnIr based double magnetic tunnel junctions. The 4 nm CoFeB interlayer based TMR junctions were not annealed above 400°C as it was shown in the previous sub-section 4.3.1 that annealing at 400°C resulted in the Mn, Ru and Ga diffusion.

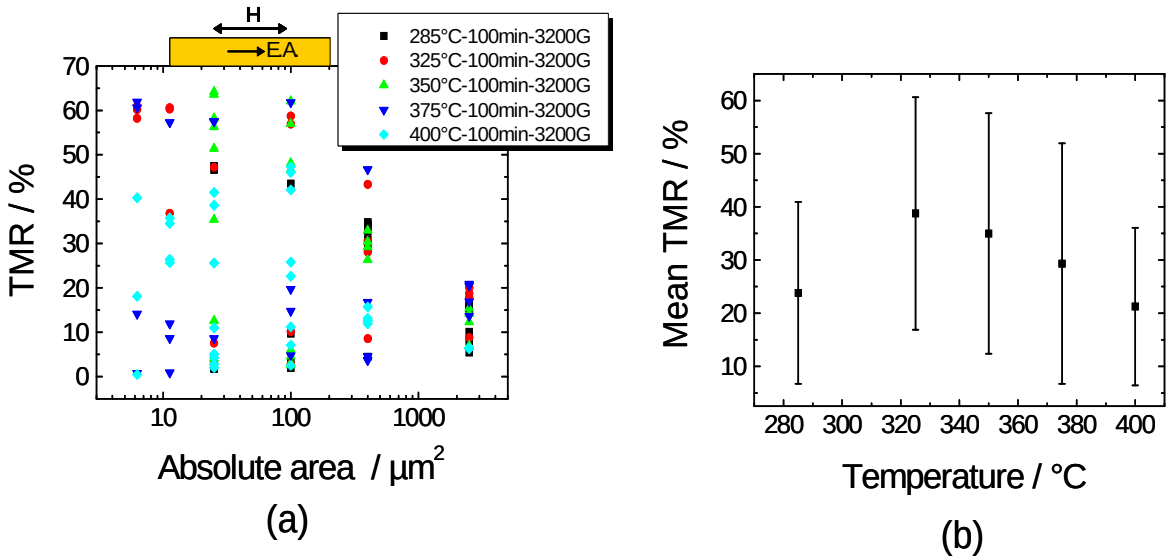

Fig. 74: (a) TMR vs. absolute area of 4 nm CoFeB interlayer based TMR junctions at different annealing temperatures and (b) Mean TMR ratio of all the junctions at various annealing temperatures.

The influence of the annealing temperature on the TMR ratio as a function of the RA product of the junctions is shown in Fig. 75. RA product of junctions which show TMR ratios above 50% are in the range of 10 kΩµm^2 to 130 kΩµm^2. Because the oxide layer was removed by sputter etching there is a clear reduction of the RA product as compared to the 2 nm CoFeB based TMR junctions. Removal of the oxide layer also increases the TMR ratio.

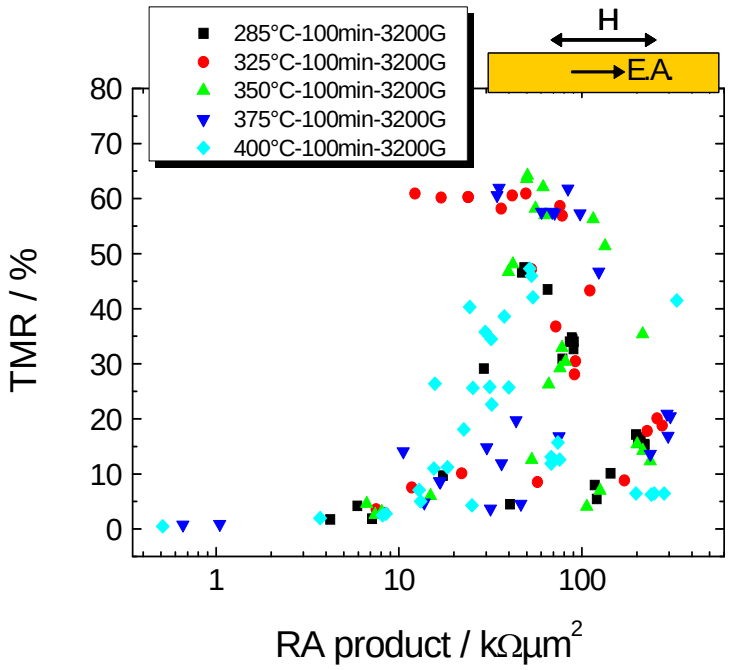

Fig. 75: TMR vs. RA product of 4 nm CoFeB interlayer based TMR junctions at different annealing temperatures

It can be noted from Fig. 75 that junctions annealed at 375 °C and 400 °C show a tendency of increase in the RA with increasing TMR ratio. There is also a very large distribution of junctions showing small TMR ratio for all junction sizes and at all annealing temperatures. A possible explanation could be because the re-deposition of etched elements on the sides of the TMR junctions during IBE, resulting in additional conduction paths. In this case there would a correlation between low RA and low TMR, but there is no such correlation. Therefore other reasons for the reduction of TMR are introduction of impurities and defects. A non-uniform argon ion sputter etching over the wafer before the sputter deposition of FeGa could result in the introduction of such defects and impurities. Annealing of these junctions was performed after the sputter deposition of FeGa sensing layer. There is also a high possibility of Ga diffusion (section 4.2) at high annealing temperatures over a prolonged period (100 minutes).

From the Fig. 76, the calculated maximum TMR ratio was 66% for samples annealed at 350°C and the RA product of the junctions showing above 50% TMR ratio are in the range of 10 kΩμm^2 to 106 kΩμm^2. A small increase in the TMR ratios is observed because the calculated RA product (after

removing the resistance of ground electrode) of all the junctions at all annealing temperatures is reduced.

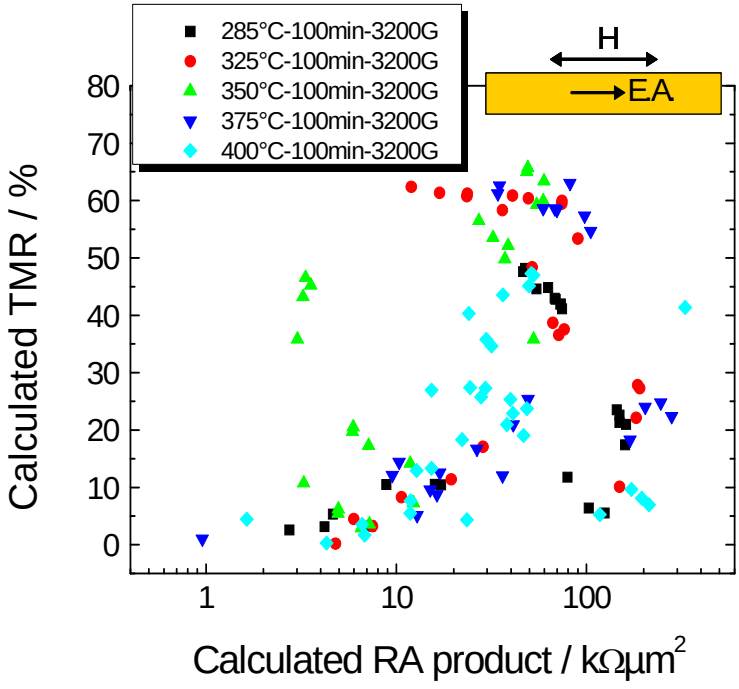

Fig. 76: Calculated TMR vs. Calculated RA product of 4 nm CoFeB interlayer based TMR junctions at different annealing temperatures

In comparison with 2 nm CoFeB interlayer based exchange biased junctions an overall increase in TMR ratio was observed. The RA of these junctions vary from a few $k\Omega\mu m^2$ to almost 350 $k\Omega\mu m^2$ as compared to the 2 nm CoFeB based TMR junctions which showed RA in the $M\Omega\mu m^2$ range. Therefore it is shown that the high resistance of the junctions which might arise from the oxide interlayer in the previous TMR configuration can be successfully removed by sputter etching and sputter depositing FeGa without breaking the vacuum. The RA product of the junctions are in the range of few hundreds of $k\Omega\mu m^2$ which is in the good co-relation with the RA product of the state of the art strain sensor[9] based on a similar TMR junction configuration.

To understand further if the defective TMR junctions are due to the Ga diffusion another wafer with the following configuration was prepared:

TaN 5 nm / Ta 5 nm / PtMn 25 nm / CoFe 2.5 nm / Ru 0.8 nm / $CoFe_{40}B_{20}$ 4nm / Mg 1.5 nm / MgO 1.5 nm / $CoFe_{40}B_{20}$ 6 nm

The wafer was diced and each piece was annealed at different temperatures. Exchange bias was established only for the samples annealed at 285°C, 325°C and 400°C annealing temperatures. After annealing at various annealing temperatures 2 nm of CoFeB was etched by Ar ions out of 6 nm CoFeB on top of MgO barrier layer. Further a 20 nm FeGa sense layer, Ta and Ru top electrodes were sputter deposited without the break of vacuum.

A minor loop of a 2.5 µm x 2.5 µm junction annealed at 400°C is shown in Fig. 77a. The hysteresis of the soft magnetic layer shows a stepwise increase in the resistance from the parallel state to the anti-parallel state because of the domain formation. The junction shows a TMR ratio of 53%. The RA of this junction was 41 kΩµm^2. The major loop (Fig. 77b) shows that at ±400 mT the hard magnetic layer (pinned CoFeB) also switches the magnetization in the direction of the applied field resulting in parallel resistance state.

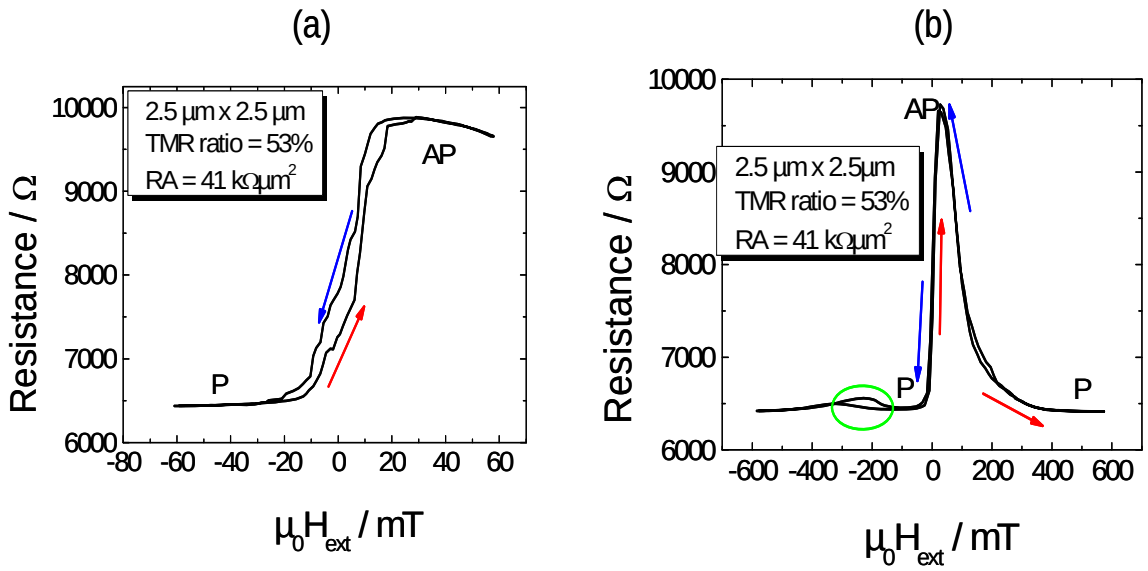

Fig. 77: (a) Minor loop of a 2.5 µm x 2.5 µm junction annealed at 400°C for 100 minutes at 320 mT field, (b) Major loop of the same junction. P and AP denote the parallel and anti-parallel configuration of magnetization of sensing and reference layer. The red arrows denote the field direction during the forward looping and the blue arrows denotes the reverse looping of the applied external field

Fig. 78a is the I-V measurement curves of a 2.5 µm x 2.5 µm junction. At +60 mT field a non-linear tunneling behaviour can be clearly observed. At -60 mT field essentially an ohmic behaviour similar to the 4 nm CoFeB based junctions can be noticed. No shift of the maximum TMR at zero bias voltage is observed. This means that annealing these junctions at 400°C results in almost similar CoFeB/MgO interfaces on both sides of the junction.

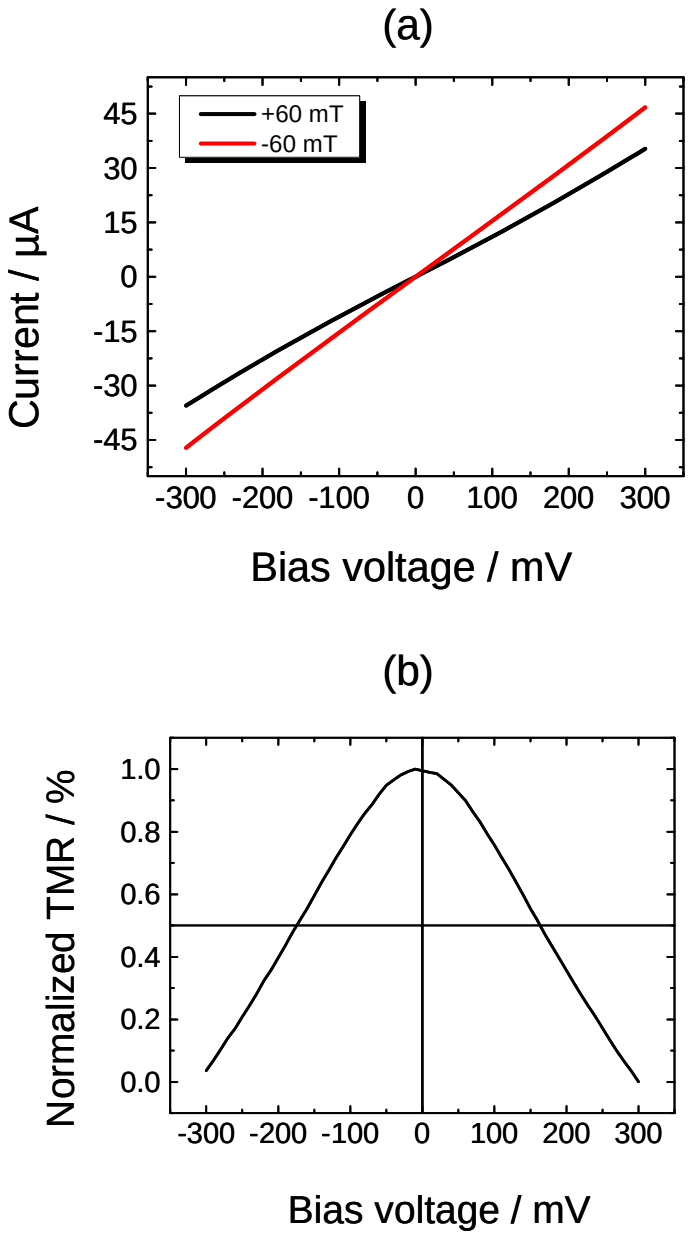

Fig. 78: (a) I-V curve of a 2.5 µm x 2.5 µm junction measured at positive and negative saturation fields of the soft magnetic FeGa layer and (b) Normalized TMR ratio from the I-V curve versus supplied voltage.

It was shown by Feng et al[117] that with increasing annealing temperature the shift of the maximum TMR ratio to the bias voltage is reduced due to the improved film texture between CoFeB layers and the MgO barrier layer. A very small asymmetry can be observed. The bias voltages when TMR ratio is reduced to half are -174 mV and +163 mV. Therefore the difference between the negative and positive bias voltage is just 11 mV. This is much less as compared to the 4 nm CoFeB based TMR junctions. From the I-V curves there is no indication that there is Ga diffusion into the barrier layer.

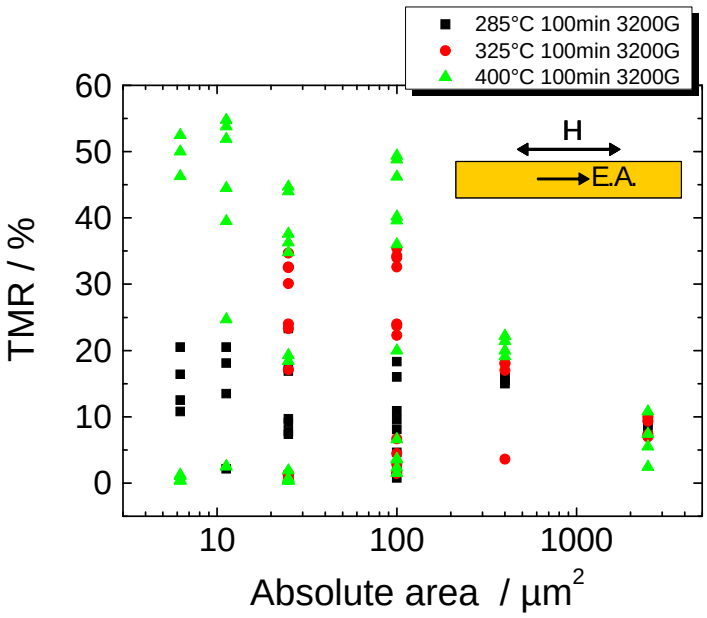

Fig. 79: TMR vs. absolute area of 4 nm CoFeB based TMR junctions at different annealing temperatures (annealing was performed before the deposition of FeGa sensing layer).

Magnetoresistance measurements were performed at different annealing temperatures and for various junction sizes. Shown in Fig. 79, is the TMR ratio dependence on the absolute area of the junctions at various annealing temperatures. Independent of annealing temperature, junctions larger than 100 μm^2 show decrease in the TMR ratio. When compared with the previous (4 nm CoFeB interlayer based junction) configuration no junctions annealed at 325 °C show TMR ratio higher than 40%. Junctions annealed at 400°C achieve TMR ratio as high as 55%. The junctions were not annealed at temperatures higher than 400 °C because the 2 nm CoFeB based TMR junction annealed at 450 °C showed a large variation in the TMR ratio due

to Mn, Ru and Ga diffusion. Therefore this temperature was not included for the experiments. Junctions smaller than 100 μm^2 show high TMR ratios. Highly defective TMR junctions can be observed at all annealing temperatures and at all junction sizes. The reason could be because of the defects originating from the lithography, as it was not possible to achieve vacuum contact between the diced pieces of the wafer and the mask during lithography resulting in defective junctions. Another possibility is the non uniform argon ion etch of the TMR junctions before deposition of FeGa and top electrodes resulting in large number of defective junctions.

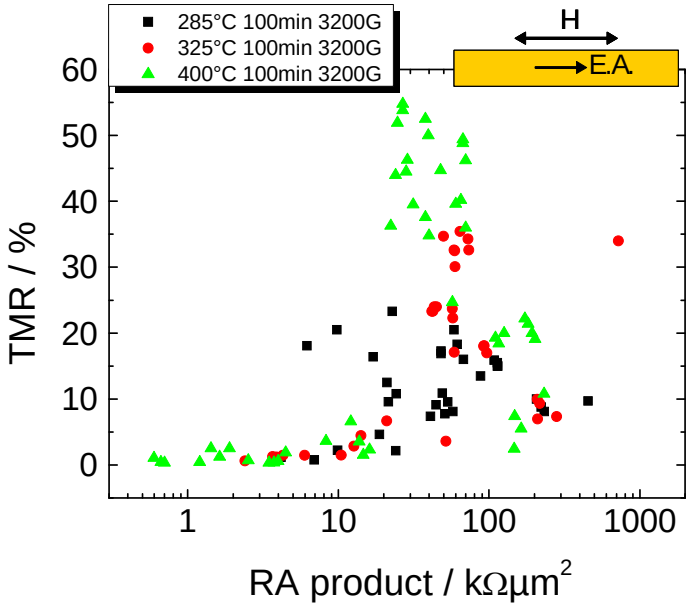

Fig. 80: TMR vs. RA product of 4 nm CoFeB based TMR junctions at different annealing temperatures (annealing was performed before the deposition of FeGa sensing layer)

The RA product of the junctions as a function of TMR ratio is plotted in Fig. 80. Junctions with high TMR ratio have a RA product in the range of 70 $k\Omega\mu m^2$ to 80 $k\Omega\mu m^2$. Overall there is a very large distribution of junctions at all annealing temperatures showing RA product less than 10 $k\Omega\mu m^2$. The results are comparable to the previous configuration. Further pre-annealing of the TMR junction before deposition of the FeGa increases the coherent tunneling process as shown from the I-V curves in Fig. 78b. Therefore the highly defective junctions are not because of the Ga diffusion during annealing. Exchange biasing of the hard magnetic layer also worked. It can be concluded that annealing of the 4 nm CoFeB based TMR stacks did not contribute to the fluctuation in the TMR ratio and RA product of the junctions. Therefore either lithography which includes the Ion beam etching

or the Ar etch of the wafer before sputter deposition of FeGa are the main reasons for highly defective TMR junctions.

4.3.4 Strain sensitivity of exchange biased TMR junctions with 4nm CoFeB interlayer

The stack configuration of the junctions can be referred under section 4.3.3. The strain sensitivity measurements were performed by placing the junction such that the magnetic bias field applied during the strain measurements was perpendicular to the hard axis of the sensing layer during the measurements.

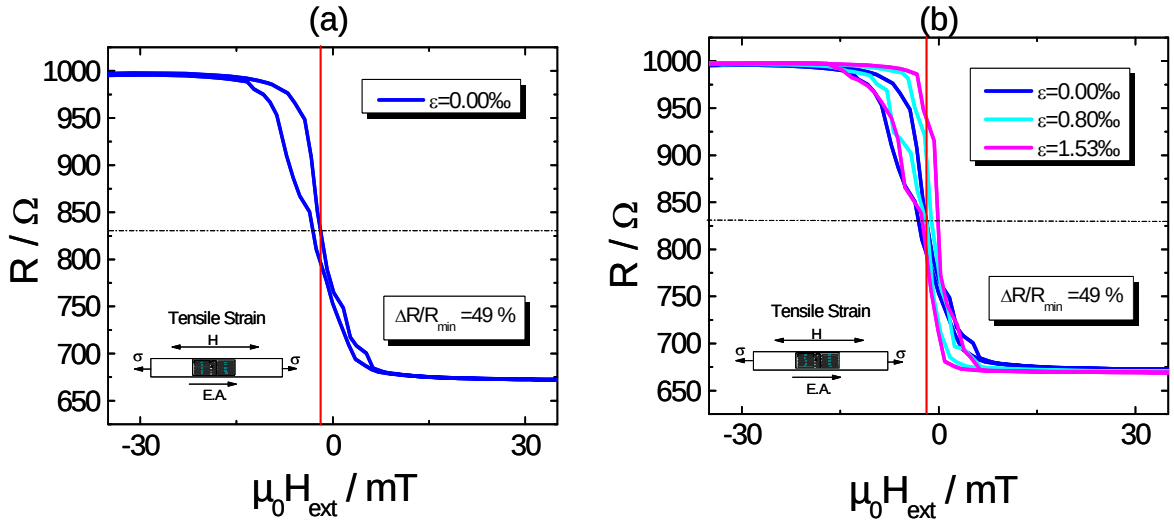

Fig. 81: (a) Magnetoresistance measurement of a 100 μm^2 unstrained TMR junction annealed at 400°C and cooled down in the presence 320 mT; (b) Magnetoresistance measurements of the same TMR junction when tensile strain was applied

The effect of tensile strain on a 100 μm^2 junction is shown in the Fig. 81b. Fig. 81a shows the minor loop of the same junction when no strain was applied. Under tensile strain the slope of the hysteresis becomes steeper. The coercive field of the hysteresis also increases with increasing tensile strain. As the sensing layer is positively magnetostrictive, tensile strain induces a stabilization of the easy axis resulting in an increase in the coercive field of the minor loop. This behavior is similar to the 2 nm CoFeB based TMR junctions configuration (4.3.2).

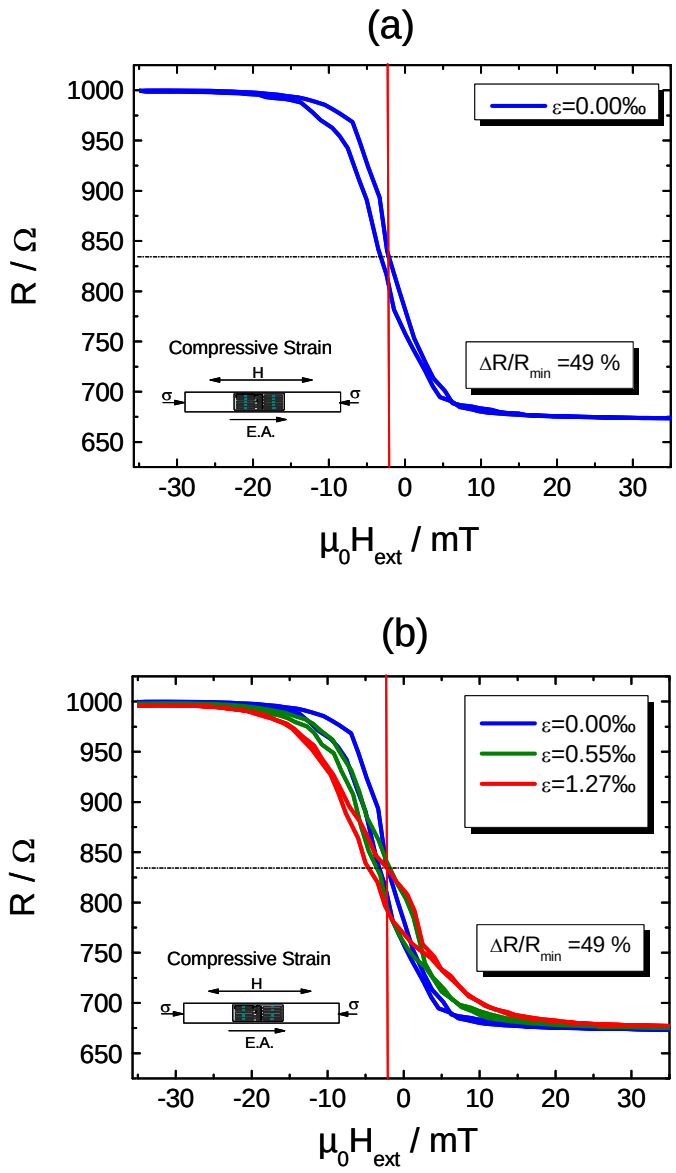

Fig. 82: (a) Magnetoresistance measurement of a 100 μm^2 unstrained TMR junction annealed at 400°C; (b) Magnetoresistance measurements of the same TMR junction at compressive strain.

Fig. 82a is the minor loop of an unstrained 100 μm^2 TMR junction. The TMR effect of 49% was detected for these junctions. The center of the minor loop was shifted towards the left by 2.2 mT (shown by the red line in Fig. 82). This asymmetric shift of the minor loop with respect to zero field is due to the ferromagnetic exchange coupling between the CoFeB/FeGa sense layer and the anti-ferromagnet. More information about exchange bias coupling is discussed in section 2.5.

Fig. 82b shows the effect of compressive strain on the 100 µm^2 junction. It can be observed that the hysteresis curve tends to become flat with increasing strain. This behavior is expected as the FeGa/CoFeB sense layer is positive magnetostrictive. Fig. 82b shows an increase in the width of the hysteresis. A comparison of the curves at zero strain position for compressive and tensile strain measurements (Fig. 81a and Fig. 82a) show that the switching behaviour varies for each time. This could be caused due to the interplay of domains and junction's edge roughness[124].

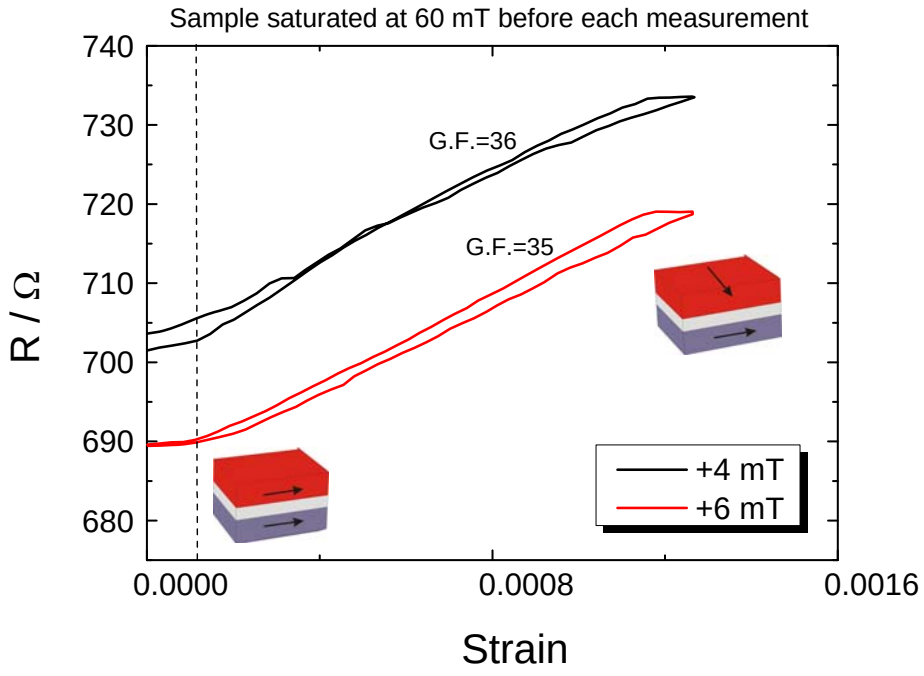

Fig. 83: Strain vs. resistance measurements at 4 mT and 6 mT bias fields. The insets show idealizations of the magnetization configuration approached during the strain loop.

The effects of strain at positive bias fields are shown in Fig. 83. Both 4 mT and 6 mT bias fields are in the transition area between the hysteresis and saturation magnetization field (Fig. 82a). The resistance at the beginning of the forward strain was 690 Ω and 705 Ω for 4 mT and 6 mT respectively. This resistance corresponds to an almost parallel configuration between the reference and sensing layer as shown in the Fig. 82. Increasing the strain to ε=1.27‰ (maximum), an increase in the resistance was observed. The resistance at maximum strain for 4 mT was 735 Ω and 6 mT was 725 Ω. It can further be observed that the sample starts to experience the strain and the change in the resistance a few displacements (0.11‰) after starting the experiment. This is because it was not possible to observe the exact point of

contact physically (by eyes) due to the closeness of the pusher block and the sample. The maximum strain achieved during this measurement was 1.16‰ . A further increase in the strain resulted in the permanent damage of the sample. An increase in the bias field (4 mT to 6 mT) decreases the resistance at zero strain. A maximum gauge factor of 36 was calculated at 4 mT bias field.

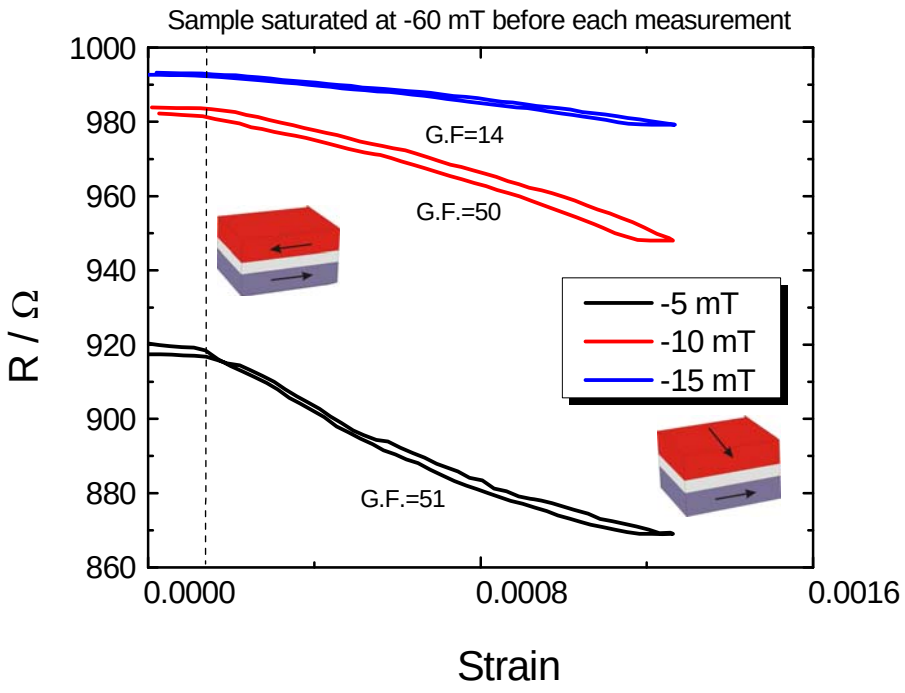

Fig. 84: Strain vs resistance measurements at -5 mT, -10 mT and -15 mT bias fields. The insets show idealizations of the magnetization configuration approached during the strain loop.

The strain versus resistance measurements when a negative bias field was applied is shown in Fig. 84. Bias fields -5 mT, -10 mT and -15 mT were chosen to check the effect. The bias field -5 mT was inside the hysteresis of the minor loop and the other two bias fields are at the transition area between the hysteresis and saturation field (shown in Fig. 82). The resistances at zero strain for all three bias fields approach the anti-parallel configuration of magnetization (920 Ω, 950 Ω and 990 Ω). Increase in strain decreases the resistance until a maximum strain was reached. At the maximum strain state the sample was in intermediate resistance state as shown in Fig. 84. In accordance with Fig. 82b an increase in bias field results in an increase in the resistance at zero strain. For smaller bias fields the slope was steeper as compared to the large bias fields. But at large bias

field the sample showed small hysteresis, this results in a more linear curve and a linear measurement range.

When strain was reversed the resistance increases back and reaches the original resistance at zero strain. At -5 mT bias field, reverse strain reaches a slightly high resistance (920 Ω) than the forward resistance state. This could be because of some irreversible domains that were rotated during the forward strain. A maximum gauge factor of 51 was achieved at -5 mT bias field. The above mentioned gauge factors are higher than the commercially available metallic strain sensors, whose gauge factor is in the range of 2-5[125]. The gauge factor of the FeGa and CoFeB interlayer based TMR junctions lies between the piezoresistive semiconductor based strain gauges having gauge factor from 40-150[125,126,127]. The state of the art strain gauges based on magnetic tunnel junctions show gauge factor of 840[9]. Similar strain gauges based on TMR effect show gauge factor of the order of 300 to 600[11] and the gauge factors measured during this work are much smaller than the above mentioned values. Nevertheless the FeGa and CoFeB based TMR junctions can be used for the strain measurement where moderate strain sensitivity is sufficient.

5 Summary and outlook

This dissertation describes the fabrication and characterization of FeGa thin films to be used in the TMR junctions. Different configurations of TMR junctions were prepared and discussed. Special interest was given to investigate the strain sensitivity of TMR junctions.

The FeGa thin films were sputter deposited by magnetron deposition method. An increased sputter deposition rate was observed for FeGa thin films deposited in the presence of a forming field. The resultant film thickness shows an inverted parabolic distribution and the maximum is achieved at the center of the substrate holder.

The XRD measurements show disordered A2 bcc structure up to a sputter power of 300 W. An $L1_2$ phase was observed for further increase in the sputter power (350 W and above). FeGa thin film sputter deposited at 200 W was analyzed by a three dimensional area detector and found out that 90 nm film shows highly oriented (200) crystallographic growth direction. A 10 nm thin film shows only a very small degree of orientation and at 800 nm film thickness polycrystalline films were observed.

The magnetic characterization of FeGa thin films were performed by MOKE and magnetostriction measurements. MOKE measurements performed on FeGa films show that the films are strain sensitive in a deposition power range of 20 W to 500 W. The coercive field of FeGa film reduces from 5.9 mT to 3.7 mT when the sputter power was reduced. This suggests a soft magnetic behaviour of FeGa film with decreasing sputter power. The magnetostriction measurements of FeGa films showed saturation magnetostriction between $80*10^{-6}$ to $110*10^{-6}$. The Gallium content of these films were in the range of 17.5±0.5 to 19.5±0.5 at%.

The first configuration of the TMR junctions were based on the thick and thin FeGa electrodes. The junctions were sputter deposited on MgO (100) oriented substrates. A sputter power of 200 W was chosen to sputter FeGa film for the TMR stacks, as this sputter power shows highly oriented (200) crystallographic growth of FeGa on MgO substrate. The as deposited TMR junctions show maximum 9% TMR. It was expected that annealing of these junctions might result in further increase of the TMR ratio. But annealing resulted in a total reduction of the TMR ratio. The reason for this decrease in

the TMR ratio was analyzed to be due to the parallel spin independent current paths. TEM experiment was performed on the as deposited and samples annealed at 350 °C to understand the reasons for the introduction of these current paths. An in-situ EDX measurement of the annealed sample revealed an accumulation of Ga at the interface between the FeGa and MgO films. The diffusion length was measured to be 2-5 nm. Thus the reason for the reduction of the TMR ratio and the introduction of the parallel current paths were due to the Ga diffusion into the MgO barrier layer.

TMR junctions were also prepared with the following stack configuration:

TaN 5 nm / Ta 5 nm / PtMn 25 nm / CoFe 2.5 nm / Ru 0.8 nm /
$CoFe_{40}B_{20}$ 4nm / Mg 1.5 nm / MgO 1.5 nm /
$CoFe_{40}B_{20}$ (2 nm or 6 nm) / FeGa 20 nm / Ta 5 nm / Ru 10 nm

The stacks until the top CoFeB layer was sputter deposited at Siemens AG. FeGa, Ta and Ru were sputter deposited at our clean room facility (Kieler Nanolabor). The above mentioned stack configuration has the advantage that FeGa is not in direct contact with the MgO barrier layer. Thus diffusion of Ga into the barrier layer can be avoided. Further this stack configuration can be sputter deposited on commercial Si or Si/SiO_2 substrates. It was also shown in the literature that annealing[91,112,113,114] the CoFeB / MgO / CoFeB based TMR junctions results in large increase in the TMR ratio. Two types of stacks were prepared by varying the thickness of the sensing layer.

For the first configuration 20 nm of FeGa was sputter deposited directly on 2 nm CoFeB film. The junctions were annealed at 285 °C, 350 °C, 400 °C and 450 °C to study further the effect of annealing temperatures on these junctions. An increase in the TMR ratio was observed for increase in annealing temperature until 400 °C. The corresponding TMR ratio at this annealing temperature was 31±5 %. At 450 °C a reduction in the TMR ratio was observed. The RA product of the junctions varied between 4-27 $M\Omega\mu m^2$. It was concluded that the presence of an oxide layer between CoFeB and FeGa is the reason for such high RA product and a reduced TMR ratio. Further the reduction of the TMR ratio of the junctions annealed at 450 °C was concluded due to the Ga diffusion. Ru and Mn diffusion[14,121,123] could also cause an additional reduction of the TMR ratio. An asymmetric tunneling behaviour was observed and the intermixing of CoFeB and FeGa was suggested as the possible reason for such asymmetry.

The second configuration consists of 6 nm CoFeB on top of MgO barrier layer of which 2 nm was sputter etched to remove the oxide layer. FeGa was deposited on remaining 4 nm CoFeB without the break of vacuum to avoid contamination. The junctions were annealed at various temperatures. TMR ratios between 50-65 % were observed for annealing temperatures 325 °C, 350 °C and 375 °C. At 400 °C a reduction in the TMR ratio was observed. The RA of the junctions was between 10-350 $k\Omega\mu m^2$. This was expected for the nominal barrier thickness[9]. Therefore it was shown that sputter etching can remove the oxide film on top of CoFeB. Nearly symmetric tunneling behaviour was observed for this configuration. Large fraction of defective junctions were observed and a further experiment was performed to check if the origin of these defective junctions was annealing. To check this, the TMR stacks on a Si wafer were diced and annealed at 285 °C, 325 °C and 400 °C. After annealing, 2 nm of CoFeB was etched away and FeGa and top electrodes were sputter deposited without break of vacuum. The results were comparable and therefore the reason for defective junctions were proposed either due to the non-uniform argon etch of TMR stack to remove oxide layer before deposition of FeGa or the IBE etch during the lithography.

To use the TMR junctions as strain sensors the strain sensitivity of TMR junctions should be characterized. As the thick and thin FeGa electrodes based TMR junctions did not show a stable anti-parallel configuration the measurements were focused on CoFeB / MgO / CoFeB / FeGa based tunnel junctions. The highest gauge factor achieved for the 2 nm CoFeB/ FeGa top layer (sense layer) based TMR junctions was about GF=42. The 4 nm CoFeB / FeGa top layer based junctions show a small increase in the gauge factor. The measured gauge factor in this case was GF=51. These values of gauge factors are higher than the strain sensitivity of metallic strain gauges, but less than the state-of-the-art TMR sensors[9] and therefore can be used as strain sensors where moderate strain sensitivity is required.

It was shown that TMR junctions with FeGa film show a moderate TMR ratio and moderate strain sensitivity. Further experiments should be performed by sputter deposition of CoFeB / MgO / CoFeB / FeGa based TMR junctions without break of vacuum, thus avoiding the defects arising due to argon etch. A low etch rate of TMR junctions in IBE during lithography is also expected to further reduce the defects and increase the TMR ratio. Annealing temperatures below 400 °C would also be favourable to avoid Ga, Mn and Ru diffusion.

Abbreviations

AFM	Anti-ferromagnet
AMR	Anisotropic magnetoresistance
AP	Anti-parallel configuration of magnetization
DC	Direct current
EDX	Energy dispersive X-ray spectroscopy
FM	Ferromagnet
GMR	Giant magnetoresistance
IBE	Ion beam etching
MOKE	Magneto-optic Kerr effect
MR	Magnetoresistance
MRAM	Magnetic random access memory
ONR	Office of Naval Research
P	Parallel configuration of magnetization
RA	Resistance area
Rap	Anti-parallel resistance
Rp	Parallel resistance
RF	Radio frequency
TEM	Transmission electron microscopy
TMR	Tunneling magnetoresistance
UV	Ultraviolet
VSM	Vibrating sample magnetometry
XPS	X-ray photoelectron spectroscopy
XRD	X-ray diffraction

Bibliography

[1] Jullière, M.: Tunneling between ferromagnetic films., Phys. Lett. A, 54(3), (1975), 225-226.

[2] Moodera, J. S., Kinder, L. R., Wong, T. M., Meservey, R.: Large Magnetoresistance at Room Temperature in Ferromagnetic Thin Film Tunnel Junctions., Phys. Rev. Lett., 74, 16 (1995), 3273-3276.

[3] Xiaoyong Liu, C. Ren., and Gang Xiao, Magnetic tunnel junction field sensors with hard-axis bias field., J. Appl. Phys, 2002, 92(8), 4722–4725.

[4] A. Ney, C. Pampuch., R. Koch, K. H. Ploog., Programmable computing with a single magnetoresistive element., Nature, 2003, 425, , 485-487.

[5] P.P. Freitas, S. Cardoso, R. Sousa, Wanjun Ku, R. Ferreira, V. Chu, J.P. Conde, Spin Dependent Tunnel Junctions for Memory and Read-Head Applications. IEEE Trans. Magn, September 2000, 36(5), 2796-2801.

[6] W. J. Gallagher and S. S. P. Parkin, Development of the magnetic tunnel junction MRAM at IBM: From first junctions to a 16-Mb MRAM demonstrator chip., IBM J. Res. & Dev, 2006, 50(1), p.5.

[7] Quandt, E., Löhndorf, M., Ludwig, A., Wecker, J., Rührig, M.: TMR Sensor, US Patent 10/405, 934.

[8] Löhndorf, M.; Duenas-Lockwood, T.; Tewes, M.; Quandt; E., Rührig, R.; Wecker, J.: Highly sensitive strain sensors based on magnetic tunneling junctions (MTJs)., Appl.Phys.Letter, 81 (2002), 313 – 315.

[9] D. Meyners, T. von Hofe, M. Vieth, M. Rührig, S. Schmitt, and E. Quandt, Pressure sensor based on magnetic tunnel junctions. J. Appl. Phys., 2009 105(07C914).

[10] Löhndorf, M.; Dokupil, S.; Rührig, M.; Wecker, J.; Quandt, E.: Characterization of magnetic tunnel junctions (MTJ) with magnetostrictive free layer materials., J. Magn. Magn. Mat. 272 (2004), 2023-2024.

[11] Löhndorf, M., Dokupil, S., Bootsmann, M.-T., Malavé, A., Rührig, M., Bär, L., Quandt, E.: Characterization of magnetostrictive TMR pressure sensors by MOKE. J. Magn. Magn. Mat., 316 (2007), e223–e225.

[12] A. E. Clark, J. B. Restorff, M. Wun-Fogle, T. A. Lograsso, and D. L. Schlagel, Magnetostrictive properties of body-centered cubic Fe–Ga and Fe–Ga–Al alloys, IEEE Trans.Magn., 2000, 36, 3238–3240.

[13] J. Joshua Yang, Chengxiang Ji, Y. Austin Chang, Xianglin Ke, and M. S. Rzchowski, Over 70% tunneling magnetoresistance at room temperature for a CoFe and AlO_x based magnetic tunnel junction, Appl. Phys. Lett. 89, 202502 (2006).

[14] S. Ikeda, J. Hayakawa, Y. Ashizawa, Y. M. Lee, K. Miura, H. Hasegawa, M. Tsunoda, F. Matsukura, and H. Ohno, Tunnel magnetoresistance of 604% at 300 K by suppression of Ta diffusion in CoFeB/MgO/CoFeB pseudo-spin-valves annealed at high temperature Appl. Phys. Lett. 93, 082508 (2008)

[15] Butler, W. H., Zhang, X.-G., Schulthess, T. C., MacLaren, J. M.: Spin-dependent tunneling conductance of Fe/MgO/Fe sandwiches, Phys. Rev. B 63 (2001), 054416

[16] G. X. Miao, J. Y. Chang, M. J. van Veenhuizen, K. Thiel, M. Seibt, G. Eilers, M.Münzenberg, and J. S. Moodera , Epitaxial growth of MgO and Fe/MgO/Fe magnetic tunnel junctions on (100)-Si by molecular beam epitaxy, Applied Physics Letters, October 2008, 93 (14), 10

[17] Frédéric Bonell, Stéphane Andrieu, François Bertran, Patrick Lefèvre, Amina Taleb Ibrahimi, Etienne Snoeck, Coriolan-Viorel Tiusan, and François Montaigne, MgO-Based Epitaxial Magnetic Tunnel Junctions Using Fe-V Electrodes, IEEE Transactions on Magnetics, Vol, October 2009, 45(10).

[18] A. Butera, J. Gómez, J. L. Weston, and J. A. Barnard, Growth and magnetic characterization of epitaxial $Fe_{81}Ga_{19}$/MgO (100) thin films, J. Appl. Phys., 2005, 98,, 033901.

[19] Hand book of Giant Magnetostricitive Materials, Edited by Göran Engdahl, Page 1.

[20] Hand book of Giant Magnetostricitive Materials, Edited by Göran Engdahl, Page 2.

[21] E. du Trémolet de Lacheisserie, "Magnetostriction: Theory and Applications of Magnetoelasticity," CRC Press, Boca Raton, FL, 1993, page 45.

[22] E. du Trémolet de Lacheisserie, "Magnetostriction: Theory and Applications of Magnetoelasticity," CRC Press, Boca Raton, FL, 1993, page 43.

[23] B.D. Cullity and C.D.Graham., Introduction to Magnetic Materials, Second Edition, Page 255.

[24] G.A.Gehring, M.Ali, M.D.Cooke, R. Mattheis, Determination of magnetostriction in thin films using strained substrate techniques., J. Magn. Magn. Mater., 2003, 257(15-21).

[25] E.Klokholm, The measurement of magnetostriction in ferromagnetic thin films, IEEE Trans. Magn. Mag-12, 819,(1976).

[26] E. du Trémolet De Lacheisserie und J.C. Peuzin., Magnetostriction and internal stresses in thin films: the cantilever method revisited., J. Magn. Magn. Mater., 136 (1-2):189, 196, 1994.

[27] Villari, E., Ueber die Aenderungen des Magnetischen Moments, welche der zug und das Hindurchleiten eines galvanischen Stroms in einem Stabe von Stahl oder Eisen hervorbringen, Ann.Phys.Chem. (Poggendorf Annals) 126, 87, 1865.

[28] Thomas A. Baudendistel and Michael L. Turner, Member, IEEE., A Novel Inverse-Magnetostrictive Force Sensor., IEEE Sensors Journal, February 2007, 7(2).

[29] Arthur Beiser., Concept of Modern Physics, Sixth Edition, page 184, 193.

[30] H. Nagura, K. Saito, K. Takanashi, H. Fujimori., Influence of third elements on the anisotropic magnetoresistance in permalloy films., J. Magn. Magn. Mater., 2000, 212(1-2), 53-58.

[31] T.R. Mcguire, R.I. Poter, Anisotropic Magnetoresistance in Ferromagnetic 3d Alloys., IEEE Trans. Magn., 1975, 11(4), 1018-1038.

[32] J. Smit, "Magnetoresistance of ferromagnetic metals and alloys at low temperatures," Physica, vol. XVI, No. 6, pp. 612-627, June 1951.

[33] H. C. van Elst, "The anisotropy in the magneto-resistance of some nickel alloys," Physica, vol. 25, pp. 708-720, 1959.

[34] M. Baibich, J. Broto, A. Fert, F. Nguyen Van Dau, F. Petroff, P. Etienne, G. Creuzet, A. Friederich, J. Chazelas, Gaint Magnetoresistance of (001) Fe / (001) Cr Magnetic Superlattices Phys. Rev. Lett. , 1988, 61, (21), 2472 -2475.

[35] G. Binasch, P. Grunberg, F. Saurenbach, W. Zinn, Phys. Rev. B 39, 4828 (1989).

[36] Parkin, S.S.P., Origin of enhanced magnetoresistance of magnetic multilayers: Spin-dependent scattering from magnetic interface states., Physical Review Letters, 1993, 71(10), 1641-1644.

[37] S. S. P. Parkin, Z. G. Li, and David J. Smith, Giant magnetoresistance in antiferromagnetic Co/Cu multilayers, Appl. Phys. Lett. 58, 2710 (1991).

[38] H. Kano, K. Kagawa, A. Suzuki, A. Okabe, K. Hayashi et al, Substrate temperature effect on giant magnetoresistance of sputtered Co/Cu multilayers, Appl. Phys. Lett. 63, 2839 (1993).

[39] R. Schad, C. D. Potter, P. Belien, G. Verbanck, V. V. Moshchalkov, and Y. Bruynseraede, Giant magnetoresistance in Fe/Cr superlattices with very thin Fe layers, Appl. Phys. Lett. 64, 3500 (1994).

[40] S. S. P. Parkin, K. P. Roche, M.G. Samant, P. M. Rice, R. B. Beyers, R. E.Scheuerlein, E. J. O'Sullivan, S. L. Brown, J. Bucchigano, D. W. Abraham, Yu Lu, M. Rooks, P. L. Trouillowd, R. A. Wanner, W. J. Galagher, Exchange-biased magnetic tunnel junctions and application to nonvolatile magnetic random access memory., J. Appl. Phys, . 1999, 85, (8), 5828-5833.

[41] B.D. Cullity and C.D.Graham., Introduction to Magnetic Materials, Second Edition, page 510.

[42] H. J. Mamin, B. A. Gurney, D. R. Wilhoit, and V. S. Speriosu, "High sensitivity spin-valve strain sensors," Appl. Phys. Lett., vol. 72, pp.3220–3222, June 1998.

[43] S. S. Parkin et al., "Exchange-biased magnetic tunnel junctions and application to nonvolatile magnetic random access memory," J. Appl. Phys., vol. 85, pp. 5828–5833, Apr. 1999.

[44] Löhndorf, M.; Duenas-Lockwood, T.; Ludwig, A.; Rührig, M.; Bürgler, D.; Grünberg, P.; Quandt, E. : Strain sensors based on magnetostrictive GMR/TMR structures., IEEE Trans. Magn., 38 (2002), 2826-2828.

[45] J -G. Zhu, and C. Park, Magnetic tunnel junctions, Mater. Today, 2006, 9(11), 36.

[46] Le Clair, P.L. Fundamental Aspects of Spin Polarized Tunneling, PhD Thesis, Eindoven University of Technology, 2002.

[47] Gider S, Runge B U, Marley A C and Parkin S S P, The Magnetic Stability of Spin-Dependent Tunneling Devices., Science, 1998 281 797.

[48] Tedrow PM, Meservey R, Spin-dependent tunneling into ferromagnetic nickel., Phys. Rev. Lett., 1971 26, 192-195.

[49] Tedrow PM, Meservey R, Direct observation of spin-mixing in superconductors, Phys Rev Lett, 1971, 27, 919-921.

[50] Tedrow, P.M., and R. Meservey, Spin polarization of electrons tunneling from films of Fe, Co, Ni, Gd,. Phys. Rev. B, 1973, 7, 318-326.

[51] M. B. Stearns. J. Magn. Magn. Mater., 1977, 5, 1062.

[52] Slonczewski, J.C., Conductance and exchange coupling of two ferromagnets separated by a tunneling barrier., Physical Review B, 1989, 39(10), 6995-7002.

[53] Mathon, J. and Umerski, A., Theory of tunneling magnetoresistance of an epitaxial Fe/MgO/Fe(001) junction., Physical Review B, 2001, 63(22), 220403.

[54] Tsymbal, E.Y., O. N. Mryasov, P. R. LeClair, Spin dependent tunneling in magnetic tunnel junctions., J. Phys.: Condens.Matter, 2003, 15(4), R109-R142.

[55] D. D. Djayaprawira, K. Tsunekawa, M. Nagai, H. Maehara, S. Yamagata, N. Watanabe, S. Yuasa, Y. Suzuki, and K. Ando, Appl. Phys. Lett., 86, 092502 (2005).

[56] Yuasa, S., Nagahama, T., Fukushima, A., Suzuki, Y. and Ando, K., Giant room-temperature magnetoresistance in single-crystal Fe/MgO/Fe magnetic tunnel junctions., Nat Mater, 2004, 3(12), 868-871.

[57] H. J. Mamin, B. A. Gurney, D. R. Wilhoit, and V. S. Speriosu, "High sensitivity spin-valve strain sensors," Appl. Phys. Lett., vol. 72, pp. 3220–3222, June 1998.

[58] S. S. Parkin et al., "Exchange-biased magnetic tunnel junctions and application to nonvolatile magnetic random access memory," J. Appl.Phys., vol. 85, pp. 5828–5833, Apr. 1999.

[59] J.Stöhr and H.C. Steigmann., Magnetism From Fundamentals to Nanoscale Dynamics, page 617.

[60] Meiklejohn, W. H. und C. P. Bean, New Magnetic Anisotropy., Phys. Rev., 1956, 102(5), 1413.

[61] Meiklejohn, W. H. und C. P. Bean, New Magnetic Anisotropy. Phys. Rev.,1956, 105(3), 904.

[62] Dirk Meyners, Herstellung und Charakterisierungvon Logikarrays mit ultrakleinen magnetischen Tunnelelementen, PhD thesis, Faculty of physics, Bielefeld University. Page 18.

[63] Peng Zhao, Zhenli Zhao, Dwight Hunter, Richard Suchoski, Chen Gao, Scott Mathews, Manfred Wuttig, and Ichiro Takeuchi., Fabrication and characterization of all-thin-film magnetoelectric sensors., Appl. Phys. Lett., 2009(94), 243507.

[64] B Adolphi, J.M., M Bertram, C-G Oertel, U Merkel, U Marschner, R Schäfer, C Wenzel and W-J Fischer., Improvement of sputtered Galfenol thin films for sensor applications., Smart Mater. Struct., 2010, 19(5), 055013.

[65] Patrick D. McGary, L.T., Jia Zou, Bethanie J. H. Stadler, Patrick R. Downey, and Alison B. Flatau, Magnetic nanowires for acoustic sensors *J. Appl. Phys.*, 2006(99), 08B310.

[66] www.crystec.de

[67] www.semiwafer.com

[68] I.Fergen., Entwicklung, Herstellungund Charakterisierung weichmagnetischer Dünnschichten für Hochfrequenz-Anwendungen Dissertation, Universität Karlsruhe (TH), 2003, Page. 40.

[69] J Du , S Gnanarajan and A Bendavid, Characterization of MgO substrates for growth of epitaxial YBCO thin films, Supercond. Sci. Technol., 2005, 18, 1035–1041.

[70] http://www.siemens.com/corporate-technology/en/index.php

[71] Sangjun Han, James Derksen, and Jung-Hoon Chun, Extrusion Spin Coating: An Efficient and Deterministic Photoresist Coating Method in Microlithography., IEEE Trans. on Semiconductor Manufacturing, 2004, 17(1).

[72] http://groups.mrl.uiuc.edu/dvh/pdf/AZ5214E.pdf

[73] www.microchemicals.eu

[74] S.J.B. Reed., Electron microprobe analysis and scanning electron microscopy in geology., Cambridge University Press, 2005, Page. 1.

[75] Atkins., Physical Chemistry, Sixth Edition, Page 625, 626.

[76] Fuchs, E., Oppolzer, H., Rehme, H., Particle beam microanalysis: fundamentals, methods and applications., VCH, 1990, page 138.

[77] David B. Williams and C. Barry Carter, Transmission Electron Microscopy, Page 143.

[78] K.H.J. Buschow and F.R. de Boer, Physics of Magnetism and Magnetic Materials, Kluwer Academic/Plenum Publishers, 2003. Page 87.

[79] Amit Kulkarni, Magnetic nanocomposites, Dissertation, Technischen Fakultät, Christian-Albrechts-Universität zu Kiel, Page 44.

[80] Alex Hubert and Rudolf Schäfer, Magnetic Domains- The Analysis of Magnetic Microstructures. Page 25.

[81] Delacheisserie, E. D. T. & Peuzin, J. C. Magnetostriction and internal-stresses in thin-films-The cantilever method revisited., J. Magn. Magn. Mater., 1994, 136, 189–196.

[82] Christoph Bechtold, Entwicklung von $Fe_{70}Pd_{30}$-Dünnschichtsensoren zur Bestimmung von Dehnung mittels des Inversen magnetischen Formgedächtnise effektes, Dissertation, Technischen Fakultät, Christian-Albrechts-Universität zu Kiel, Page 32.

[83] A. Ludwig., Herstellung, Charakterisierung und Optimierung hochmagnetostriktiver Viellagenschichten., Dissertation, Universität Karlsruhe (TH), 1999, page. 49.

[84] A. Ludwig and E. Quandt. Giant magnetostrictive thin films for applications in microelectromechanical systems (invited)., J. Appl. Phys., 87:4691_4695, 2000.

[85] I. Fergen., Entwicklung, Herstellung und Charakterisierung weichmagnetischer Dünnschichten für Hochfrequenz-Anwendungen Dissertation, Universität Karlsruhe (TH), 2003, Page. 57.

[86] B.W. Wang et al., Structure, magnetic properties and magnetostriction of Fe81Ga19 thin films., Journal of Magnetism and Magnetic Materials, 2008, 320 (5), 769–773.

[87] Clark A.E, Hathaway K.B., Wun-Fogle M, Restorff J B, Lograsso T.A, Keppens V.M, Petculescu G and Taylor R A., Extraordinary magnetoelasticity and lattice softening in bcc Fe–Ga alloys., J. Appl. Phys., 2003, 93, 8621.

[88] D.M. Jeon, J.W. Park, D.H. Lee, S.Y. Yoon, D.H. Yoon, S.J. Suh, Annealing effect on the barrier properties and TMR of magnetic tunneling junctions fabricated in various oxidation conditions., Journal of Magnetism and Magnetic Materials, 2004, 272–276(3), 1956–1958.

[89] W. G. Wang et al., Understanding tunneling magnetoresistance during thermal annealing in MgO-based junctions with CoFeB electrodes., Physical Review B 81, 2010, 144406.

[90] Il-Jae Shin, Byoung-Chul.Min., Jin Pyo Hong, and Kyung-Ho Shin., Effects of Ru diffusion in exchange-biased MgO magnetic tunnel junctions prepared by in situ annealing., Appl. Phys. Lett., 2009, 95, (22), 222501.

[91] Shinji Yuasa, T.N., Akio Fukushima, Yoshishige Suzuki and Koji Ando, Giant room-temperature magnetoresistance in single-crystal Fe/MgO/Fe magnetic tunnel junctions, Nature Materials, 2004, 3, 868 - 871.

[92] O. Ikeda, R. Kainuma, I. Ohnuma, K. Fukamichi, and K. Ishida, Phase equilibria and stability of ordered b.c.c. phases in the Fe-rich portion of the Fe–Ga system, J. Alloys Compd., 2002, 347, 198.

[93] Y. Du, M.Huang, S. Chang, D.L. Schlagel, T.A. Lograsso and R.J. Mc Queeney, Relation between Ga ordering and magnetostriction of Fe-Ga alloys studied by x-ray diffuse scattering., Phys. Rev. B, 2010, 81(5), 054432.

[94] Kiyotaka Wasa, Makoto Kitabatake Hideaki Adachi, Thin Film Materials Technology: Sputtering of compound Materials., Page 3.

[95] A. E. Clark, M. Wun-Fogle, J. B. Restorff, T. A. Lograsso, and J. R.Cullen, IEEE Trans. Magn., 37, 2678, 2001.

[96] T.A. Lograsso, A.R. Ross, D.L. Schlagel, A.E. Clark, M. Wun-Fogle, Structural transformations in quenched Fe–Ga alloys, Journal of Alloys and Compounds, 2003, 350, 95–101.

[97] A.E. Clark, J.B. Restorff, M. Wun-Fogle, T.A. Lograsso, D.L. Schlagel, Magnetostrictive properties of body-centered cubic Fe–Ga and Fe–Ga–Al alloys, IEEE Transactions on Magnetics, 36, (2000), pp. 3238–3240.

[98] N. Srisukhumbowornchai, S. Guruswamy, Influence of ordering on the magnetostriction of Fe–27.5 at% Ga alloys, Journal of Applied Physics, 92, (2002), pp. 5371–5379.

[99] Himalay Basumatary, Mithun Palit, J. Arout Chelvane, S. Pandian, M. Manivel Raja and V. Chandrasekaran, Structural ordering and magnetic properties of $Fe_{100-x}Ga_x$ alloys, Scripta Materialia, 59, (2008), 878–881.

[100] J.M. Borrego, J.S.B., C.F. Conde,A. Conde, S. Roth., Structural ordering and magnetic properties of arc-melted FeGa alloys., Intermetallics, February 2007, 15(2), 192-200.

[101] N. Srisukhumbowornchai and S. Guruswamy, Large magnetostriction in directionally solidified FeGa and FeGaAl alloys, J. Appl. Phys., 90, 5680, (2001).

[102] Rajneeta R. Basantkumar, Bethanie J. Hills Stadler, William P. Robbins, and Eric M. Summers, Integration of Thin-Film Galfenol With MEMS Cantilevers for Magnetic Actuation, IEEE Transactions on Magnetics, October 2006, 42(10), 3102-3104.

[103] http://www.crystran.co.uk/magnesium-oxide-mgo.htm

[104] A. Javed, N. A. Morley, M. R. J. Gibbs, "Structure, magnetic and Magnetostrictive properties of As-deposited Fe-Ga thin films"., J. Magn. Magn. Mater., 321, (2009), 2877- 2882.

[105] Herzer, G. Grain size dependence of coercivity and permeability in nanocrystalline ferromagnets., IEEE Trans. Magn., 1990, 26(5), 1397-1402.

[106] A. Javed, T.S., N.A. Morley,M.R.J. Gibbs, An investigation of the effect of structural order on magnetostriction and magnetic behavior of Fe–Ga alloy thin films., Acta Materialia, 2010, 58(11), 4003–4011.

[107] N. A. Morley, A.J., and M. R. J. Gibbs., Effect of a forming field on the magnetic and structural properties of thin Fe–Ga films., J. Appl. Phys., 2009, 105(7), A912.

[108] Xiaoming Kou, Weigang Wang ,Xin Fan, Lubna R. Shah, Rae Tao, and John Q. Xiao, High temperature annealing induced superparamagnetism in CoFeB/MgO/CoFeB tunneling junctions Journal of Applied Physics, 2010, 108(8), 083901.

[109] W. G. Wang,C. Ni, G. X. Miao, C. Weiland, L. R. Shah, X. Fan, P. Parson, J. Jordan-sweet, X. M. Kou,Y. P. Zhang, R. Stearrett, E. R. Nowak, R. Opila, J. S. Moodera, and J. Q. Xiao, Understanding tunneling magnetoresistance during thermal annealing in MgO-based junctions with CoFeB electrodes., Physical Review B 81, 144406, 2010.

[110] W. G. Wang, C. Ni, A. Rumaiz, Y. Wang, X. Fan, T. Moriyama, R. Cao, Q. Y. Wen, H. W. Zhang, and John Q. Xiao, Real-time evolution of tunneling magnetoresistance during annealing in CoFeB/MgO/CoFeB magnetic tunnel junctions., Appl. Phys. Lett., 2008, 92, 152501.

[111] S. Ikeda, J. Hayakawa, Y. M. Lee, R. Sasaki, T. Meguro, F. Matsukura,and H. Ohno, Dependence of Tunnel Magnetoresistance in MgO Based Magnetic Tunnel Junctions on Ar Pressure during MgO Sputtering., Jpn. J. Appl. Phys., 2005, 44, L1442-L1445.

[112] S. Yuasa, A. Fukushima, T. Nagahama, K. Ando, and Y. Suzuki, High Tunnel Magnetoresistance at Room Temperature in Fully Epitaxial Fe/MgO/Fe Tunnel Junctions due to Coherent Spin-Polarized Tunneling., Jpn. J. Appl. Phys., 2004, 43, L588-L590.

[113] S. S. Parkin, C. Kaiser, A. Panchula, P. M. Rice, B. Hughes, M. Samant, and S.-H. Yang, Giant tunneling magnetoresistance at room temperature with MgO (100) tunnel barriers,
Nat. Mater. 3, 862 (2004).

[114] J. Hayakawa, S. Ikeda, F. Matsukura, H. Takahashi, and H. Ohno, Dependence of Giant Tunnel Magnetoresistance of Sputtered CoFeB/MgO/CoFeB Magnetic Tunnel Junctions on MgO Barrier Thickness and Annealing Temperature., Jpn. J. Appl. Phys., 2005, Part 2 44, L587-L589.

[115] S. Yuasa, Y. Suzuki, T.Katamaya, K.Ando, Characterization of growth and crystallization processes in CoFeB/MgO/CoFeB magnetic tunnel junction structure by reflective high-energy electron diffraction., Appl. Phys. Lett., 87, (2005), 242503.

[116] X.-G. Zhang and W. H. Butler, Large magnetoresistance in bcc Co⁄MgO⁄Co and FeCo⁄MgO⁄FeCo tunnel junctions., Phys. Rev., 2004, B 70, 172407.

[117] G. Feng, Sebastian van Dijken, J. F. Feng, J. M. D. Coey, T. Leo, Annealing of CoFeB/MgO based single and double barrier magnetic tunnel junctions: Tunnel magnetoresistance, bias dependence, and output voltage., J. Appl. Phys., 2009, 105, 033916.

[118] W. Oepts, M. F. Gillies, R. Coehoorn, R. J. M. van de Veerdonk, and W. J.M. de Jonge, J., Asymmetric bias voltage dependence of the magnetoresistance of Co/Al2O3/Co magnetic tunnel junctions: Variation with the barrier oxidation time., J. Appl. Phys., 2001, 89, 8038.

[119] Y. M. Lee, J. Hayakawa, S. Ikeda, F. Matsukura, and H. Ohno, Giant tunnel magnetoresistance and high annealing stability in CoFeB/MgO/CoFeB magnetic tunnel junctions with synthetic pinned layer., Appl. Phys. Lett., 2006, 89, 042506.

[120] W. G. Wang, C. Ni, A. Rumaiz, Y. Wang, X. Fan, T. Moriyama,R. Cao, Q. Y. Wen, H. W. Zhang, and J. Q. Xiao, Appl. Phys.Lett. 92, 152501, 2008.

[121] J. Hayakawa, S. Ikeda, Y. M. Lee, F. Matsukura, and H. Ohno, Effect of high annealing temperature on giant tunnel magnetoresistance ratio of CoFeB/MgO/CoFeB magnetic tunnel junctions, Appl. Phys. Lett., 89, 232510 (2006).

[122] Rie Matsumoto, Shingo Nishioka, Masaki Mizuguchi, Masashi Shiraishi, Hiroki Maehara, Koji Tsunekawa, David D. Djayaprawira, Naoki Watanabe, Yuichi Otani, Taro Nagahama, Akio Fukushima, Hitoshi Kubota, Shinji Yuasa, Yoshishige Suzuki, Dependence on annealing temperatures of tunneling spectra in high-resistance CoFeB/MgO/CoFeB magnetic tunnel junctions., Solid State Communications, September 2007, 143(11–12), 574–578.

[123] Gen Feng, Sebastiaan van Dijken, and J. M. D. Coey, Influence of annealing on the bias voltage dependence of tunneling magnetoresistance in MgO double-barrier magnetic tunnel junctions with CoFeB electrodes., Appl. Phys. Lett 89, 162501 (2006).

[124] D Meyners, H Brükl and G Reiss, Influence of boundary roughness on the magnetization reversal in submicron sized magnetic tunnel junctions, Influence of boundary roughness on the magnetization reversal in submicron sized magnetic tunnel junctions., Journal of Applied Physics, 2003, 93, 5.

[125] Strain Gauge Technology, edited by A. L. Window (Springer, New York, 1992).

[126] A Tibrewala, E Peiner, R Bandorf, S Biehl and H Lüthje, Piezoresistive gauge factor of hydrogenated amorphous carbon films, Journal of Micromechanical and Microengineering, 2006, 16,(6), S75–S81.

[127] Cosmin Farcau, Neralagatta M. Sangeetha, Helena Moreira, Benoît Viallet, Jérémie Grisolia, Diana Ciuculescu-Pradines, and Laurence Ressier, High-Sensitivity Strain Gauge Based on a Single Wire of Gold Nanoparticles Fabricated by Stop-and-Go Convective Self-Assembly, ACS Nano, 2011, 5(9), 7137–7143.